Lappeenrannan teknillinen korkeakoulu
Lappeenranta University of Technology

Jussi Salo

DESIGN AND ANALYSIS OF A TRANSVERSAL-FLUX SWITCHED-RELUCTANCE-LINEAR-MACHINE POLE-PAIR

Thesis for the degree of Doctor of Science (Technology) to be presented with due permission for public examination and criticism in the Auditorium 1381 at Lappeenranta University of Technology, Lappeenranta, Finland on the 18th of December, 1999, at noon.

Acta Universitatis
Lappeenrantaensis
92

ISBN 951-764-389-6
ISSN 1456-4491

Lappeenrannan teknillinen korkeakoulu
Monistamo 1999

ABSTRACT

Lappeenranta University of Technology
Acta Universitatis Lappeenrantaensis 92

Jussi Salo

Design and analysis of a transversal-flux switched-reluctance-linear-machine pole-pair

Lappeenranta 1999

ISBN 951-764-389-6, ISSN 1456-4491 UDC 621.313.282

Key words: switched reluctance machine, SR-motor, linear motor, transversal-flux, scaling

The Switched Reluctance technology is probably best suited for industrial low-speed or zero-speed applications where the power can be small but the torque or the force in linear movement cases might be relatively high. Because of its simple structure the SR-motor is an interesting alternative for low power applications where pneumatic or hydraulic linear drives are to be avoided.

This study analyses the basic parts of an LSR-motor which are the two mover poles and one stator pole and which form the “basic pole pair” in linear-movement transversal-flux switched-reluctance motors. The static properties of the basic pole pair are modelled and the basic design rules are derived. The models developed are validated with experiments. A one-sided one-pole-pair transversal-flux switched-reluctance-linear-motor prototype is demonstrated and its static properties are measured.

The modelling of the static properties is performed with FEM-calculations. Two-dimensional models are accurate enough to model the static key features for the basic dimensioning of LSR-motors. Three-dimensional models must be used in order to get the most accurate calculation results of the static traction force production.

The developed dimensioning and modelling methods, which could be systematically validated by laboratory measurements, are the most significant contributions of this thesis.

CONTENTS

ABBREVIATIONS AND SYMBOLS

α	temperature coefficient of the resistance.
δ	air gap length.
η	efficiency of stator winding.
Θ	magnetomotive force (MMF), total current in coil, ampere turns.
μ_0	permeability of the vacuo.
μ_r	relative permeability.
ν_r	relative magnetic reluctivity of the material.
ξ	winding factor.
ρ_{Cu}	density of copper.
ρ_{Fe}	density of iron.
σ	air gap shear stress.
σ_n	normal component of the air gap shear stress.
σ_t	tangential component of the air gap shear stress.
τ_d	distance between traction force pulses of individual phases.
τ_m	mover pole pitch.
τ_{ovl}	overlap distance of the traction force pulses.
τ_p	traction force pulse pitch.
τ_s	stator pole pitch.
$\Psi(i,x)$	flux linkage base function.
ψ	flux linkage.
ψ_d	fictious eddy current flux caused by the alternating main flux.
ψ_M	main flux transferring electrical energy to mechanical work.
ψ_v	fictious iron loss flux caused by the velocity effects.
Ω_e	finite element volume.
A	cross-sectional area of the pole face.
A_δ	area of the air gap in the direction of movement.
A_{Cu}	cross-sectional area of the winding copper.
A_e	virtual current loading.
A_s	area covered by the stator.
A_w	winding area.

$\boldsymbol{B}$	magnetic flux density (vector).
$\hat{B}$	magnetic loading.
B_{n}	normal component of magnetic flux density.
B_{t}	tangential component of magnetic flux density.
C	constant.
d_{w}	depth of the winding window.
$\boldsymbol{F}$	force (vector).
F_{ave}	average traction force value.
F_{ep}	traction force mover in the edge position.
F_{L}	load force.
F_{max}	maximum traction force value of the continuous traction force curve.
F_{mean}	mean value of the continuous traction force curve.
F_{min}	minimum traction force value of the continuous traction force curve.
F_{n}	normal component of the force.
F_{t}	traction force, the tangential component of the force.
F_{tp}	traction force curve of the individual phase.
$\boldsymbol{H}$	magnetic field strength (vector).
h_{m}	mover pole height.
h_{mlf}	mover pole height of the LF-LSR-motor.
H_{n}	normal magnetic field strength component.
h_{s}	stator pole height.
h_{slf}	stator pole height of the LF-LSR-motor.
H_{t}	tangential magnetic field strength component.
i	current.
$I(\psi,x)$	current base function.
i_{d}	current associated with the eddy current iron losses.
i_{h}	current associated with the hysteresis effects.
$\Delta i_{\mathrm{h}\downarrow}$	hysteresis current band in downward traction force measurement.
$\Delta i_{\mathrm{h}\uparrow}$	hysteresis current band in upward traction force measurement.
i_{L}	current associated with the mechanical work.
i_{M}	magnetising current of main flux.
I_{n}	nominal current.

i_v	current of the iron losses of velocity effects.
J	current density.
K	coefficient.
k_{sc}	scaling factor.
k_w	winding fill factor.
l	pole length, the length of the mover pole circle.
L_σ	inductance of the ideal coil of stray flux.
l_a	length of the pole arc of the stator pole of TF-TLSR-motor.
L_e	electrical length of TF-LSR-motor.
L_{elf}	electrical length of the LF-LSR-motor.
l_p	total stator pole length of the TF-LSR-motor.
l_{pa}	total stator pole arc of the TF-TLSR-motor.
L_{str}	stroke distance of the mover.
l_w	length of the winding window.
l_{wa}	arc of the winding window of TF-TLSR-motor.
M	mass.
m	phase number.
M_{1s}	total mass of the one-sided TF-LSR-motor.
M_{4s}	total mass of the four-sided TF-LSR-motor.
M_{clf}	mass of the copper of LF-LSR-motor.
M_{ctl}	mass of the copper of the LF-TLSR-motor.
M_{Cu}	copper mass.
M_{lf}	mass of all magnetic parts of an LF-LSR-motor.
M_{lf2}	total mass of the magnetic circuit parts of the two-sided LF-LSR-motor.
M_{m1s}	total mass of the moving magnetic circuit parts of the one-sided TF-LSR-motor.
M_{m4s}	mass of the moving iron of the four-sided TF-LSR-motor.
M_{ml2}	mass of the mover of the two-sided LF-LSR-motor.
M_{mlf}	mass of the mover of an LF-LSR-motor.
M_{mp}	mass of the mover pole iron of the one sided TF-LSR-motor.
M_{mp4}	mass of the four-sided mover pole of TF-LSR-motor.
M_{mtl}	mass of the mover of the LF-TLSR-motor.
M_{slf}	mass of the stator of LF-LSR-motor.

M_{sp}	mass of the stator pole iron.
M_{stl}	mass of the stator of the LF-TLSR-motor.
M_{t4s}	total mass of four-sided stator TF-TLSR-motor.
M_{tcp}	mass of the copper of the stator pole winding of the TF-TLSR-motor.
M_{tlf}	mass of magnetic parts of LF-TLSR-motor.
M_{tm}	total mass of the mover of the TF-TLSR-motor.
M_{tmp}	mass of the mover pole iron of the TF-TLSR-motor.
M_{tsp}	mass of the pole of the stator pole iron of the TF-TLSR-motor.
N	number of turns in coil winding.
$\boldsymbol{n}$	unit vector.
P_c	power dissipated in the coil.
P_{cla}	classical eddy current power losses.
P_d	eddy current power losses caused by the alternating main flux.
P_{dyn}	dynamic power losses.
P_{exe}	excess power losses.
P_{Fe}	total iron power losses.
P_{hys}	hysteresis power losses.
p_m	mover pole number of transversal flux construction.
p_{mlf}	mover pole number of the LF-LSR-motor.
p_s	stator pole number of transversal flux construction.
p_{s1s}	stator pole number of the one-sided TF-LSR-motor.
p_{s4s}	stator pole number of the four-sided TF-LSR-motor.
p_{slf}	stator pole number of the LF-LSR-motor.
P_v	power losses of the eddy currents caused by velocity effects.
q	general direction used in force computation.
R	resistance.
R_d	resistance associated with the power losses of the eddy currents caused by alternating main flux.
R_h	resistance associated with the power losses of the magnetic hysteresis.
r_{mi}	inner radius of the mover of a TF-TLSR-motor.
r_{mo}	outer radius of the mover of a TF-TLSR-motor.
r_{mtb}	radius of the mover back iron of an LF-TLSR-motor.
r_{mto}	outer radius of the mover of an LF-TLSR-motor.

r_{si}	inner radius of the stator pole of a TF-TLSR-motor.
r_{si0}	approximate value of the stator inner radius of a TF-TLSR-motor.
r_{sig}	inner radius of stator when the air gap of a TF-TLSR-motor is zero.
r_{so}	outer radius of the stator of a TF-TLSR-motor.
r_{stb}	radius of the back iron of the stator of an LF-TLSR-motor.
r_{sti}	inner radius of the stator of an LF-TLSR-motor.
R_v	resistance associated with the power losses of the eddy currents caused by the velocity effects.
S	integration volume.
s	intergation surface.
s_{m}	distance between two mover poles.
T	torque.
t	time, pole width.
$\boldsymbol{t}$	unit vector.
$T(i,x)$	torque base function.
T_{c}	average temperature of the coil.
T_{em}	elctromagnetic torque.
T_{n}	nominal torque.
u	voltage.
u_{ind}	induced voltage of auxilary measuration coil.
v	velocity.
V_{clf}	total copper volume of an LF-LSR-motor.
V_{ctl}	total copper volume of an LF-TLSR-motor.
V_{Cup}	copper volume of the stator pole winding.
V_{mlf}	volume of the mover of an LF-LSR-motor.
V_{mp1}	volume of the mover pole of the one-sided TF-LSR-motor.
V_{mp4}	volume of the four-sided mover pole of a TF-LSR-motor.
V_{mtl}	volume of the mover of an LF-TLSR-motor.
V_{slf}	volume of the stator of an LF-LSR-motor.
V_{sp}	volume of the iron of the stator pole pair.
V_{stl}	volume of the stator iron of the LF-TLSR-motor.
V_{tcp}	volume of the copper of the stator pole winding of the TF-TLSR-motor.
V_{tmp}	volume of the mover pole of the TF-TLSR-motor.

V_{tsp}	volume of the tubular four-sided stator of the TF-TLSR-motor.
W_{co}	magnetic coenergy.
W_f	magnetic field energy.
W_{lin}	magnetic field energy of a magnetically linear circuit.
x	co-ordinate axis.
x	position of the mover.
x_{ep}	edge position of the mover.
x_{max}	point of the maximum traction force of the continous traction force curve.
x_{min}	point of the minimum traction force of the continous traction force curve.
y	co-ordinate axis.
z	co-ordinate axis.

Acronyms

2D	two dimensional.
3D	three dimensional.
A	a region in finite element mesh, label of the element of mesh.
AC	alternating current.
B	a region in finite element mesh, label of the element of mesh.
BTFPP	Basic Transversal Flux Pole Pair.
cos(φ)	stator power factor.
C	a region in finite element mesh, label of the element of mesh.
CRD	control rod drive.
D	a region in finite element mesh, label of the element of mesh.
D1	a region in finite element mesh, label of the element of mesh.
D2	a region in finite element mesh, label of the element of mesh.
D3	a region in finite element mesh, label of the element of mesh.
D4	a region in finite element mesh, label of the element of mesh.
DC	direct current, direct current machine.
E	a region in finite element mesh, label of the element of mesh.
FEM	finite element method.
IM	induction machine.

LF	longitudinal flux construction.
LF-LSR-motor	longitudinal flux linear movement switched reluctance motor.
LF-TLSR-motor	longitudinal flux tubular pole geometry linear movement switched reluctance motor.
LSR-motor	linear movement switched reluctance motor.
M1	magnetic material name used.
M2	magnetic material name.
M3	magnetic material name.
M4	magnetic material name.
MAGLEV	magnetic levitation and propulsion in railroad technology.
MMF	magnetomotive force.
PM	permanent magnet.
SM	synchronous machine.
SR	switched reluctance.
TF	transversal flux construction.
TF-CLSR-motor	transversal flux cylindrical pole geometry linear movement switched reluctance motor.
TF-LSR-motor	transversal flux linear movement switched reluctance motor.
TLSR-motor	tubular pole geometry linear movement switched reluctance motor.
TRV	torque per unit rotor volume.

Operators

ceil{argument}	integer of the argument added by one.

Subscripts

sc	scaled value.

1 INTRODUCTION

The enhanced productivity of industrial manufacturing is achieved by increasing automation and by developing new types of industrial tools based on well controlled electric drives. The recent development in microelectronics and information technology enables the use of mechanical structures and electric motors which are more simple than before. Today's digital signal processors and advanced digital control give opportunities to utilize even strongly non-linear electromechanical phenomena with an electrically produced driving force. The flux controlled induction motor drives replacing direct current motor drives even in most demanding applications are a very good example of this trend.

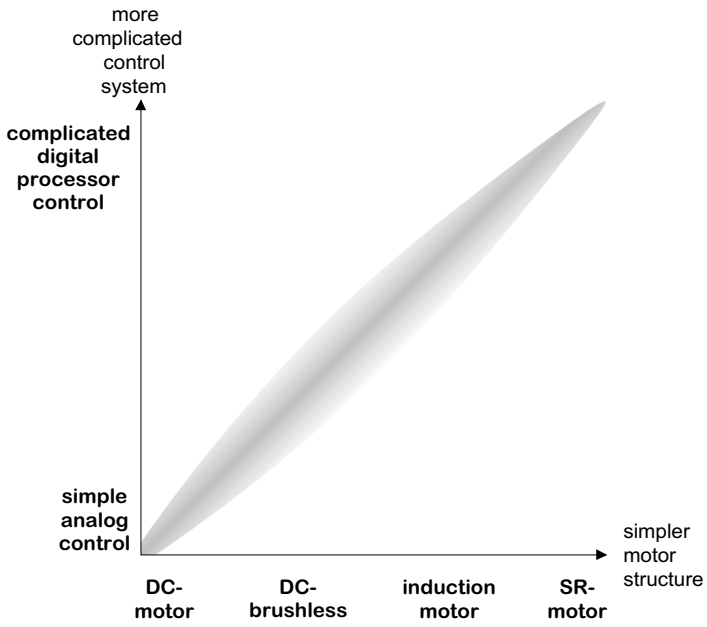

Figure 1.1. Comparison between motor structures and control systems.

The development of speed controlled electric motor drives can be seen in figure 1.1. At first there was a complex DC-motor (Direct Current motor) with many coils and poles. Analog PID-controllers were used to control armature DC-voltage by the rectifier firing angle. Nowadays the switched reluctance motor (SR-motor) has simple coils on laminated iron stator poles and a laminated iron rotor without coils at all. On the other side this simplicity requires the use of a

complicated digital control to handle the non-linear production of the torque of an SR-motor (Switched Reluctance motor).

Harris and Miller (1991), Miller (1993), Lovatt, McClelland and Stephenson (1997) have made comparative studies between the SR and other types of rotating electric motors. They concluded that the SR-motor has some more performance potential than the other types of electric motors, when middle power and steady normal speed (1500 rpm) are used. The specific torque per air gap volume of the SR-motor is a little bit higher than in the other types of rotating electric motors.

In industrial systems the Switched Reluctance technology is maybe best suited for low or zero speed applications where the power can be small but the torque or the force in the linear movement case might be relatively high. High power synchronous and induction technologies usually have difficulties when low or zero speed is used. An SR-motor can easily be locked at standstill like stepper motors. The SR-motor can be an attractive choice for well controlled low speed drive applications. The simple structure of the SR-motor makes it an alternative for low power applications, where pneumatic or hydraulic linear drives are to be avoided as far as reliability, usability and durability are concerned.

1.1 Objectives of the study

The main goals of this thesis are:

- To develop a basic design method of the linear movement SR-motor (LSR-motor).
- To evaluate comparatively the four basic LSR-motor structures and the effect of the various design parameters on the traction force production.
- To develop the basic transversal flux pole pair (BTFPP) model using the two-dimensional finite element calculation as a tool for the basic design process.
- To design the flowchart of the basic dimensional design.

1.2 An appraisal of linear movement electric drives described in the literature

The common way to produce linear movement by means of a rotating electric motor is to convert the rotation of the shaft by plunger rods, ball screws, gears and belt systems. Electromagnetic devices producing linear movement without any additional transmission system are called direct drives. The direct drive linear electric machine can be considered as an unrolled version of its cylindrical counterpart as the direct current motor (DC-motor), permanent magnet motor (PM-motor), induction motor, stepper motor, synchronous motor, synchronous reluctance motor and switched reluctance motor (SR-motor). Linear electric motors often are lacking some of the power factor, performance and efficiency expected from their rotary counterparts, because of the open structure with end effects and increased mass of the mover when compared to the rotor. The reduction of performance can be accepted if it is compensated by convenience and robustness. The size of a direct linear drive with no gears may be smaller than that of a conventional motor and gear combination producing the linear movement. The friction of the moving elements of the linear drive is reduced or eliminated when the direct linear drive is used. The feedback element can be directly coupled to the load, which improves the positioning accuracy and repeatability of the system. Some applications might not be possible without an electric linear drive.

One of the most comprehensive studies of electric linear drives is a paper written by G.W. McLean (1988) where he reviewed the industrial and transport applications and introduced methods to analyse and design them. He described the linear induction motors for conveyer applications providing linear, reciprocating and circular motion. Linear induction motors have been used also for metal handling in metal industry. Linear electric motors can provide levitation and propulsion when e.g. steel plates are transferred from one place to another during different processing stages in a mill. Conventional conveyers might not be needed. Linear induction motors seem to be well suited for conveyer systems such as those in automatic warehouses.

Edwards, Preston and Williams (1987) explained the use of a linear synchronous reluctance motor for metal handling. Motor and carrier vehicles (barriers) form a kind of conveyer. This application is advantageous when handling toxins or pathogens, or when maintaining sterile conditions. A contactless conveyer can be made of a linear motor by using magnetic levitation and propulsion.

Hayashiya, Katayama, Ohsaki and Masada (1997) investigated the non-contact conveyance method using a linear induction motor in order to improve the surface quality of a steel plate. Electromagnets were used for the suspension and levitation to carry the plates. A linear induction motor was used for the propulsion.

The food industry can use linear electric motors to increase product quality. The electric linear motor may be a substitute for the conventional conveyer system. Imal and Williams (1994) described such a system for a linear synchronous reluctance motor to move hollow cans which are moved from one place to another during different processing stages in a food factory. The primary of that motor is a normal three-phase AC-winding while each hollow ferromagnetic can forms a moving secondary.

Linear synchronous motors have been used mostly in transport applications. McLean lists many experimental high speed (over 500 km/h) railroads with steep gradients and magnetically levitated vehicles without friction between the rail and the vehicle. Linear induction motors represent often the rival technology in the magnetically levitated and propelled railroad called MAGLEV. The MAGLEV is an example of a technology that can not be utilised by conventional rails and motors driving steel wheels.

The linear DC-motor is relatively uncommon because it is expensive to manufacture. It can provide very smooth movements and a good controllability that can be compared to that of the rotating DC-motor. Linear DC-motors have been used in some machine tool XY-tables and computer peripherals.

Ben Yahia and Henneberger (1998) studied the magnetically levitated system using a linear direct drive for the high speed machine tool. The magnetic levitation technique combined with a linear movement permanent magnet synchronous motor makes frictionless operation of a machine tool table possible.

Roubicek, Pejsek and Podzimek (1988) described several types of electric linear drives such as an oscillatory synchronous linear drive of the feeder of bulky material, an oscillatory synchronous reluctance linear drive of a liquid extractor, a stepping linear drive of a manipulator of an

automatic welding machine and the linear DC-drive of an equipment used in the precision manufacturing of components. They stated electric linear drives having properties such as mechanical simplicity and reliability, good dynamic properties, savings in constructional materials, of space and energy, extension of service life of the working parts, low noise level and negligible maintenance when compared to the other technologies available.

Fast acting electric solenoid valves are used in mechatronics. The electric actuator is often a reluctance type linear electric actuator in the servo valves used to control the hydraulics. Abrahamsen, Ennemark and Jensen (1994) described the electromagnetic model for such a device. They were able to combine in their model non-linear magnetics including iron losses, the electric circuit and the mechanical side.

The servo valve studied by Abrahamsen, Ennemark and Jensen (1994) was a conventional solenoid valve. Evans, Smith and Ketteleborough (1997) described a new type of servo valve using a linear permanent magnet reluctance motor. They studied the design and optimisation methods for the motor. Their prototype validated the proposed design.

The control rod drives (CRD) in nuclear reactors are a good example of an application where reliability is the key feature of the drive system. At present most of the CRD's are based on conventional rotary electric motors, reduction gears and a holding mechanism as a mechanical part. Khan and Ivanov (1994) presented the linear step motor as a CRD. They found it to have a fast response, a high position accuracy and a wide speed range. The linear step motor CRD also simplifies a great deal of the mechanics needed when compared to the conventional CRD's thus enhancing the reliability of CRD-system.

Many electric linear motor configurations may potentially be applied to linear compressors. Redlich, Unger and Van der Walt (1996) found permanent magnet type linear motors to be a feasible solution for a free piston linear compressor. They described the moving coil and the moving magnet type PM-linear motor and they also considered design restrictions such as cost, size and efficiency.

Linear motor technologies have variants coming from all conventional rotating electric machines. They and their applications seem to have the same kind of relation than the rotating machines. Table 1.1. has beeen derived to show some of the linear motor technologies and application properties.

Table 1.1. Commonly used linear motor technologies and characteristics. Applications colum is added in order to have some kind of image for required traction force, speed and stroke length.

Technology	Speed	Force	Stroke length	Applications
Synchronous	medium high	high	free	transport, railroad, conveyers
Induction	medium high	high medium	free	transport, railroad, conveyers
Permanent magnet	low zero	weak medium	mostly limited	mechatronics, automation devices, robot technology
SR (variable reluctance)	low zero	weak medium	free mostly limited	transport, mechatronics, automation devices, robot technology
Stepper	low zero	weak	free mostly limited	mechatronics, automation devices, control devices, tools
DC	medium low	weak	limited	tools, high precision devices

1.3 The need for numerical models

Theoretically all electromagnetic field problems can be solved by utilising Maxwell's equations which are partial differential equations. They can be solved analytically when a set of boundary conditions strict enough are defined. These boundary conditions may be geometrical, constructional, electrical and mechanical. Analytical solutions require electrically and magnetically homogenous linear material, no movements of electric or magnetic bodies are allowed. These restrictions limit the analytical solutions of a field problem to very simple constructions which are of minor practical use.

Scientists have developed very efficient computer codes to solve field problems numerically by computers. The difficulty, size and complexity of the field problem is limited by the available computer resources. The most common computer code used for the solving of electromagnetic field problems is the finite element method (FEM).

The FEM-analysis of any three-dimensional moving electromagnetic devices coupled to the electric circuitry and to the mechanical system is still far away from every-day practical engineering work. Other numerical models are needed to fulfil the lack of computer resources when solving field problems. These numerical models are not global and they are good and rapid only for problems of the same type as the problem for which they were developed. A good example of a simplified model is the steady state equivalent circuit of the induction machine. Practical numerical models of this type are also needed to facilitate proper design and simulation of a linear electric drive in a reasonable time.

1.4 Scope of the thesis

The basic parts of the LSR-motors are the two-mover poles and stator pole as it will be seen later. Most of this study analyses the basic part of the linear movement transversal flux switched reluctance motor (TF-LSR-motor). Static properties of the basic pole pair are modelled and the basic design rules are derived. Some remarks about the modelling of the dynamic effects are given. The developed models are validated with experiments. The prototype of the one-sided one-pole-pair transversal flux switched reluctance linear motor is demonstrated and its static properties are measured.

The basis for the design of the rotating electric motors is the output equation linking the air gap volume of the motor to the electric and the magnetic loading giving the nominal torque. LSR-motors do not have such an output equation. The basis for the design of a LSR-motor is the required traction force which is a function of the cross-sectional area of the poles and the magnetomotive force in the coil of the stator pole. The traction force production is estimated with the two-dimensional finite element method applied to the basic transversal flux pole pair (BTFPP) model.

The magnetomotive force used is so high that the traction force grows nearly constantly with the magnetomotive force, due to which the length of the air gap is not as important as the cross-sectional area and the magnetomotive force.

1.5 Description of the thesis

The motivation and goals for this work are given in chapter 1. Also a wide range of linear electric drive applications found in literature are presented. A summary of the range of speed, power and linear electric drive technologies is shown in table 1.1. at the end of chapter 1.2.

An overview of the Switched Reluctance technology and the four basic constructions of the linear movement switched reluctance motors are given in chapter 2. There are two ways of guiding the main flux, the longitudinal and the transversal construction, two alternatives which fundamentally group the LSR-motor structures into different types. The two-mover poles and one-stator pole system as the basic part of the transversal flux LSR-motor is illustrated in chapter 2.

The equations needed for the basic design of linear SR-motors are derived in chapter 3. As a result of the comparison between the four basic LSR-motor structures the four-sided transversal flux LSR-motor is chosen for closer study.

The modelling methods for the static and the dynamic modelling of the LSR-motor properties are presented in chapter 4.

The finite element models of the two-dimensional and three-dimensional static magnetic field problems are shown in chapter 5 with the flowchart of the design process of the TF-LSR-motor for traction force production. The calculation results and measured results from the laboratory prototype are also explained in chapter 5.

The conclusions of the study are described in chapter 6.

2 SWITCHED RELUCTANCE TECHNOLOGY - AN OVERVIEW

An overview of the switched reluctance technology and possible structures for a linear movement SR-motor given in this chapter. Transversal flux machines are found to be suitable for a new type of linear SR-motor.

One definition of a switched reluctance motor states that it is a brushless, variable reluctance electric machine with an electronically commutated stator side. It consist of a salient stator and rotor structure, and of separated windings on the stator poles. According to Miller (1993. p. 1) "*A reluctance motor is an electric motor in which torque (or force) is produced by tendency of its moveable part to move to a position where the inductance of the excited winding is maximised. The motion may be rotary or linear, and the rotor may be interior or exterior.*" The SR-motor is constructed of separate electromagnets of phases which are excited one after another. The rotor position determines the right moments for the starting and finishing of the exciting periods for each phase. A three-phase SR-motor having six stator poles and four rotor poles, and with one leg of an inverter supplying the SR-motor phase is shown in figure 2.1.

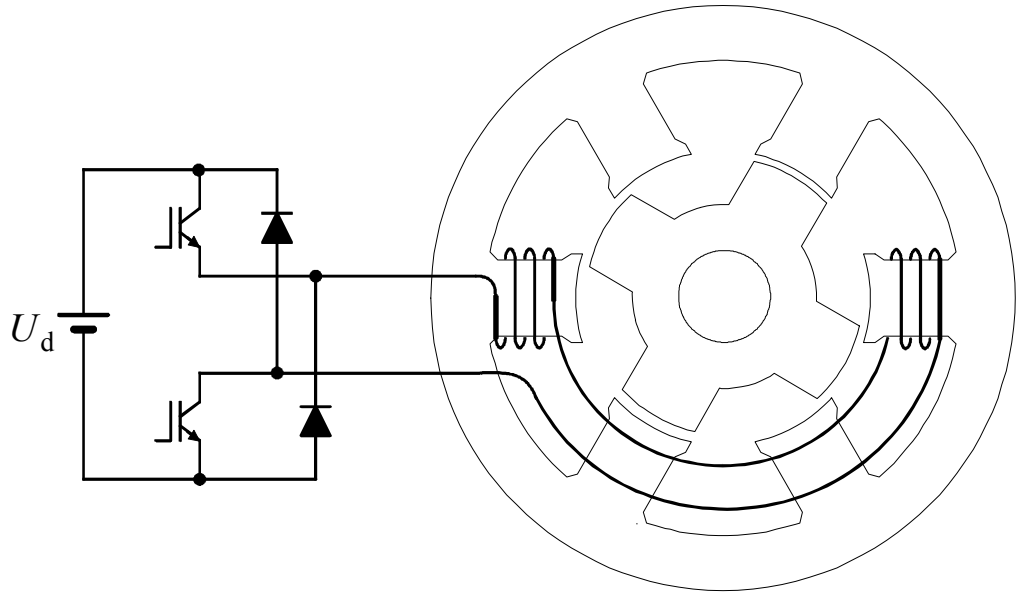

Figure 2.1. A three-phase 6/4-SR-motor, in which one phase of the motor is supplied by one leg of the inverter. The connections between phase winding and power switches of the inverter leg are shown. U_d is the DC-link voltage of the inverter.

Because of the excitation method, the SR-motor always needs a converter to supply the electric energy. The SR-motor can not generally operate directly from a direct current source (DC) or an alternating current (AC) source. The position of the rotor must be known in order to select the right moments for excitation of each of the corresponding phases. There has to be an absolute position transducer for the rotor position, or the position of the rotor has to be calculated from the other measured values.

The position of the rotor with respect to poles A-A' in figure 2.2a. is called “the aligned position” and the position of the rotor in figure 2.2b. is called “the unaligned position“. The rotor poles and the stator poles of phase A-A’ are overlapping each other completely at the aligned position and therefore the air gap and the reluctance of the overlapping poles have their minimum values. The air gap and the reluctance have their maximum values at unaligned position of phase A-A', and also the distance between the rotor poles and the stator poles has its maximum value at this point.

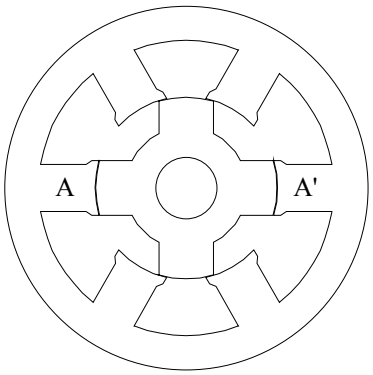

Figure 2.2a. The rotor in aligned position at phase A-A' .

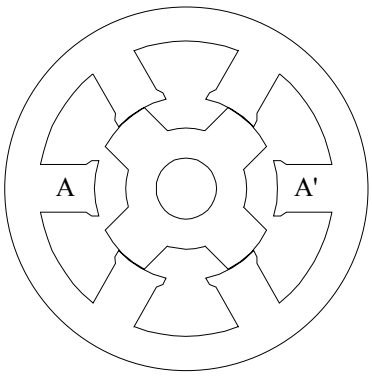

Figure 2.2b. The rotor in unaligned position at phase A-A' .

An SR-motor is one of the simplest electric machines when considering the electric and mechanical properties. However, controlling the SR-motor is very difficult. The air gap flux of the SR-motor is not sinusoidal as in induction and synchronous machines. The magnetic circuit of the SR-motor changes continuously and it is strongly non-linear when the rotor turns. There is a heavy local saturation at the edges of the overlapping stator and rotor poles causing the mag-

netic circuit of the SR-motor to operate continuously more or less in a saturated stage. There is no general analytical model for SR-motors. Each SR-motor has to be modelled by using numerical methods or by constructing prototypes and measuring them (Salo, 1996a).

SR-motors perform well at zero and low rotating speeds. Periodic use of rotating electric drives is very common in applications operating below 1000 rpm. Periodic use consists of starts, accelerations, steady speed runs, braking and holdings in position. Usability, durability, starting and maximum torque are more significant factors than efficiency, which is important especially in the constant speed drives having a long running time per year. SR-motors seem to be the most suitable choice for drives in which high dynamic performance at low or zero speed is required (Silventoinen, 1999).

Since the very first commonly known publication by Lawrenson, Stephenson, Blenkinsop, Corda, and Fulton (1980), SR-motor technology has been a subject of a world-wide research. Numerous papers concerning aspects of the SR-motors have been published. Prof. T. J. E. Miller has gathered up a great deal of SR-machine knowledge to his textbook "Switched Reluctance Motors and their Control" (1993). In Miller's book, there is a comprehensive listing of rotating SR-machine structures and design rules.

2.1 Linear movement SR-motor structures

There are several possible magnetic circuit structures suitable for a linear SR-motor. When the simplicity of the structure is a key factor, the one-pole-pair per phase and the three, four or five phase designs are preferable. The three-phase motor provides the greatest peak traction force of a pole and the five-phase motor with the same motor volume can give the smoothest traction force. The two alternatives for the main flux path described in figure 2.3. are the longitudinal flux magnetic circuit construction and the transversal flux magnetic circuit construction.

It can be seen in figure 2.3. that the back iron of the stator and the mover of the longitudinal construction is not needed in transversal flux construction (figure 2.3b.). Because of this the amount of the mover iron of the tranversal flux constructionis is much less than the mover iron of the longitudinal flux construction. The poles and phases of the transversal flux construction

are separated, while there is always some mutual magnetic coupling between the different phases of the longitudinal flux construction.

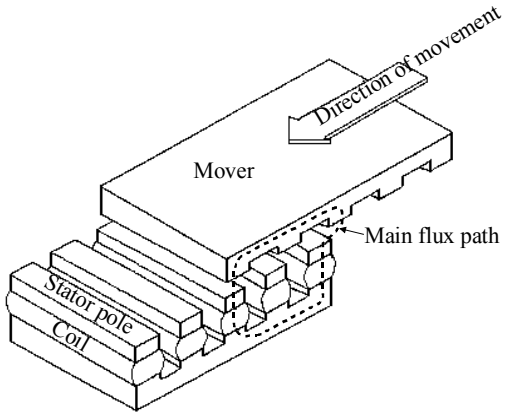

Figure 2.3a. A longitudinal flux design linear SR-motor (Adamiak & al., 1987. p. 40).

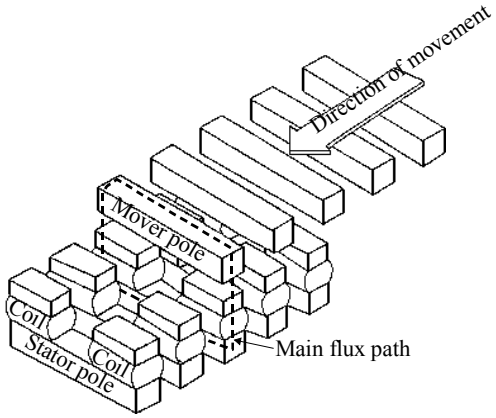

Figure 2.3b. A transversal flux design linear SR-motor (Adamiak & al., 1987. p. 40).

Normally the mover is the moving part and the stator is the fixed part, see figure 2.3. Coils are then wound on the stator poles. However, when the travelling distance is long and the moving vehicle is short, the moving part may have coils. The terms active track, passive shuttle and passive track, active shuttle are used in the MAGLEV railroad technology.

The positions of the mover of the LSR-motors have special meanings. The position of the mover in which the active stator pole has an equal distance to two-mover poles is called "the unaligned position". The unaligned position of the mover is shown in figure 2.4a. The position of the mover in which the stator and the mover poles are just to start overlapping and the edges of the active stator and the active mover poles are in line is called "the edge position". The edge position of the mover is shown in figure 2.4b. The position of the mover in which the stator and the mover poles are totally overlapping each other is called "the aligned position". The aligned position of the mover is shown in figure 2.4c. The traction force F_t is produced when the magnetised stator pole and the mover pole are attracting each other. There can never be a repulsion force, because there is no active magnetising in the mover.

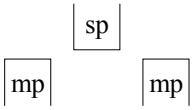

Figure 2.4a. The unaligned position of the mover. sp indicates the stator pole and mp indicates the mover pole. No traction force is generated in the unaligned position, but a weak normal force is generated.

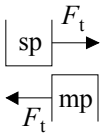

Figure 2.4b. The edge position of the mover. The traction force F_t and normal force are almost the same.

Figure 2.4c. The aligned position of the mover. No traction force is generated in the aligned position, but a high normal force is generated, which can be about 10 times the maximum traction force in the edge position.

2.1.1 Longitudinal main flux structure of the magnetic circuit

The longitudinal magnetic circuit structure is commonly used in rotating SR-motors, and the longitudinal flux linear SR-motor is an unrolled version of the normal rotating SR-motor.

The magnetic circuit design in figure 2.3. is said to be one-sided, which is the simplest possible structure. The one-sided design has a severe normal force problem when magnetised poles are attracting each other. Totally overlapped poles in aligned position can create a large normal force towards pole face, and at the same time there is no traction force at all. The one-sided structure needs a strong bearing system to overcome the normal force problem. Hence, the one-sided SR-linear motor is not very practical.

If the one-sided structure is copied and mirrored in respect to the mover back iron, we have a two-sided structure, such as the three-phase SR-linear motor described in figure 2.5. The normal forces are balanced in the two-sided structure, and the bearings are designed to carry only the mass of the mover and the possible load. The possible effects of manufacturing imperfections are not concidered here.

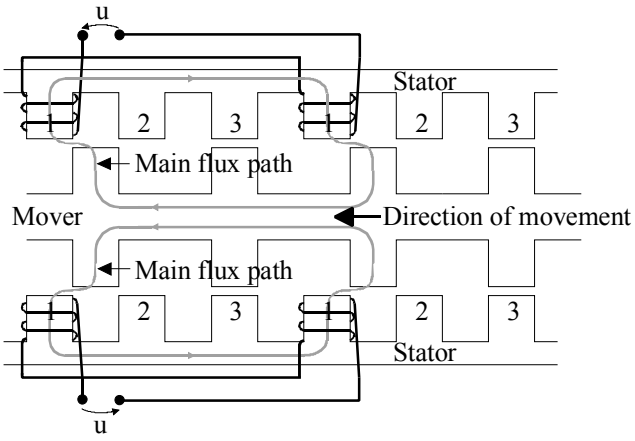

Figure 2.5. A two-sided three-phase longitudinal flux linear SR-motor. Only phase one is shown with coils. The main flux paths of the excited phase one are also shown. The numbered poles show the corresponding phase.

The flux paths may be short in the longitudinal flux SR-motors in which there are more than one-stator pole per phase. A few possibilities for rotational SR-motors are described in Miller's textbook (1993. p. 36-45).

When more sides are added to the basic construction the final possible geometry is round. This is called the cylindrical or the tubular construction depending on the mover. Corda and Skopljak (1993) introduced a tubular geometry longitudinal flux linear SR-motor in which the stator of the motor consists of phase sets allowing the short flux paths shown in figure 2.6. This structure has been examined by Corda and Wilkinson (1994), (1995) and (1996) and they have found the tubular longitudinal flux linear SR-motor to be a reasonable solution for a linear electric drive.

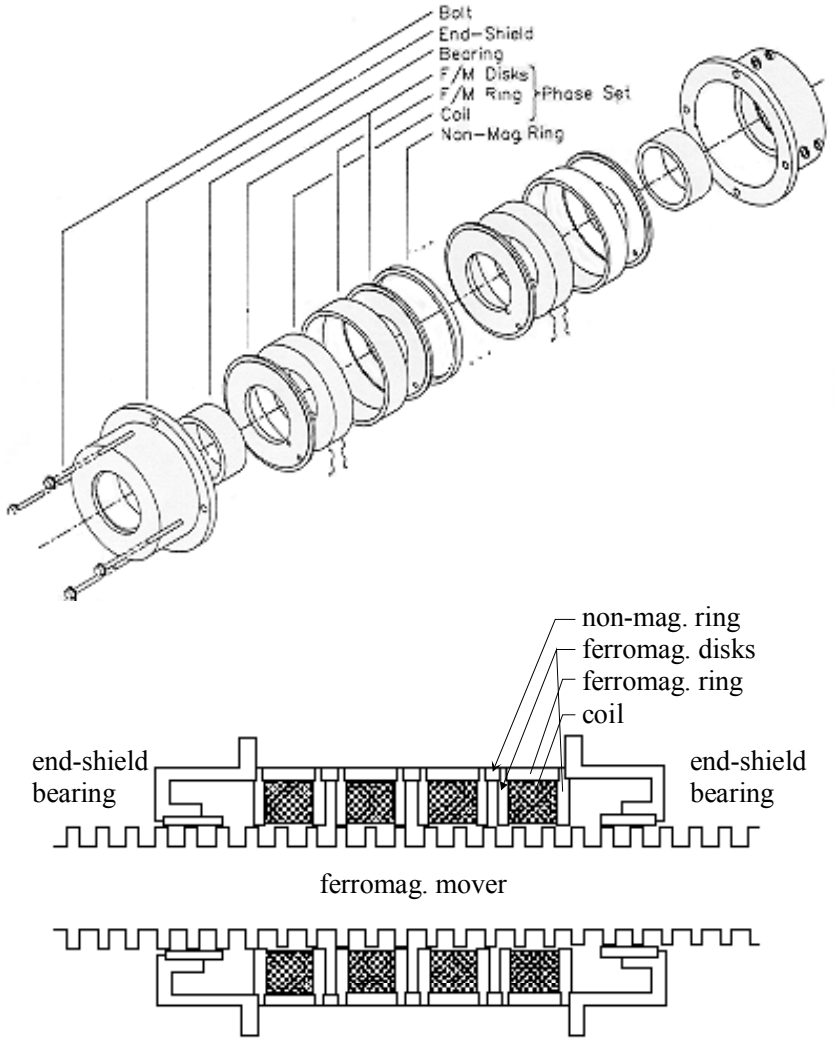

Figure 2.6. A tubular four-phase linear SR-motor (Corda, Skopljak, 1993. p. 536). Upper picture shows the phase sets and their assembly. Lower picture shows a through sectional cut with the ferromagnetic mover.

2.1.2 Transversal main flux structure of the magnetic circuit

The one-sided transversal flux linear SR-motor (see in figure 2.3b.) has pole windings divided into the two legs of the stator pole. Figure 2.7. shows an alternative solution where the winding is wound on the stator back iron.

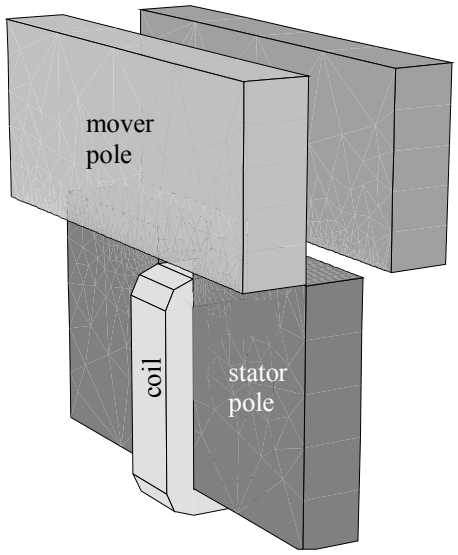

Figure 2.7. The basic two-mover poles and one-stator pole transversal flux linear SR-motor with vertical coil.

Figure 2.7. illustrates the basic two-mover poles and one-stator pole transversal flux linear SR-motor. The concentrated coil on the stator back iron gives some freedom in construction. The depth of the winding window is determined by the space between the two stator poles of different phases. The needed cross-sectional area of the copper coil is obtained by adjusting the length of the winding window. The amount of copper required remains the same regardless the winding arrangemets. The coils are maybe easier to cool when they are divided into horizontal coils on two legs of the stator pole as shown in figure 2.3b. and in figure 5.42. The stray flux through the winding window and in the coil regions with the horizontal coil is smaller than in the case of figure 2.7. On the other hand, the concentrated coil in figure 2.7. leaves the stator pole legs free for fastening purposes. This simplifies the construction especially in a four sided tansversal flux linear motor.

Again, the one-sided magnetic circuit structure is not very practical because of the normal forces between the stator and the mover poles. The one-sided rectangular structure can be expanded for example to two- and four-sided structures. The stator pole design remains the same but the mover poles in the four sides share the same back iron, thus creating a common mover pole for all four stator poles of the stator phase. The magnetic parts of the five-phase the four-sided

transversal flux linear SR-motor with coils is illustrated in figure 2.8. The normal forces are balanced. There is some space left for bearings in every corner of the mover pole.

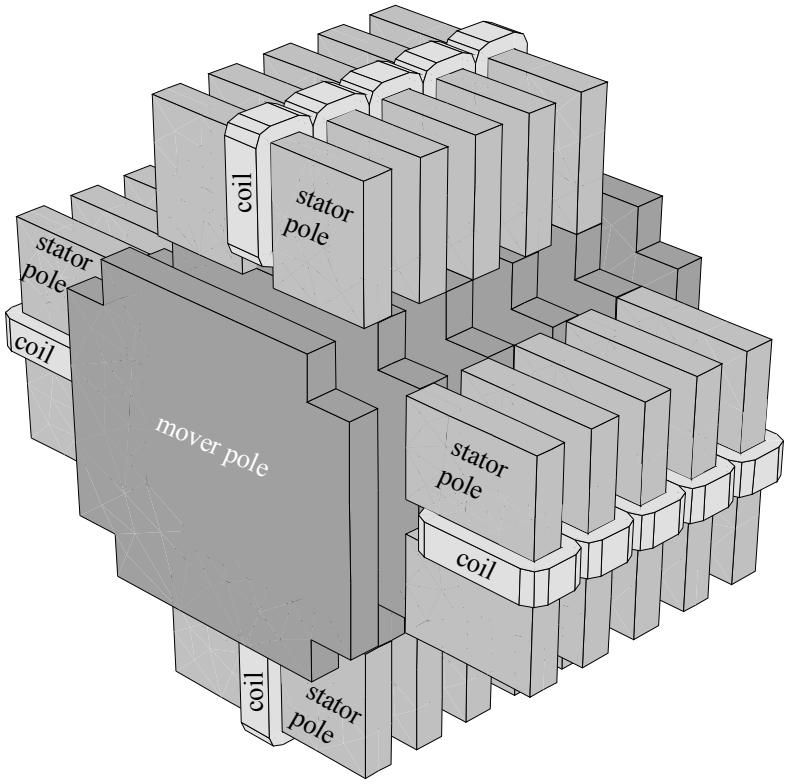

Figure 2.8. A five-phase four-sided transversal flux linear SR-motor.

The transversal flux design can also be cylindrical. Figure 2.9. illustrates the cylindrical transversal flux linear SR-motor, in which only one-stator phase and one mover pole are shown. The mover in figure 2.9. is cylindrical while the stator poles remain rectangular in the other sides. The pole edge of the stator pole towards the mover has the same cylindrical geometry than as the mover.

The basic one-stator pole and two-mover poles transversal flux linear SR-motor is found in all transversal flux designs. This basic part is the starting point for the design of a transversal flux linear SR-motor from which the design equations can be derived.

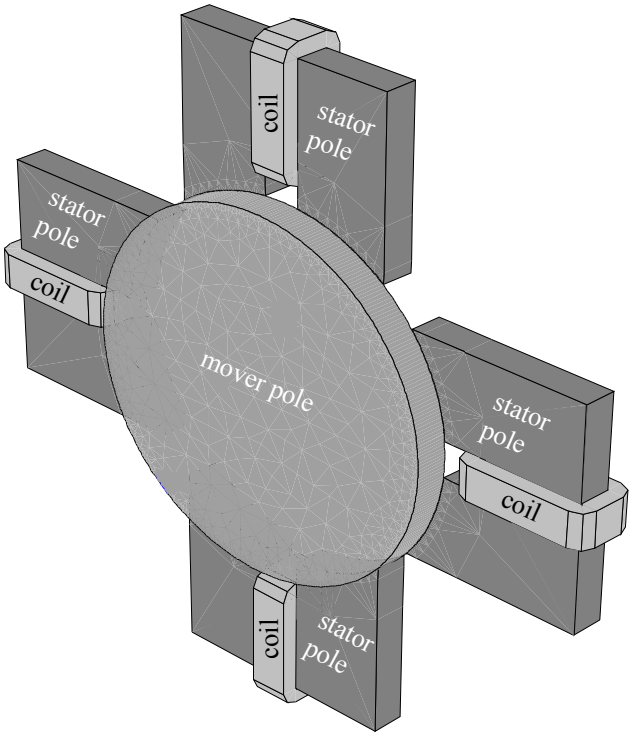

Figure 2.9. A cylindrical mover four-sided stator transversal flux linear SR-motor. Only one phase is shown with one mover pole in the edge position.

2.2 Conclusions from the switched reluctance technology

Switched reluctance motor is an old invention which may now rise to a possible technology for a new type of electric drives such as the linear electric motor. There are many possibilities for the magnetic circuit structure, but the transversal flux technique might be a good solution in terms of moving iron mass.

The presented main solutions for magnetic structures are examined in the following chapter. The introduced basic transversal flux pole pair is used as a basis for the modelling work.

3 DIMENSIONING OF LINEAR SR-MOTORS

There are unlimited possibilities to choose phase and pole number combinations and pole geometries for a linear SR-motor. The four most basic structures with phase numbers three, four and five are examined here.

1. One- and four-sided transversal flux linear SR-motors including poles with rectangular geometry (TF-LSR-motor).
2. One- and two-sided longitudinal flux linear SR-motors including poles with rectangular geometry (LF-LSR-motor).
3. Four-sided transversal flux linear SR-motor including poles with cylindrical geometry (TF-CLSR-motor).
4. Longitudinal flux linear SR-motor including poles with tubular geometry (LF-TLSR-motor).

Equations for all the basic dimensions of the magnetic circuit parts are derived. The required suspension or bearing devices or other mechanical systems needed are not considered. The dimensional design equations are derived to be functions of the cross-sectional pole face area A, of the magnetomotive force (MMF, total current in the pole winding) Θ, of the current density J, of the pole width t, of the phase number m, of the stroke distance of the mover L_{str}, of the winding fill factor k_{w}, and of the air gap length δ.

All designs have few common dimensional constraints which can be seen in figure 3.1.:

- The width of stator poles and the mover poles is equal.
- The distance between two-stator poles are equal to the pole width.
- The minimum length of the whole linear SR-motor is an electrical length determined by phase number.

- The portion of stray flux is assumed to be small, thus the effects of the stray flux are ignored in the dimensioning equations.
- The pole width *t* is chosen in a way that the combination of *t* and pole length *l* produces the minimum mass of the mover.

The first constraint is required in order to avoid dead zones in traction force production (Salo, 1996). If the stator pole and the mover pole have an uneven width, there is a zone in which the reluctance is not changing, thus there is no traction force production.

The second constraint is a combination of the traction force production and the amount of copper which is possible to put on the coil. The larger the distance between the two-stator poles, the larger the available winding space becomes and the smaller the copper power losses.

The useful traction force production starts from the edge position. If the distance between the two-stator poles is larger than the pole width, then the distance between the unaligned position and the edge position is larger than in the case when the distance between the two-stator poles is equal to the pole width. The mover has to travel further before a useful traction force can be generated than is the case when the distance between the two-stator poles is equal to the pole width. This decreases the mean traction force available and the traction force waveform is more peaky (Salo, 1996b. p. 4-16).

If the distance between the two-stator poles is smaller than the pole width, then the unaligned reluctance is smaller than is the case when the distance between the two-stator poles is equal to the pole width. This decreases available peak traction force. The maximum peak traction force of the one-pole pair with some current density is obtained when the distance between the two-stator poles is equal to the pole width (Salo, 1996b. p. 4-16).

The third constraint classifies the device between a linear movement motor and an actuator. An actuator has a small limited stroke distance and only few-stator poles are needed when the movement distance is less than the electrical length of the actuator.

The fourth constraint is derived from the idea that the effect of the stray flux on the traction force production is rather small. The stator poles are almost magnetically uncoupled and the stray flux paths are not going through the air gaps of the other stator poles which may produce an opposite traction force. The presence of the stray flux increases the required magnetomotive force due to which there are more copper losses.

The fifth constraint is the key desing rule. The moving iron mass should be as small as possible and the whole motor structure must be sensible mechanically as well as magnetically.

The designer must decide the required traction force first. Then the cross-sectional area of the pole leg face and the total MMF are chosen from a data base like in figure 3.6., which may be obtained by doing field calculations with BTFPP-model presented in chapter 5.2.1. or by measuring an existing device. The iterative nature of the dimensioning process is shown in figure 5.31.

The current density J is also a parameter to be determined by the designer. It depends on the cooling method used for the windings and insulations. Some guidelines to choose the current density and the cooling method are given in the textbook of Hendershot (1994). A summary of the suitable current densities for electrical machines is given in table 3.1.

Table 3.1. Typical values of current densities used in motors cooled by different methods. Values in the table are adapted from the textbook of Hendershot (1994).

Cooling method	J [A/mm^2]
Totally enclosed natural air cooling	4.7…5.4
Totally enclosed, air over fan cooled	7.8…10.9
External blower, through cooled	14.0…15.5
Liquid cooled	23.3…31.0

The cooling of large pole windings is less efficient than that of smaller slot windings. The current density values in table 3.1. have to be decreased when the coil dimensions increase if the

cooling system remains the same. The heat transfer from the centre of the thick coil is not as good as in the case of the slot windings especially when round wire is used.

3.1 Basic design of a TF-LSR-motor

The basic one-sided TF-LSR-motor can be approached as follows. A system with a stator and two-mover poles is considered first and then the equations are expanded to the four-sided motor. The one-sided pole system is the basic constructional part of all motors in which poles have a rectangular geometry. The schematic view of the one-sided three-phase TF-LSR-motor is illustrated in figure 3.1. The geometrical definitions of the dimensions are also shown.

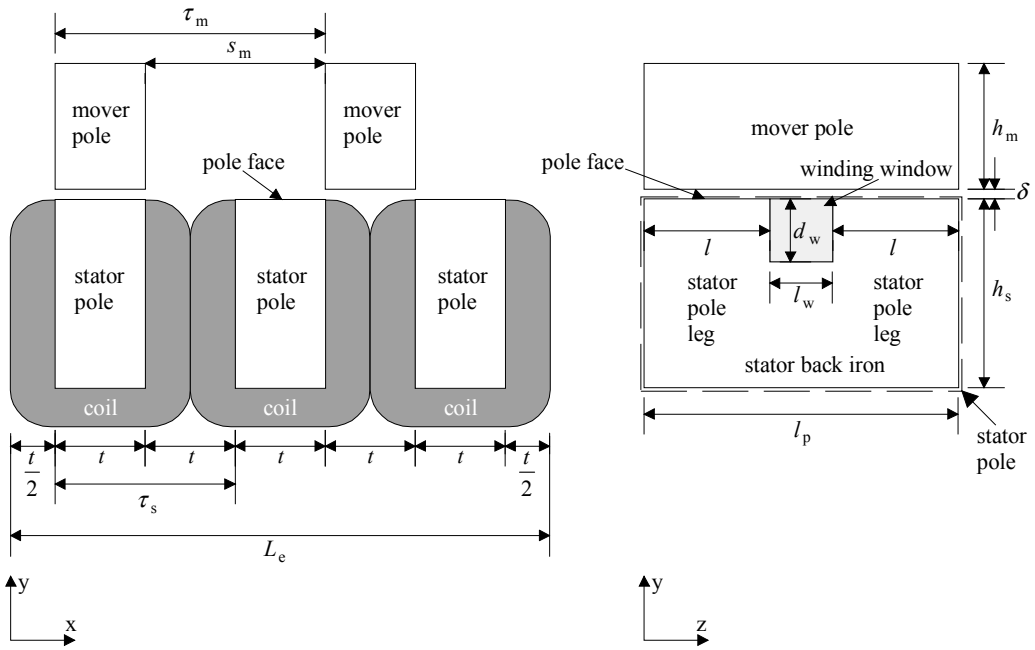

Figure 3.1. The schematic view of the one-sided three-phase TF-LSR-motor. Movement and traction force are assumed to be in x-direction. The most important geometrical dimension are shown. Left picture shows the through-sectional cut of the motor and right picture shows the cross-sectional cut of the motor.

The traction force F_t of a basic TF-LSR-motor pole system is a function of the cross-sectional area of the pole face A of the stator pole leg and the total magnetomotive force (total MMF, Ampere turns [A]) Θ

$$F_{\mathrm{t}} = f(A, \Theta) . \tag{3.1}$$

The cross-sectional pole face area is a product of the pole width t and the pole length l

$$A = t \cdot l . \tag{3.2}$$

Due to initial dimensional boundary condition the distance between the stator poles is equal to the pole width t. The stator pole pitch τ_{s} is then

$$\tau_{\mathrm{s}} = 2 \cdot t . \tag{3.3}$$

The electrical length L_{e} of the TF-LSR-motor is the product of the stator pole pitch and the phase number m. The electrical length counts stator length with coils in the direction of movement (see figure 3.1.)

$$L_{\mathrm{e}} = \tau_{\mathrm{s}} \cdot m = 2 \cdot t \cdot m . \tag{3.4}$$

The electrical length corresponds to the circle of the air gap radius in a rotating SR-motor. The mover pole pitch τ_{m} is then defined as

$$\tau_{\mathrm{m}} = \frac{L_{\mathrm{e}}}{m-1} = \frac{2 \cdot t \cdot m}{m-1} . \tag{3.5}$$

In a rotating SR-motor the rotor pole number is not allowed to be equal to the stator pole number. Similarly, the mover pole number p_{m} and the stator pole number p_{s} of the TF-LSR-motor are not allowed to be equal in terms of the electrical length. The stator pole number of the one-sided TF-LSR-motor p_{s1s} is equal to the phase number m of the TF-LSR-motor, if there is only one stator pole per phase

$$p_{\mathrm{s1s}} = m . \tag{3.6}$$

The mover pole number p_{m} depends on the electrical length, the stroke distance L_{str} of the mover, and the phase number. When the stroke distance is less than or equal to the electrical length of the TF-LSR-motor, the mover pole number is

$$p_{\mathrm{m}} = m-1, L_{\mathrm{str}} \le L_{\mathrm{e}}, \tag{3.7}$$

and when the stroke distance exceeds the electrical length, the mover pole number is

$$p_{\mathrm{m}} = \mathrm{ceil}\left\{\frac{L_{\mathrm{str}}}{\tau_{\mathrm{m}}}\right\} = \mathrm{ceil}\left\{L_{\mathrm{str}} \cdot \frac{m-1}{2 \cdot t \cdot m}\right\},\ L_{\mathrm{str}} > L_{\mathrm{e}}, \tag{3.8}$$

where the ceil function in equation (3.8) is defined to be the integer of the argument of the function ceil added by one.

The stator pole width and the mover pole width are equal. The distance between two mover poles s_{m} is then

$$s_{\mathrm{m}} = \tau_{\mathrm{m}} - t = t \cdot \frac{m+1}{m-1}. \tag{3.9}$$

The current density determines the minimum cross-sectional area of the winding copper A_{Cu}

$$A_{\mathrm{Cu}} = \frac{\Theta}{J}. \tag{3.10}$$

The windings cross-sectional area has to be multiplied by the inverse of the winding fill factor k_{w}. A common winding fill factor is approximately 0.6 if normal round wire is used. The winding fill factor might be in the range of 0.8 … 0.95 when a wire with rectangular profile is used. k_{w} includes the insulation of the wire. The minimum winding area A_{w} is then

$$A_{\mathrm{w}} = \frac{A_{\mathrm{Cu}}}{k_{\mathrm{w}}} = \frac{\Theta}{k_{\mathrm{w}} \cdot J}. \tag{3.11}$$

The depth of the winding window d_w is as large as half the space available for the winding between the stator poles. The distance between the stator poles is the pole width and there is a side of windings of two-stator poles in the slot between the stator poles. The depth of the winding window is then

$$d_w = \frac{t}{2}. \tag{3.12}$$

The length of the winding window l_w is determined by the winding area and by the depth of the winding window, but the minimum l_w should be at least pole width to limit the stray flux through the winding window

$$l_w = \frac{A_w}{d_w} = \frac{2 \cdot \Theta}{k_w \cdot J \cdot t}. \tag{3.13}$$

The transversal flux stator pole is a pole pair consisting of two poles with the same back iron and a winding window between the pole legs. The total stator pole length l_p is then

$$l_p = 2 \cdot l + l_w = \frac{2}{t} \cdot \left(A + \frac{\Theta}{k_w \cdot J} \right). \tag{3.14}$$

The flux that runs through the stator poles must also fit into the back iron of the stator pole. The stator pole height h_s is then the pole length added to the winding window depth

$$h_s = l + d_w = \frac{A}{t} + \frac{t}{2}. \tag{3.15}$$

There is no winding window in the mover pole, but the mover pole length is equal to the stator pole length. The mover pole height h_m is then

$$h_m = l = \frac{A}{t}. \tag{3.16}$$

It is possible to calculate the volume and the mass of the different magnetic parts and winding copper, if all the dimensions of the magnetic parts of the one-sided rectangular geometry transversal flux mover and the stator pole system are known. The volume of the mover pole V_{mp1} of the one-sided TF-LSR-motor is

$$V_{\mathrm{mp1}} = l_{\mathrm{p}} \cdot t \cdot h_{\mathrm{m}} = 2 \cdot \frac{A}{t} \cdot \left(A + \frac{\Theta}{k_{\mathrm{w}} \cdot J} \right). \tag{3.17}$$

The mover pole iron mass M_{mp} of the one-sided TF-LSR-motor is

$$M_{\mathrm{mp1}} = V_{\mathrm{mp1}} \cdot \rho_{\mathrm{Fe}} = 2 \cdot \rho_{\mathrm{Fe}} \cdot \frac{A}{t} \cdot \left(A + \frac{\Theta}{k_{\mathrm{w}} \cdot J} \right), \tag{3.18}$$

where ρ_{Fe} is the density of iron.

The total mass of the moving magnetic circuit parts M_{m1s} of the one-sided TF-LSR-motor is

$$M_{\mathrm{m1s}} = M_{\mathrm{mp1}} \cdot p_{\mathrm{m}} = 2 \cdot \rho_{\mathrm{Fe}} \cdot p_{\mathrm{m}} \cdot \frac{A}{t} \cdot \left(A + \frac{\Theta}{k_{\mathrm{w}} \cdot J} \right). \tag{3.19}$$

The iron volume of the stator pole pair with it's back iron V_{sp} is

$$V_{\mathrm{sp}} = l_{\mathrm{p}} \cdot h_{\mathrm{s}} \cdot t - A_{\mathrm{w}} \cdot t = A \cdot \left(\frac{2}{t} \cdot \left(A + \frac{\Theta}{k_{\mathrm{w}} \cdot J} \right) + t \right). \tag{3.20}$$

The stator pole iron mass M_{sp} is

$$M_{\mathrm{sp}} = V_{\mathrm{sp}} \cdot \rho_{\mathrm{Fe}} = \rho_{\mathrm{Fe}} \cdot A \cdot \left(\frac{2}{t} \cdot \left(A + \frac{\Theta}{k_{\mathrm{w}} \cdot J} \right) + t \right). \tag{3.21}$$

The copper volume of the stator pole winding V_{Cup} is

$$V_{\mathrm{Cup}} = 2\cdot(l+2\cdot t)\cdot A_{\mathrm{Cu}} = 2\cdot\frac{\Theta}{J}\cdot\left(2\cdot t+\frac{A}{t}\right). \tag{3.22}$$

The mass of the copper M_{Cup} of the winding of the stator pole is

$$M_{\mathrm{Cup}} = V_{\mathrm{cup}}\cdot\rho_{\mathrm{Cu}} = 2\cdot\rho_{\mathrm{Cu}}\cdot\frac{\Theta}{J}\cdot\left(2\cdot t+\frac{A}{t}\right), \tag{3.23}$$

where ρ_{Cu} is the density of copper.

The total mass of the one-sided TF-LSR-motor $M_{1\mathrm{s}}$ is thus

$$M_{1\mathrm{s}} = \left(M_{\mathrm{sp}}+M_{\mathrm{Cup}}\right)\cdot p_{\mathrm{s1s}} + M_{\mathrm{m1s}} = \left(M_{\mathrm{sp}}+M_{\mathrm{Cup}}\right)\cdot p_{\mathrm{s1s}} + M_{\mathrm{mp1}}\cdot p_{\mathrm{m}}. \tag{3.24}$$

The length of each side of the four-sided mover is equal to the total stator pole length l_{p} when the one-sided TF-LSR-motor is extended to a four-sided TF-LSR-motor. The four-sided TF-LSR-motor poles with rectangular geometry is shown in figure 3.2. A rectangular iron piece can be cut out from the centre of the four-sided mover pole. The area of the piece removed is l_{w}^2 and the volume of the four-sided mover pole V_{mp4} is

$$V_{\mathrm{mp4}} = (l_{\mathrm{p}}^2 - l_{\mathrm{w}}^2)\cdot t = 4\cdot\frac{A}{t}\cdot\left(A+2\cdot\frac{\Theta}{k_{\mathrm{w}}\cdot J}\right). \tag{3.25}$$

The mass of the four-sided mover pole M_{mp4} is

$$M_{\mathrm{mp4}} = V_{\mathrm{mp4}}\cdot\rho_{\mathrm{Fe}} = (l_{\mathrm{p}}^2 - l_{\mathrm{w}}^2)\cdot t\cdot\rho_{\mathrm{Fe}} = 4\cdot\rho_{\mathrm{Fe}}\cdot\frac{A}{t}\cdot\left(A+2\cdot\frac{\Theta}{k_{\mathrm{w}}\cdot J}\right). \tag{3.26}$$

The moving iron mass of the four-sided TF-LSR-motor is the mass of the total mover iron mass M_{m4s}. It depends on the pole number of the mover

$$M_{\mathrm{m4s}} = M_{\mathrm{mp4}} \cdot p_{\mathrm{m}} = 4 \cdot \rho_{\mathrm{Fe}} \cdot p_{\mathrm{m}} \cdot \frac{A}{t} \cdot \left(A + 2 \cdot \frac{\Theta}{k_{\mathrm{w}} \cdot J} \right). \tag{3.27}$$

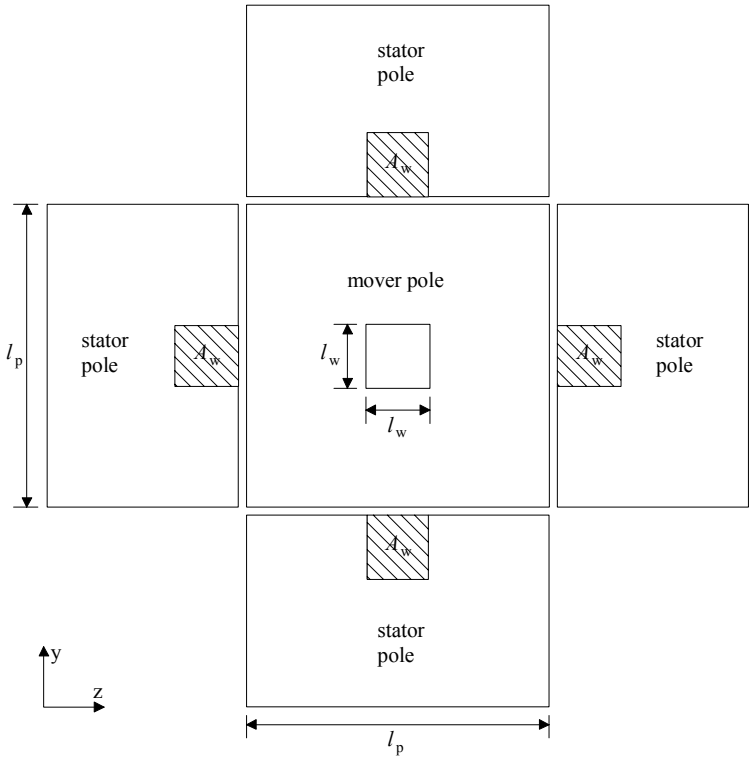

Figure 3.2. The schematic view of the four-sided TF-LSR-motor. A stator phase consists of four stator poles, one in each side of the four sided mover.

The traction force of the four-sided TF-LSR-motor is four times the traction force of the one-sided TF-LSR-motor if the stator pole design and windings remain the same. There is one-stator pole in each mover side. If there is only one-stator four-pole system per phase, the stator pole number of the four-sided TF-LSR-motor p_{s4s} is

$$p_{\mathrm{s4s}} = 4 \cdot p_{\mathrm{s1s}} = 4 \cdot m \,. \tag{3.28}$$

The total mass of the four-sided transversal flux SR-motor $M_{4\mathrm{s}}$ is

$$M_{4\mathrm{s}} = (M_{\mathrm{sp}} + M_{\mathrm{Cup}}) \cdot p_{\mathrm{s4s}} + M_{\mathrm{m4s}} = (M_{\mathrm{sp}} + M_{\mathrm{Cup}}) \cdot p_{\mathrm{s4s}} + M_{\mathrm{mp4}} \cdot p_{\mathrm{m}} \,. \tag{3.29}$$

3.2 Basic design of an LF-LSR-motor

Most of the equations for the TF-LSR-motor are valid also for the LF-LSR-motor. A schematic view of a two-sided three-phase LF-LSR-motor is shown in figure3.3.

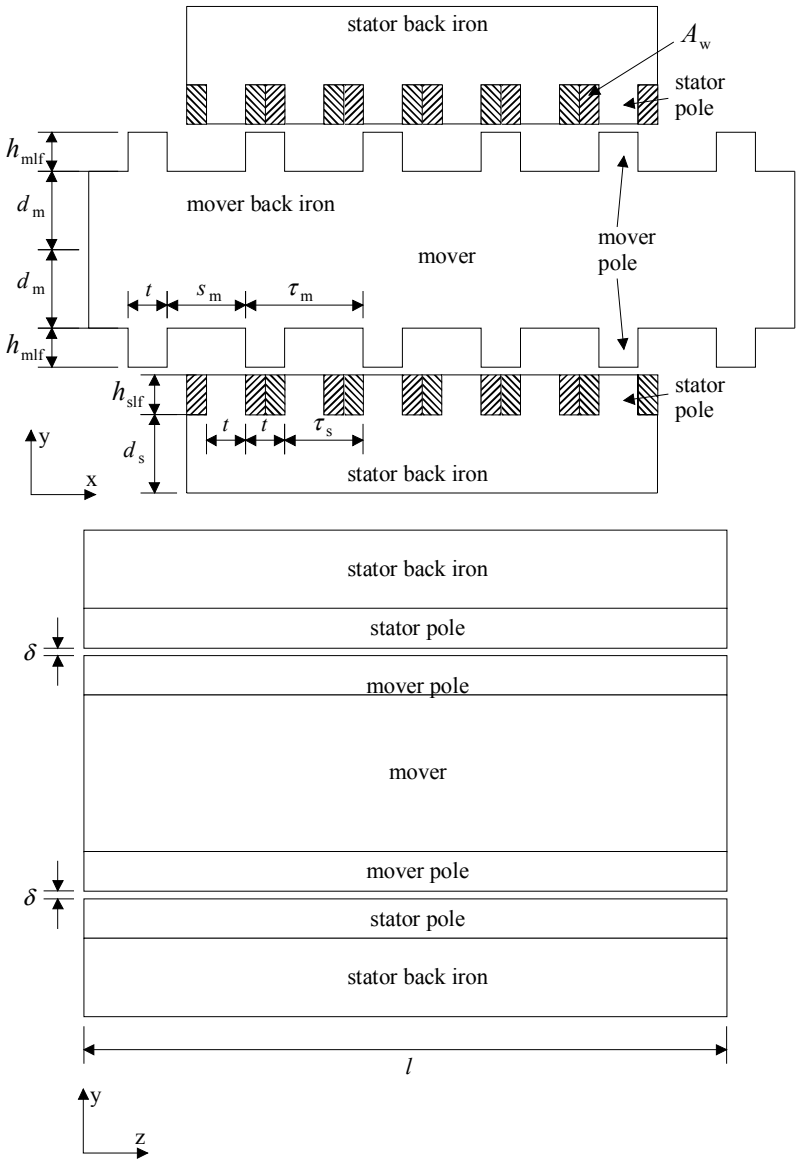

Figure 3.3. Schematic view of a two-sided three-phase LF-LSR-motor. Upper picture shows the through-sectional cut of the motor and lower pictures shows the cross-sectional cut of the motor.

The electrical length of the LF-LSR-motor is different than that of the TF-LSR-motor. This is because in the longitudinal flux configuration the cross-sectional area of the stator and mover poles and the total MMF is always divided into at least two pole pairs. The electrical length of the LF-LSR-motor L_{elf} is then

$$L_{\mathrm{elf}} = \tau_{\mathrm{s}} \cdot 2 \cdot m = 4 \cdot t \cdot m \,. \tag{3.30}$$

The mover pole pitch τ_{m} of the LF-LSR-motor is defined by considering also the longitudinal flux configuration

$$\tau_{\mathrm{m}} = \frac{L_{\mathrm{elf}}}{2 \cdot m - 2} = \frac{2 \cdot t \cdot m}{m - 1} \,. \tag{3.31}$$

When there are at least two-stator poles in the flux path, the stator pole number of the LF-LSR-motor p_{slf} is twice the phase number

$$p_{\mathrm{slf}} = 2 \cdot m \,. \tag{3.32}$$

When the stroke distance is less than or equal to the electrical length of the LF-LSR-motor, the mover pole number p_{mlf} of the LF-LSR-motor is

$$p_{\mathrm{mlf}} = 2 \cdot m - 2 = 2 \cdot (m - 1), \quad L_{\mathrm{str}} \le L_{\mathrm{elf}} \,, \tag{3.33}$$

and when the stroke distance exceeds the electrical length, the mover pole number is

$$p_{\mathrm{mlf}} = \mathrm{ceil}\left\{ \frac{L_{\mathrm{str}}}{\tau_{\mathrm{m}}} \right\} = \mathrm{ceil}\left\{ L_{\mathrm{str}} \cdot \frac{m - 1}{2 \cdot t \cdot m} \right\}, \; L_{\mathrm{str}} > L_{\mathrm{elf}} \quad . \tag{3.34}$$

Equations (3.8) and (3.34) are the same, but p_{m} and p_{mlf} are not, because L_{elf} is twice L_{e}, if t is the same for both TF-LSR-motor and LF-LSR-motor. When m is 3, p_{m} is 2 and p_{mlf} is 4.

The required winding space is defined in the same way for the LF-LSR-motor as for the TF-LSR-motor. The stator pole height and the stator back iron thickness are treated separately in the LF-LSR-motor. The windings are wound on the stator poles. The sides of two coils are in the space between the two-stator poles. The stator pole height h_{slf} of the LF-LSR-motor is determined by the required winding space

$$h_{\mathrm{slf}} = 2 \cdot \frac{A_{\mathrm{w}}}{t} = 2 \cdot \frac{\Theta}{k_{\mathrm{w}} \cdot J \cdot t} . \tag{3.35}$$

There might be fluxes of the two-stator phases at the same time in the stator back iron, especially when the mover is kept standing still with maximum load and two-phases is magnetised with the maximum total MMF. The thickness of the stator back iron d_{s} must be large enough to allow the simultaneous peak fluxes to pass through the stator back iron without more significant saturation in the back iron than in the stator poles. The thickness of the stator back iron must be at least twice the pole width. The same peak fluxes pass through the mover back iron as well. The mover back iron thickness d_{m} is also twice the pole width.

$$d_{\mathrm{s}} = d_{\mathrm{m}} = 2 \cdot t . \tag{3.36}$$

The minimum mover pole height h_{mlf} is determined to be at least two times the vertical distance between the mover and the stator pole in unaligned mover position for having enough separation between two mover poles. This "rule of thumb" can be adopted by Miller (1993. p. 168). Otherwice the stray flux between the stator pole and the mover back iron will be remarkable

$$h_{\mathrm{mlf}} = 2 \cdot \left(\frac{s_{\mathrm{m}} - t}{2} \right) = \tau_{\mathrm{m}} - 2 \cdot t = \frac{2 \cdot t}{m - 1} . \tag{3.37}$$

The mover volume V_{mlf} of the longitudinal flux linear SR-motor is then

$$V_{\mathrm{mlf}} = \left(t \cdot h_{\mathrm{mlf}} \cdot l + \tau_{\mathrm{m}} \cdot d_{\mathrm{m}} \cdot l \right) \cdot p_{\mathrm{mlf}} = 2 \cdot A \cdot p_{\mathrm{mlf}} \cdot t \cdot \frac{2 \cdot m + 1}{m - 1} . \tag{3.38}$$

The stator volume V_{slf} of LF-LSR-motor is

$$V_{\mathrm{slf}} = \left(t \cdot h_{\mathrm{slf}} \cdot l + \tau_{\mathrm{s}} \cdot d_{\mathrm{s}} \cdot l\right) \cdot p_{\mathrm{slf}} = 4 \cdot A \cdot m \cdot \left(2 \cdot t + \frac{\Theta}{k_{\mathrm{w}} \cdot J \cdot t}\right). \tag{3.39}$$

The total copper volume V_{clf} of LF-LSR-motor is

$$V_{\mathrm{clf}} = 2 \cdot (l + 2 \cdot t) \cdot A_{\mathrm{Cu}} \cdot p_{\mathrm{slf}} = 4 \cdot m \cdot \frac{\Theta}{J} \cdot \left(2 \cdot t + \frac{A}{t}\right). \tag{3.40}$$

The mass of the mover M_{mlf}, the mass of the stator M_{slf}, the mass of the copper M_{clf} and the mass of all magnetic parts M_{lf} of LF-LSR-motor are respectively

$$M_{\mathrm{mlf}} = V_{\mathrm{mlf}} \cdot \rho_{\mathrm{Fe}} = 2 \cdot \rho_{\mathrm{Fe}} \cdot A \cdot p_{\mathrm{mlf}} \cdot t \cdot \frac{2 \cdot m + 1}{m - 1}, \tag{3.41}$$

$$M_{\mathrm{slf}} = V_{\mathrm{slf}} \cdot \rho_{\mathrm{Fe}} = 4 \cdot \rho_{\mathrm{Fe}} \cdot A \cdot m \cdot \left(2 \cdot t + \frac{\Theta}{k_{\mathrm{w}} \cdot J \cdot t}\right), \tag{3.42}$$

$$M_{\mathrm{clf}} = V_{\mathrm{clf}} \cdot \rho_{\mathrm{cu}} = 4 \cdot \rho_{\mathrm{cu}} \cdot m \cdot \frac{\Theta}{J} \cdot \left(2 \cdot t + \frac{A}{t}\right), \tag{3.43}$$

$$M_{\mathrm{lf}} = M_{\mathrm{mlf}} + M_{\mathrm{slf}} + M_{\mathrm{clf}}. \tag{3.44}$$

The two-sided LF-LSR-motor is more practical than the one-sided LF-LSR-motor because of the balanced normal forces in the two-sided case. The two-sided LF-LSR-motor is obtained simply by mirroring and copying a one-sided design into a two-sided design in respect to the mover back iron.

The mass of the mover of the two-sided LF-LSR-motor M_{ml2} is

$$M_{\mathrm{ml2}} = 2 \cdot M_{\mathrm{mlf}}. \tag{3.45}$$

The total mass of the magnetic circuit parts of the two-sided LF-LSR-motor M_{lf2} is

$$M_{\mathrm{lf2}} = 2 \cdot M_{\mathrm{lf}} = 2 \cdot M_{\mathrm{mlf}} + 2 \cdot M_{\mathrm{slf}} + 2 \cdot M_{\mathrm{clf}} . \tag{3.46}$$

When a one-sided LF-LSR-motor design is expanded into a two-sided LF-LSR-motor design, the total mass is doubled and at the same time the traction force is also doubled. There is no point in designing only one-sided LF-LSR-motor, when the two-sided LF-LSR-motor gives the same traction force out of the same mass of the magnetic circuit parts and the normal forces are balanced.

3.3 Basic design of a TF-CLSR-motor

The mover pole has a circular geometry in cylindrical transversal flux SR-motors. The stator side is four-sided as it is in the four-sided TF-LSR-motor. However, the geometry of the stator pole faces is circular, but the stator pole pair can be also rectangular from its back iron. The same TF-LSR-motor designing principles are also valid for the TF-CLSR-motor. The four-sided TF-CLSR-motor has four stator pole pairs with two poles on each as in a four-sided TF-LSR-motor. A TF-CLSR-motor with a four-sided stator and in which the stator poles have circular geometry, is shown in figure 3.4.

The first difference in the design equations is how the inner radius r_{si} of the stator pole is determined. The inner radius of the stator pole must be selected in such a manner that there is enough winding space. The length of the pole arc l_{a} of the stator pole is determined by the pole face area and the pole width

$$l_{\mathrm{a}} = \frac{A}{t} . \tag{3.47}$$

The inner radius of the stator r_{sig} when the air gap is zero is found by solving the equation

$$A_{\mathrm{w}} = \frac{l_{\mathrm{wa}}}{2 \cdot \pi \cdot r_{\mathrm{sig}}} \cdot \left(\pi \cdot \left(r_{\mathrm{sig}} + d_{\mathrm{w}} \right)^2 - \pi \cdot r_{\mathrm{sig}}^2 \right) = l_{\mathrm{wa}} \cdot \left(\frac{t}{2} + \frac{t^2}{8 \cdot r_{\mathrm{sig}}} \right) . \tag{3.48}$$

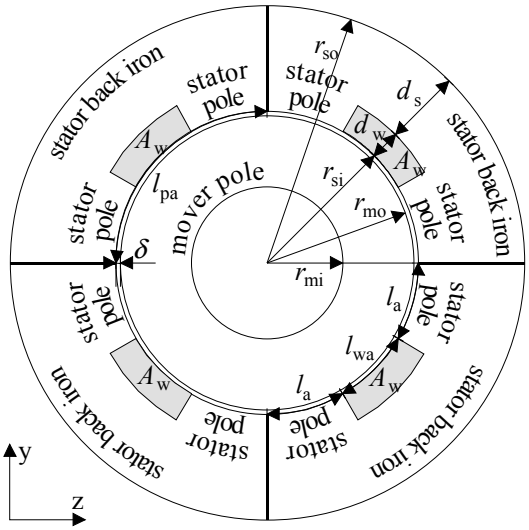

Figure 3.4. The schematic view of the TF-CLSR-motor showing a cross-section of the motor. A stator phase consists of four stator poles.

The total stator pole arc l_{pa} of the two poles and the winding window between the poles is

$$l_{pa} = 2 \cdot l_a + l_{wa} = \frac{\pi}{2} \cdot r_{sig}, \tag{3.49}$$

where l_a is the arc of the stator pole and l_{wa} is the arc of the winding window.

Equation (3.48) can be re-arranged into an equation of second order of r_{sig}, when l_{wa} is solved from equation (3.49) and substituted into equation (3.48)

$$\pi \cdot t \cdot {r_{sig}}^2 + \left(\frac{\pi}{4} \cdot t^2 - 4 \cdot A - 4 \cdot \frac{\Theta}{k_w \cdot J} \right) \cdot r_{sig} - A \cdot t = 0. \tag{3.50}$$

Equation (3.50) can be solved in a normal way. Hence, r_{sig} has two solutions. Only the positive solution is valid

$$r_{\mathrm{sig}} = \sqrt{\frac{t^2}{64} + \frac{1}{2\cdot\pi}\cdot\left(A - \frac{\Theta}{k_{\mathrm{w}}\cdot J}\right) + \frac{4}{\pi^2\cdot t^2}\left(A + \frac{\Theta}{k_{\mathrm{w}}\cdot J}\right)^2} - \frac{t}{8} - \frac{2}{\pi\cdot t}\cdot\left(A + \frac{\Theta}{k_{\mathrm{w}}\cdot J}\right). \quad (3.51)$$

The value of r_{sig} should be close to the rough value of the stator inner radius r_{si0}

$$r_{\mathrm{si0}} = \frac{2}{\pi}\cdot\left(l_{\mathrm{wa}} + 2\cdot l_{\mathrm{a}}\right) \approx \frac{4}{\pi\cdot t}\cdot\left(A + \frac{\Theta}{k_{\mathrm{w}}\cdot J}\right), \quad (3.52)$$

when l_{wa} is approximately

$$l_{\mathrm{wa}} \approx \frac{A_{\mathrm{w}}}{d_{\mathrm{w}}} = \frac{2\cdot\Theta}{k_{\mathrm{w}}\cdot J\cdot t}. \quad (3.53)$$

The inner radius r_{si} of the stator is then obtained by adding the air gap length δ to the r_{sig}

$$r_{\mathrm{si}} = r_{\mathrm{sig}} + \delta. \quad (3.54)$$

The outer radius r_{so} of the stator is determined so that there is enough space for the flux which passes through the stator poles

$$r_{\mathrm{so}} = r_{\mathrm{si}} + d_{\mathrm{w}} + l_{\mathrm{a}} = r_{\mathrm{si}} + \frac{t}{2} + \frac{A}{t}. \quad (3.55)$$

The outer radius r_{mo} of the mover is the stator inner radius minus the air gap length δ

$$r_{\mathrm{mo}} = r_{\mathrm{si}} - \delta = r_{\mathrm{sig}}. \quad (3.56)$$

The difference between the outer and the inner radius of the mover must be at least equal to the length of the pole arc. Hence, a dimensional constraint can be defined

$$r_{\mathrm{mo}} \geq l_{\mathrm{a}} \Leftrightarrow r_{\mathrm{si}} \geq l_{\mathrm{a}} + \delta. \quad (3.57)$$

This boundary condition is needed to ensure that there is enough space for the flux without a heavier saturation in the mover pole than in stator poles. The inner radius of the mover r_{mi} determines a piece of iron which can be cut out, if the outer radius of the mover exceeds the length of the pole arc

$$r_{\mathrm{mi}} = r_{\mathrm{mo}} - l_{\mathrm{a}} . \tag{3.58}$$

The volume of the mover pole V_{tmp} of the cylindrical transversal flux linear SR-motor is

$$V_{\mathrm{tmp}} = \pi \cdot t \cdot \left(r_{\mathrm{mo}}^2 - r_{\mathrm{mi}}^2 \right) = \pi \cdot A \cdot \left(2 \cdot \left(r_{\mathrm{si}} - \delta \right) - \frac{A}{t} \right), \tag{3.59}$$

and the mover pole iron mass M_{tmp} of the TF-CLSR-motor is

$$M_{\mathrm{tmp}} = V_{\mathrm{tm}} \cdot \rho_{\mathrm{Fe}} = \pi \cdot t \cdot \rho_{\mathrm{Fe}} \cdot \left(r_{\mathrm{mo}}^2 - r_{\mathrm{mi}}^2 \right) = \pi \cdot \rho_{\mathrm{Fe}} \cdot A \cdot \left(2 \cdot \left(r_{\mathrm{si}} - \delta \right) - \frac{A}{t} \right). \tag{3.60}$$

The total mass of the mover M_{tm} of the TF-CLSR-motor is

$$M_{\mathrm{tm}} = M_{\mathrm{tmp}} \cdot p_{\mathrm{m}} = \pi \cdot \rho_{\mathrm{Fe}} \cdot A \cdot p_{\mathrm{m}} \cdot \left(2 \cdot \left(r_{\mathrm{si}} - \delta \right) - \frac{A}{t} \right). \tag{3.61}$$

The volume of the cylindrical stator pole pair system (four-sided stator) V_{tsp} of the TF-CLSR-motor is

$$V_{\mathrm{tsp}} = t \cdot \left(\pi \cdot \left(r_{\mathrm{so}}^2 - r_{\mathrm{si}}^2 \right) - A_{\mathrm{w}} \right) = t \cdot \left(\pi \cdot \left(\frac{t}{2} + \frac{A}{t} \right) \cdot \left(2 \cdot r_{\mathrm{si}} + \frac{t}{2} + \frac{A}{t} \right) - \frac{\Theta}{k_{\mathrm{w}} \cdot J} \right), \tag{3.62}$$

and the stator pole iron mass M_{tsp} of the TF-CLSR-motor is

$$M_{\mathrm{tsp}} = V_{\mathrm{tsp}} \cdot \rho_{\mathrm{Fe}} = t \cdot \rho_{\mathrm{Fe}} \cdot \left(\pi \cdot \left(\frac{t}{2} + \frac{A}{t} \right) \cdot \left(2 \cdot r_{\mathrm{si}} + \frac{t}{2} + \frac{A}{t} \right) - \frac{\Theta}{k_{\mathrm{w}} \cdot J} \right). \tag{3.63}$$

The copper volume of the stator pole winding V_{tcp} is

$$V_{\mathrm{tcp}} = 2 \cdot \left(l_{\mathrm{a}} + 2 \cdot t \right) \cdot A_{\mathrm{Cu}} = 2 \cdot \frac{\Theta}{J} \cdot \left(\frac{A}{t} + 2 \cdot t \right) . \tag{3.64}$$

The copper mass of the stator pole winding M_{tcp} is

$$M_{\mathrm{tcp}} = V_{\mathrm{tcp}} \cdot \rho_{\mathrm{Cu}} = 2 \cdot \rho_{\mathrm{Cu}} \cdot \frac{\Theta}{J} \cdot \left(\frac{A}{t} + 2 \cdot t \right) . \tag{3.65}$$

The total mass M_{t4s} of the cylindrical transversal flux linear SR-motor having four-sided stator is

$$M_{\mathrm{t4s}} = \left(M_{\mathrm{tsp}} + M_{\mathrm{tcp}} \right) \cdot p_{\mathrm{s4s}} + M_{\mathrm{tm}} = \left(M_{\mathrm{tsp}} + M_{\mathrm{tcp}} \right) \cdot p_{\mathrm{s4s}} + M_{\mathrm{tmp}} \cdot p_{\mathrm{m}} . \tag{3.66}$$

3.4 Basic design of an LF-TLSR-motor

The design principles for the LF-TLSR-motor are mainly the same as those for the LF-LSR-motor. A three-phase LF-TLSR-motor is shown in figure 3.5. The tubular geometry of the poles of the LF-TLSR-motor causes some changes in the pole dimensions. The area of the mover back iron has to be approximately twice the required cross-sectional pole face area, because there may be simultaneous fluxes of different phases. The minimum radius r_{mtb} of the mover back iron is then

$$r_{\mathrm{mtb}} \geq \sqrt{\frac{2 \cdot A}{\pi}} . \tag{3.67}$$

The height of the mover pole h_{mlf} is determined by equation (3.37). The outer radius r_{mto} of the mover is

$$r_{\mathrm{mto}} = r_{\mathrm{mtb}} + h_{\mathrm{mlf}} = \sqrt{\frac{2 \cdot A}{\pi}} + \frac{2 \cdot t}{m - 1} . \tag{3.68}$$

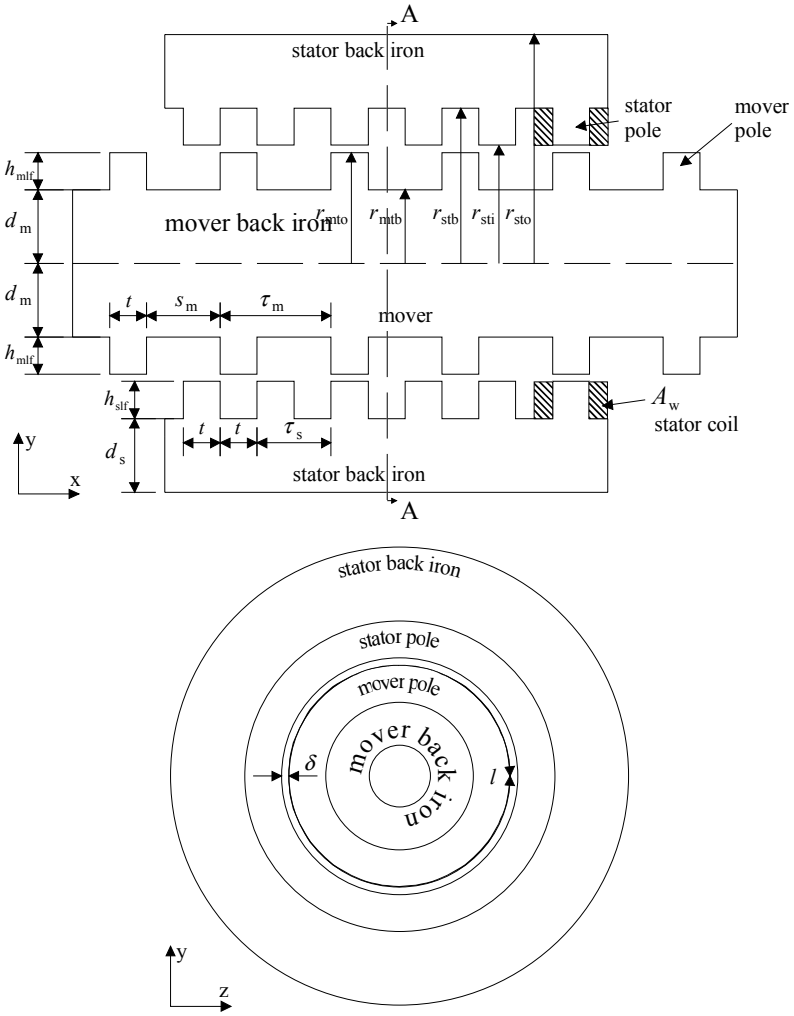

Figure 3.5. The schematic view of the three-phase LF-TLSR-motor. Upper picture shows the longitudinal-section of the motor and lower picture shows a cross-section of the motor. One pole winding is shown.

The length of the mover pole circle l is

$$l = 2 \cdot \pi \cdot r_{\mathrm{mto}} = 2 \cdot \pi \cdot \left(\sqrt{\frac{2 \cdot A}{\pi}} + \frac{2 \cdot t}{m-1} \right). \tag{3.69}$$

The pole width t is given by the cross-sectional area of the pole face divided by the length of the mover pole circle. The second order equation of the pole width t is obtained by substituting equation (3.69) into the pole width expression

$$t = \frac{A}{l} \Leftrightarrow \frac{2}{m-1} \cdot t^2 + \sqrt{\frac{2 \cdot A}{\pi}} \cdot t - \frac{A}{2 \cdot \pi} = 0 \,. \tag{3.70}$$

Equation (3.70) has two solutions. Only the positive solution for the pole width is valid. Hence, the maximum pole width is

$$t \le \sqrt{\frac{A}{8 \cdot \pi}} \cdot \left(\sqrt{m^2 - 1} \; - m + 1 \right). \tag{3.71}$$

The required space of the winding determines the height of the stator pole h_{slf} defined by equation (3.35). The outer radius of the stator r_{sto} is obtained by adding h_{slf} and the thickness of the stator back iron d_{s} to the inner radius of the stator, and the inner radius of the stator r_{sti} is obtained by adding the air gap length to the outer radius of the mover

$$r_{\mathrm{sti}} = r_{\mathrm{mto}} + \delta \,, \tag{3.72}$$

$$r_{\mathrm{sto}} = r_{\mathrm{sti}} + h_{\mathrm{slf}} + d_{\mathrm{s}} = \delta + 2 \cdot t + \frac{1}{t} \left(\frac{A}{2 \cdot \pi} + 2 \cdot \frac{\Theta}{k_{\mathrm{w}} \cdot J} \right). \tag{3.73}$$

The radius of the back iron of the stator r_{stb} is

$$r_{\mathrm{stb}} = r_{\mathrm{sti}} + h_{\mathrm{slf}} = \delta + \frac{1}{t} \left(\frac{A}{2 \cdot \pi} + 2 \cdot \frac{\Theta}{k_{\mathrm{w}} \cdot J} \right). \tag{3.74}$$

The mover volume V_{mtl} of the tubular geometry longitudinal flux linear SR-motor is then

$$V_{\mathrm{mtl}} = \pi \cdot p_{\mathrm{mlf}} \cdot \left(r_{\mathrm{mto}}^2 \cdot t + r_{\mathrm{mtb}}^2 \cdot s_{\mathrm{m}} \right), \tag{3.75}$$

and the mover mass M_{mtl} of the LF-TLSR-motor is

$$M_{\mathrm{mtl}} = V_{\mathrm{mtl}} \cdot \rho_{\mathrm{Fe}} = \pi \cdot \rho_{\mathrm{Fe}} \cdot p_{\mathrm{mlf}} \cdot \left(r_{\mathrm{mto}}^2 \cdot t + r_{\mathrm{mtb}}^2 \cdot s_{\mathrm{m}} \right). \tag{3.76}$$

The stator volume V_{stl} of the LF-TLSR-motor is

$$\begin{aligned} V_{\mathrm{stl}} &= \pi \cdot p_{\mathrm{slf}} \cdot \left(\left(r_{\mathrm{sto}}^2 - r_{\mathrm{sti}}^2 \right) \cdot t + \left(r_{\mathrm{sto}}^2 - r_{\mathrm{stb}}^2 \right) \cdot t \right) \\ &= 4 \cdot \pi \cdot m \cdot t \cdot \left(\left(\frac{\Theta}{k_{\mathrm{w}} \cdot J \cdot t} + 2 \cdot t \right) \cdot \left(\frac{A}{\pi \cdot t} + 2 \cdot (\delta + t) + \frac{\Theta}{k_{\mathrm{w}} \cdot J \cdot t} \right) + \frac{\Theta}{k_{\mathrm{w}} \cdot J} \right), \end{aligned} \tag{3.77}$$

and the stator mass M_{stl} of the LF-TLSR-motor is

$$\begin{aligned} M_{\mathrm{stl}} &= V_{\mathrm{stl}} \cdot \rho_{\mathrm{Fe}} \\ &= 4 \cdot \pi \cdot \rho_{\mathrm{Fe}} \cdot m \cdot t \cdot \left(\left(\frac{\Theta}{k_{\mathrm{w}} \cdot J \cdot t} + 2 \cdot t \right) \cdot \left(\frac{A}{\pi \cdot t} + 2 \cdot (\delta + t) + \frac{\Theta}{k_{\mathrm{w}} \cdot J \cdot t} \right) + \frac{\Theta}{k_{\mathrm{w}} \cdot J} \right). \end{aligned} \tag{3.78}$$

The total copper volume V_{ctl} of the LF-TLSR-motor is

$$\begin{aligned} V_{\mathrm{ctl}} &= 2 \cdot \pi \cdot \frac{1}{2} \cdot \left(r_{\mathrm{sti}} + r_{\mathrm{stb}} \right) \cdot A_{\mathrm{Cu}} \cdot p_{\mathrm{slf}} \\ &= 4 \cdot \pi \cdot m \cdot \frac{\Theta}{J} \cdot \left(\delta + \frac{A}{2 \cdot \pi \cdot t} + \frac{\Theta}{k_{\mathrm{w}} \cdot J \cdot t} \right), \end{aligned} \tag{3.79}$$

and the copper mass M_{ctl} of the LF-TLSR-motor is

$$\begin{aligned} M_{\mathrm{ctl}} &= V_{\mathrm{ctl}} \cdot \rho_{\mathrm{Cu}} \\ &= 4 \cdot \pi \cdot \rho_{\mathrm{Cu}} \cdot m \cdot \frac{\Theta}{J} \cdot \left(\delta + \frac{A}{2 \cdot \pi \cdot t} + \frac{\Theta}{k_{\mathrm{w}} \cdot J \cdot t} \right). \end{aligned} \tag{3.80}$$

The mass of the magnetic parts M_{tlf} of the tubular pole geometry longitudinal flux linear SR-motor is

$$M_{\mathrm{tlf}} = M_{\mathrm{stl}} + M_{\mathrm{ctl}} + M_{\mathrm{mtl}}. \tag{3.81}$$

3.5 Comparison of the basic structures of the linear SR-motors

Two important features of the linear SR-motors are the mass of the moving parts and the total mass of the motor. When the required traction force is applied, a comparison between the four basic structures can be postponed by calculating the dimensions of the motors based on different structures. This comparison is not valid generally. The designer should always start from an application point of view and check all the requirements carefylly. The conditions for this particular comparison are:

- The traction force data used (some of the data is presented in figure 3.6. with the material M2) is calculated by using the 2D-FEM-model of the basic transversal flux pole pair (chapter 5.2.1) and by using material M2 similar to normal construction steel (chapter 5.1.1).
- The traction force is generated by one phase magnetised in the edge position.
- The traction force is specified to be 1000 N, and three-, four- and five-phase motors were considered. The chosen traction force can be any traction force presented in the available data. The traction forces of the other structure sizes can be calculated by scaling the structure sizes for 1000 N. The relation between the differences in structural dimensions remains the same regardless of the traction force values.
- The stroke length is 1 m. The largest pole face area is 10000 mm^2 (t 100 mm, l 100 mm) in the data of the traction force values. The largest pole width is then 100 mm for the TF-LSR-motor. The minimum stroke length is 2*5*100=1000 mm for the five-phase TF-LSR-motor, when the stroke length is at least equal to the electrical length. The mass of movers of LSR-motors grows linearly with the number of mover poles. Again, the relation between the differences in sizes remains the same regardless of the stroke length.
- The free variable of the comparison is the cross-sectional pole face area. The magnetomotive force (total MMF) is determined by the data.
- The pole width is chosen optimally to obtain the minimum mover mass.

- The current density is 10 A/mm^2. Finally, the effect of current density on structure sizes is examined by using current density values which are multiples of 10 A/mm^2.

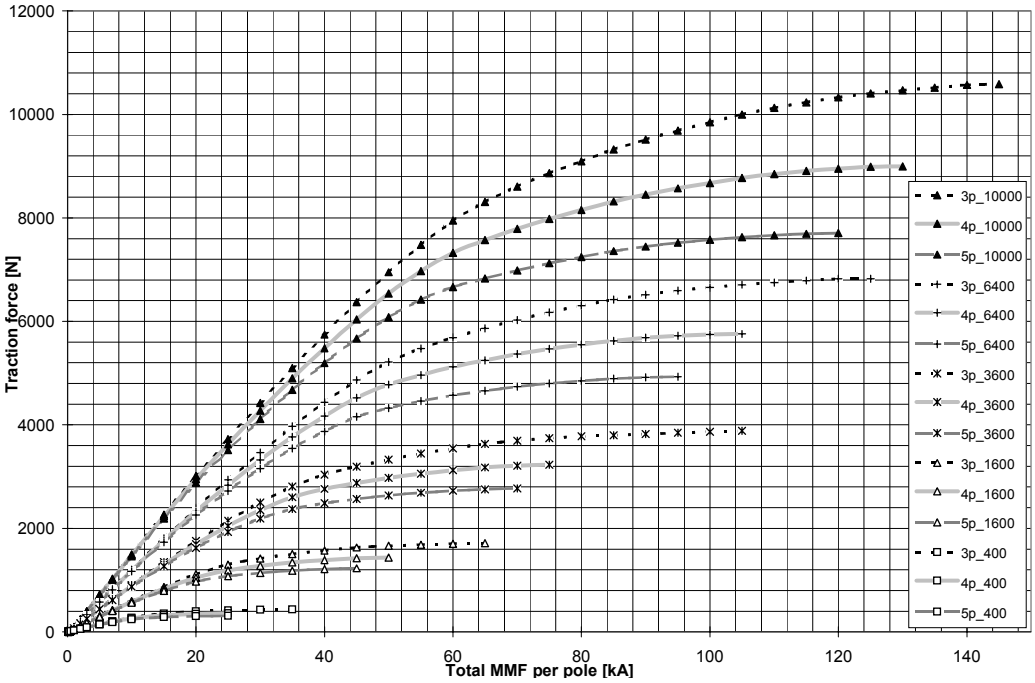

Figure 3.6. The traction force of the BTFPP-model as a function of the total MMF per pole and the cross-sectional pole face area when the magnetic material used is M2. The labels indicate three-phase as 3p, four-phase as 4p and five-phase as 5p. Numbers 400, 1600, 3600, 6400 and 10000 indicate the cross section area of the pole face in mm^2. The ratio t/l is unity.

Figures 3.7., 3.8., 3.9., 3.10. and 3.11. illustrate the mass of the movers and the total mass of the motors as functions of the pole cross-sectional areas and the phase numbers. A summary of the different parameters calculated when comparing the LSR-motors of different structures is shown in tables 3.2., 3.3., 3.4., and 3.5. pointing out the lightest and the heaviest mover of each structure and phase number.

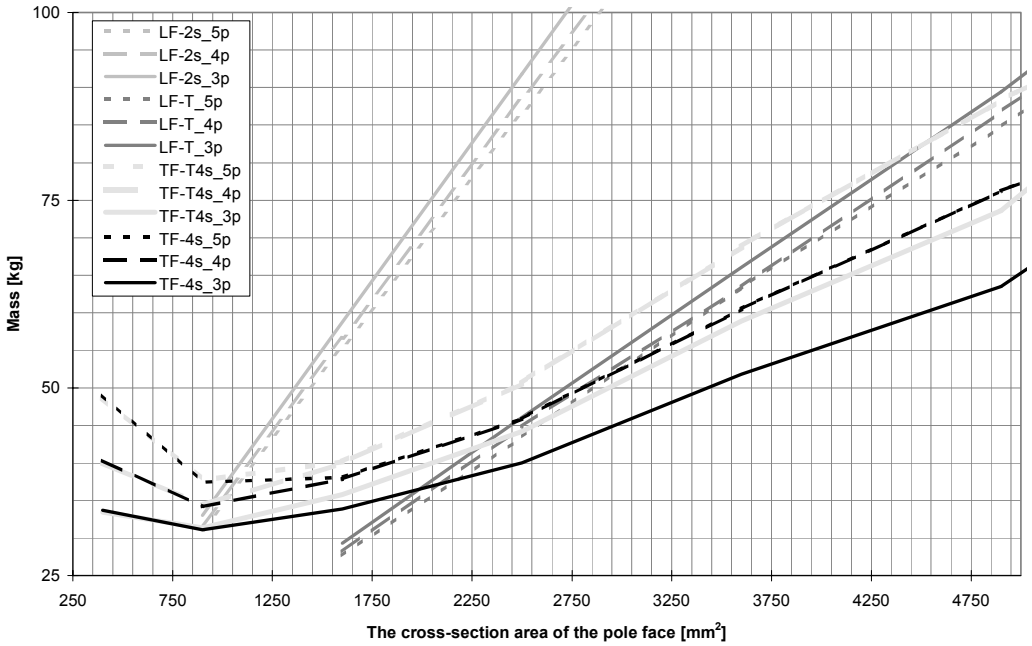

Figure 3.7. The mass of the movers of the LSR-motors as functions of the pole cross-section areas and phase numbers. Labels used: LF-2s_3p, LF-2s_4p, LF-2s_5p are two-sided longitudinal flux LSR-motors with phase numbers 3, 4 and 5 respectively. LF-T_3p, LF-T_4p, LF-T_5p are tubular longitudinal flux LSR-motors with phase numbers 3, 4 and 5 respectively. TF-T4s_3p, TF-T4s_4p, TF-T4s_5p are cylindrical transversal flux four-sided stator LSR-motors with phase numbers 3, 4 and 5 respectively. TF-4s_3p, TF-4s_4p, TF-4s_5p are four-sided transversal flux LSR-motors with phase numbers 3, 4 and 5 respectively.

The tubular LF-LSR-motors can have the lightest movers, but the total mass of the tubular LF-LSR-motor is considerably larger than that of the other structures (see figure 3.11.). The minimum mover mass of the TF-LSR, TF-CLSR and LF-LSR-motor seems to be quite even, but the mass of the mover in the LF-LSR-motor increases rapidly with the cross-sectional area of the pole.

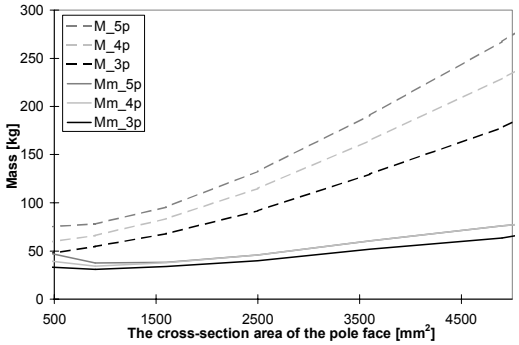

Figure 3.8. The total mass and the mover mass of the four-sided transversal flux LSR-motor as a function of the cross-section area of the pole face. Labels used: M_3p, M_4p, M_5p are the total masses of the four-sided TF-LSR-motors with phase numbers 3, 4 and 5 respectively. Mm_3p, Mm_4p, Mm_5p are the masses of movers of the four-sided TF-LSR-motors with phase numbers 3, 4 and 5 respectively.

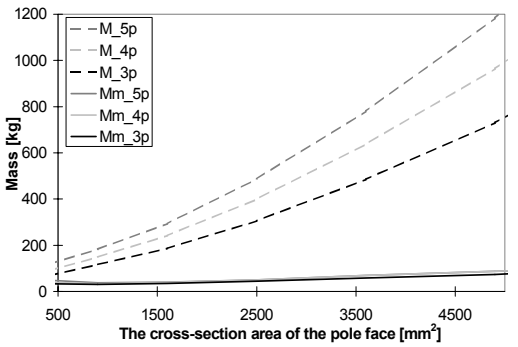

Figure 3.9. The total mass and the mover mass of the four-sided stator cylindrical transversal flux LSR-motor as a function of the cross-section area of the pole face. Labels used: M_3p, M_4p, M_5p are the total masses of the four-sided TF-TLSR-motors with phase numbers 3, 4 and 5 respectively. Mm_3p, Mm_4p, Mm_5p are the masses of movers of the four-sided TF-CLSR-motors with phase numbers 3, 4 and 5 respectively.

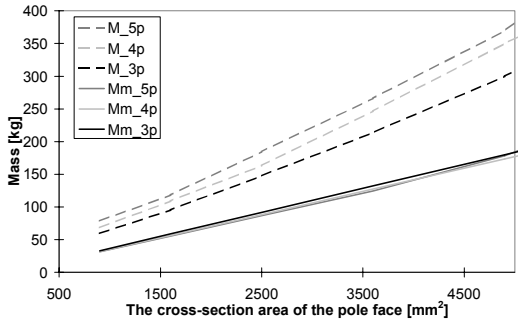

Figure 3.10. The total mass and the mover mass of the two-sided longitudinal flux LSR-motor as a function of the cross-section area of the pole face. Labels used: M_3p, M_4p, M_5p are the total masses of the two-sided LF-LSR-motors with phase numbers 3, 4 and 5 respectively. Mm_3p, Mm_4p, Mm_5p are the masses of movers of the two-sided LF-LSR-motors with phase numbers 3, 4 and 5 respectively.

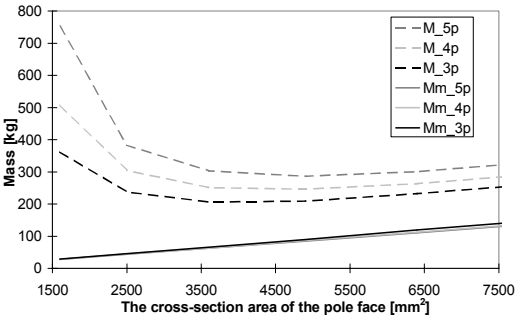

Figure 3.11. The total mass and the mover mass of the tubular longitudinal flux LSR-motor as a function of the cross-section area of the pole face. Labels used: M_3p, M_4p, M_5p are the total masses of the tubular LF-LSR-motors with phase numbers 3, 4 and 5 respectively. Mm_3p, Mm_4p, Mm_5p are the masses of movers of the tubular LF-LSR-motors with phase numbers 3, 4 and 5 respectively.

Table 3.2. Some calculation results of the four-sided transversal flux LSR-motor (TF-LSR) when the generated traction force of the one stator phase is 1000 N in overlap position, and the stroke length is 1m. The air gap is 0.2 mm. The material used in the calculation is similar to the normal construction steel. The current density is 10 A/mm^2. m is the phase number, A is the cross-section area of the pole face, Θ is the total MMF (Ampere turns) in the pole winding, t is the pole width, l is the pole length, L_e is the electrical length of the motor, p_s is the stator pole number, p_m is the mover pole number, l_p is the total length of the stator pole and the length of the side of the four-sided mover, M_{s4} is the total mass of the four-sided stator iron, M_{cu4} is the total mass of the copper of the four-sided stator, M_{mp4} is the mass of the four-sided mover pole, M_{m4s} is the total mass of the four-sided mover. M_{4s} is the total mass of the four-sided transversal flux LSR-motor.

m	3 the lightest mover	3 the heaviest mover	4 the lightest mover	4 the heaviest mover	5 the lightest mover	5 the heaviest mover
A [mm^2]	900	10000	900	10000	900	10000
Θ [A]	5529	2036	5651	2041	5802	2046
t [mm]	30	100	30	100	30	100
l [mm]	30	100	30	100	30	100
L_e [mm]	180	600	240	800	300	1000
p_s	12	12	16	16	20	20
p_m	12	4	13	4	14	4
l_p [mm]	121.4	206.8	122.8	206.8	124.5	206.8
M_{s4} [kg]	12.9	289.7	17.3	386.3	21.9	482.9
M_{cu4} [kg]	10.7	13.1	14.6	17.6	18.7	22.0
M_{mp4} [kg]	2.6	33.6	2.6	33.6	2.7	33.6
M_{m4s} [kg]	31.1	134.5	34.2	134.5	37.5	134.5
M_{4s} [kg]	54.7	437.3	66.1	538.4	78.1	639.4

Table 3.3. Some calculation results of the cylindrical four-sided stator transversal flux LSR-motor (TF-CLSR) when the generated traction force of the one stator phase is 1000 N in overlap position, and the stroke length is 1m. The air gap is 0.2 mm. The material used in the calculation is similar to the normal construction steel. The current density is 10 A/mm^2. m is phase number, A is the cross-section area of the pole face, Θ is the total MMF (Ampere turns) in the pole winding, t is the pole width, l_a is the length of the pole arc, L_e is the electrical length of the motor, p_s is the stator pole number, p_m is the mover pole number, r_{mi} is the inner radius of the mover pole, r_{mo} is the outer radius of the mover pole, r_{si} is the inner radius of the stator pole, r_{so} is the outer radius of the stator pole, M_{ts4} is the total mass of the cylindrical four-sided stator iron, M_{tc4} is the total mass of the copper of the four-sided cylindrical stator, M_{tmp} is the mass of the cylindrical mover pole, M_{tm} is the total mass of the cylindrical mover, M_{t4s} is the total mass of the cylindrical four-sided stator transversal flux LSR-motor.

m	3 the lightest mover	3 the heaviest mover	4 the lightest mover	4 the heaviest mover	5 the lightest mover	5 the heaviest mover
A [mm^2]	900	10000	900	10000	900	10000
Θ [A]	5529	2036	5651	2041	5802	2046
t [mm]	30	100	30	100	30	100
l_a [mm]	30	100	30	100	30	100
L_e [mm]	180	600	240	800	300	1000
p_s	12	12	16	16	20	20
p_m	12	4	13	4	14	4
r_{si} [mm]	73.9	131.2	74.7	131.2	75.7	131.2
r_{so} [mm]	118.9	281.2	119.7	281.2	120.7	281.2
r_{mi} [mm]	43.7	31.0	44.5	31.0	45.5	31.0
r_{mo} [mm]	73.7	131.0	74.5	131.0	75.5	131.0
M_{ts4} [kg]	74.6	1831.7	100.3	2442.4	126.6	3053.1
M_{tc4} [kg]	10.7	13.1	14.6	17.6	18.7	22.0
M_{tmp} [kg]	2.6	40.0	2.7	40.0	2.7	40.0
M_{tm} [kg]	31.4	160.1	34.4	160.1	37.7	160.2
M_{t4s} [kg]	116.7	2005.0	149.3	2620.1	116.8	3235.2

Table 3.4. Some calculation results of the two-sided longitudinal flux LSR-motor (LF-LSR) when the generated traction force of the one stator phase is 1000 N in overlap position, and the stroke length is 1m. The air gap is 0.2 mm. The material used in the calculation is similar to the normal construction steel. The current density is 10 A/mm^2. m is phase number, A is the cross-section area of the pole face, Θ is the total MMF (Ampere turns) in the pole winding, t is the pole width, l is the pole length, L_e is the electrical length of the motor, p_{slf} is the stator pole number, p_{mlf} is the mover pole number, M_{sl2} is the total mass of the two-sided stator iron, M_{cl2} is the total mass of the copper of the two-sided stator, M_{ml2} is the mass of the two-sided mover, M_{lf2} is the total mass of the two-sided longitudinal flux LSR-motor.

m	3 the lightest mover	3 the heaviest mover	4 the lightest mover	4 the heaviest mover	5 the lightest mover	5 the heaviest mover
A [mm^2]	900	10000	900	10000	900	10000
Θ [A]	55825	1815	6180	1822	6696	1831
t [mm]	27.8	83.3	26.8	75	25	75
l [mm]	32.4	120	33.6	133.3	36	133.3
L_{elf} [mm]	333.3	1000	428.6	1200	500	1500
p_{slf}	12	12	16	16	20	20
p_{mlf}	24	8	28	12	32	16
M_{sl2} [kg]	15.4	321.7	20.9	386.3	26.8	485.0
M_{cl2} [kg]	11.0	11.2	15.5	14.8	20.6	18.6
M_{ml2} [kg]	33.1	367.3	31.9	425.0	31.2	519.4
M_{lf2} [kg]	59.5	700.1	68.2	827.7	78.6	1023.0

Table 3.5. Some calculation results of the tubular longitudinal flux LSR-motor (LF-TLSR), when the generated traction force of the one stator phase is 1000 N in overlap position, and the stroke length is 1m. The air gap is 0.2 mm. The material used in the calculation is similar to the normal construction steel. The current density is 10 A/mm^2. m is phase number, A is the cross-section area of the pole face, Θ is the total MMF (Ampere turns) in the pole winding, t is the pole width, l is the length of the mover pole circle, L_{elf} is the electrical length of the motor, p_{slf} is the stator pole number, p_{mlf} is the mover pole number, r_{mtb} is the radius of the mover back iron, r_{mto} is the outer radius of the tubular mover pole, r_{sti} is the inner radius of the tubular stator pole, r_{sto} is the outer radius of the tubular stator pole, r_{stb} is the radius of the stator back iron, M_{tsl} is the total mass of the tubular stator iron, M_{ctl} is the total mass of the copper of the tubular stator, M_{mtl} is the total mass of the tubular mover, M_{tlf} is the total mass of the tubular longitudinal flux LSR-motor.

m	3 the lightest mover	3 the heaviest mover	4 the lightest mover	4 the heaviest mover	5 the lightest mover	5 the heaviest mover
A [mm^2]	1600	10000	1600	10000	1600	10000
Θ [A]	8853	3420	9479	3445	10680	3473
t [mm]	6.6	16.5	7.0	17.41	7.2	17.9
l [mm]	242.1	100	229.7	574.3	223.1	557.7
L_{elf} [mm]	79.3	198.3	111.4	278.6	143.5	358.6
p_{slf}	6	6	8	8	10	10
p_{mlf}	51	21	54	22	56	23
r_{sti} [mm]	38.7	96.5	36.8	91.6	35.7	89.0
r_{sto} [mm]	498.4	198.5	504.3	192.4	546.4	189.4
r_{stb} [mm]	485.2	165.5	490.4	157.5	532.0	153.5
r_{mtb} [mm]	31.9	79.8	31.9	79.8	31.9	79.8
r_{mto} [mm]	38.5	96.3	36.6	91.4	35.5	88.8
M_{stl} [kg]	254.8	103.3	367.6	140.5	554.6	178.4
M_{ctl} [kg]	78.3	15.1	112.5	19.3	170.7	23.7
M_{mtl} [kg]	29.4	188.8	28.2	179.6	27.7	177.7
M_{tlf} [kg]	362.5	307.3	508.3	339.5	752.9	379.9

The base current density is 10 A/mm^2 because the comparison values are calculated by using that current density. The effect of the current density on the structure sizes of the LSR-motors can be examined by using equations (3.18), (3.21), (3.23), (3.41), (3.42), (3.43), (3.60), (3.63), (3.65), (3.76), (3.78) and (3.80), which determine the mover, the stator and the copper mass. All variables are set to be unity and the current densities have p.u. values 0.5, 1 (10 A/mm^2), 1.5, 2 and 2.5. Now the change rate of the mover mass, the stator mass, and the copper mass as a function of the change rate of the current density can be found. All masses are calculated by using unity values and the current density multipliers.

Figure 3.12. illustrates the change rate of the mover mass of the different LSR-motor structures. The mover mass of the LF-LSR-motors does not depend on the current density, thus the change rate of the mover mass of the LF-motors is unity.

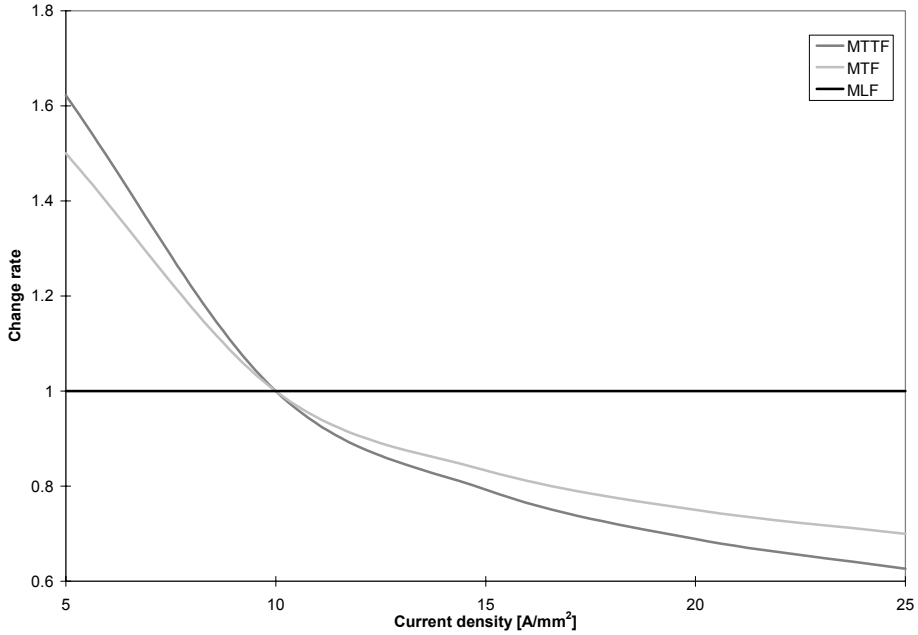

Figure 3.12. The change rate of the mover mass as a function of the current density. The labels indicate MTTF as the mass of the mover of the TF-CLSR-motor, MTF as the mass of the mover of the TF-LSR-motor and MLF as the mass of the mover of the LF-LSR-motor and the LF-TLSR-motor.

Figure 3.13. illustrates the change rate of the stator mass of the different LSR-motor structures.

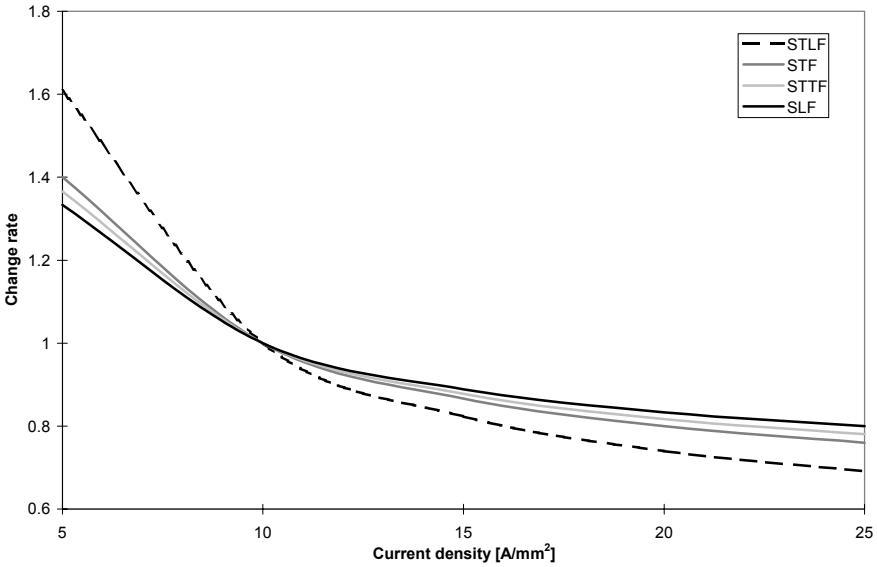

Figure 3.13. The change rate of the stator mass as a function of the current density. The labels indicate STLF as the mass of the stator of the LF-TLSR-motor, STF as the mass of the stator of the TF-LSR-motor, STTF as the mass of the stator of the TF-CLSR-motor and SLF as the LF-LSR-motor.

The current density determines the area needed for the winding. The change rate of the mass of the copper is then the same for all structures. Equations (3.23), (3.43), (3.65) and (3.80) obtain the same result illustrated in figure 3.14.

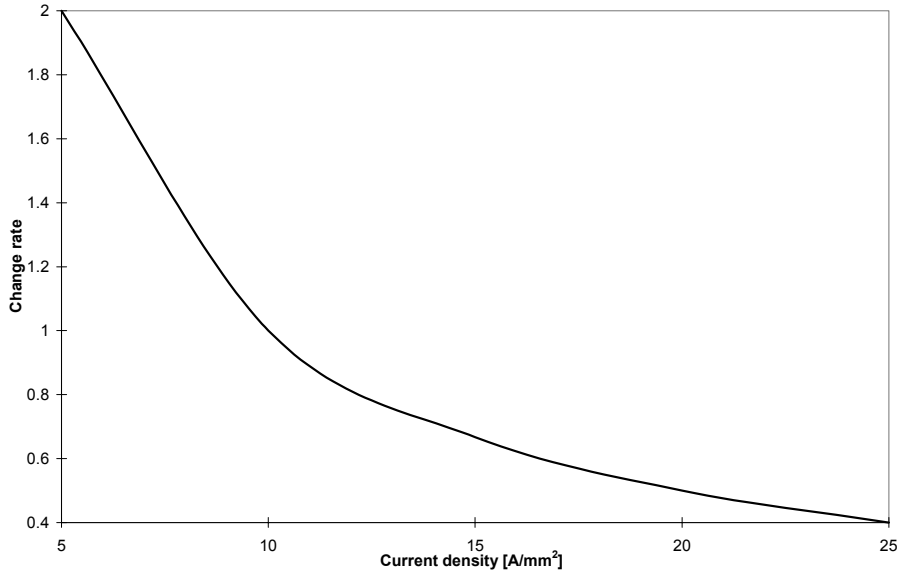

Figure 3.14. The change rate of the copper mass of the windings as a function of the current density.

3.5.1 Conclusions from the comparison between different LSR-motor structures

As figure 3.8. illustrates, the LF-TLSR-motor provides the lightest mover of the examined structures. However, this design of the LF-TLSR-motor is less practical because of the high total mass of the motor and the high total MMF required. The outer diameter of the stator is about 12.5 times the outer diameter of the mover, which makes the construction less practical. If the outer diameter of the tubular stator is about 2…5 times the outer diameter of the mover, then the stray flux is quite small and the design is magnetically good. However, this kind of design may leave as a result to heavy mover.

The permissable current density depends on the cooling system used. If natural air cooling or a light blower is used, then the current density have to be under five A/mm^2 and the LF-LSR-motor seems to have some advantage over TF-designed motors. TF-designs seem to have even lighter movers than LF-designs, when the current density is high.

The stray flux of the TF-LSR design might be remarkable, if the coil is wound on the stator back iron. The stray flux can be reduced, if the coils are wound on the pole legs. Some constructional freedom is lost especially with four-sided stator TF-LSR designs if the coils are wound on the stator pole legs.

Transversal flux designs seem to be more promising than the longitudinal flux designs, when high performance is required. The tubular or cylindrical construction is quite complicated. The tubular design cannot be integrated as a closed shape in any kind of a shuttle or as a part of some tool but it is attractive in terms of the limited stroke designs.

As a conclusion, the four-sided transversal flux LSR-motor (TF-LSR) with poles of rectangular geometry is chosen for a closer study. Furthermore the basic transversal flux pole pair system can provide a model for all LSR-motors.

4 MODELLING

In order to calculate the state of the motor there has to be a model. The model has to describe the process in which energy is converted from electricity into mechanical energy in order to obtain accurate results both for the static and the dynamic state of the motor. The magnetic circuit of a linear movement transversal flux switched reluctance motor is in a state of continuously changing saturation. Saturation causes a strong non-linear behaviour of the magnetic circuit. There are no general laws describing different kinds of SR-machines which could be applied simply by changing the parameters (Salo, 1996). Modelling is usually carried out first by using numerical methods and then by verifying the calculated results by constructing a prototype and measuring all the available data.

Because of the continuously variable magnetic circuit and because of the saturating materials in a transversal flux LSR-motors, the modelling of the motor must be carried out using numerical methods. In this dissertation the static properties are calculated by means of 2D- and 3D-FEM-analysis. The calculation results are validated by the measurements of a prototype. Static properties characterise the traction force potential of the LSR-motor. The basic dimensional design is based on static properties. This may be compared to the process in which the dimensions of the induction machine are chosen.

The static properties of the linear SR-motor are described by the flux linkage $\psi=f(i,x)$ and by the traction force $F_t=f(i,x)$ (Lawrenson, 1980. p. 261), where i is the phase current and x is the position of the mover. The linear SR-motor produces a traction force when the pole pair which has an increasing inductance in the direction of movement is excited. Force is produced by the natural tendency to minimise the field energy in the SR-motor, not by induction as it is in the case in sinusoidal rotating field machines. The modelling of SR-machines in this work is divided into the following steps:

1. Static properties,
    - force of one-pole pair as a function of the current and position,
    - flux linkage of one-pole pair as a function of the current and position.

2. Dynamic properties,

   - current and flux linkage of the motor as a function of time,
   - force of the motor as a function of current and position.

After the basic dimensions have been selected the performance of the LSR-motor may be predicted. The static traction force production and the static flux linkage as a function of current are the starting point of the modelling of the dynamic properties. The static properties represent ideal conditions in which the maximum dynamic performance can be achieved. Electric, magnetic and friction losses decrease the performance.

4.1 Solving the magnetic field problem by means of the finite element method

Maxwell's equations provide a means to solve magnetic field problems. The solution for any magnetic field problem is not likely to be found in an analytically exact closed form for practical devices. Numerical methods are required in order to solve field problems.

FEM-calculation (FEM, Finite Element Method) is the most popular method of all numerical methods used to solve electro-magnetic field problems. During the past decades, the FEM-calculation has been strongly developed especially in the 80's. Scientists have developed excellent algorithms, which are now available in numerous software packages. In addition, the computing power of a desktop PC has increased, and therefore quite large electro-magnetic problems can now be solved by using commercially available FEM-packages and low-price PC-computers. In the following an overview in the litterature concerning the use of FEM in analysing SR-motors will be given.

Adamiak & al (1987) studied a high normal force problem of a single-sided SR-linear motor by means of 2D-static-FEM. Edwards, Preston and Williams (1987) calculated geometrical coefficients of equations which give the normal force and traction force of a short-secondary linear reluctance motor. These coefficients were obtained by 2D-FEM-calculations.

In his paper "Review of recent progress in linear motors" McLean (1988) demonstrated the possibilities of FEM-calculations in analysing linear motors. According to McLean the 3D-FEM-

analysis might be in the future a superior technique for linear motor analysis when computing power has increased enough.

Leu, Scorza and Bartel (1988) used 2D-FEM to validate an analytical model of a variable air gap linear force motor (a permanent magnet type motor). They calculated flux densities and forces by comparing the results of the analytic model with those of the FEM-calculations. This speeded up the modelling work.

Akmese and Eastham (1989) studied the cogging force behaviour of a brushless-DC tubular linear motor by means of 2D-FEM. This machine is a permanent magnet linear motor and it has the same kind of cogging force as the cogging torque in rotary PM-machine. The cogging torque is caused by permeance variation and permanent magnets. The cogging behaviour is to be solved with FEM-calculation.

Abrahamsen, Ennemark and Jensen (1994) used FEM-calculation to find the flux linkage and the force characteristics of a linear reluctance actuator. The flux linkage was the core of their magnetic model of the solenoid valve.

Khan and Ivanov (1994) used 2D-axi-symmetric-FEM-calculation to design and analyse a four-phase cylindrical variable reluctance linear step motor for the control rod drive in nuclear reactors. They discovered that FEM-calculation gives more accurate values for forces than the approximating analytic technique when dealing with iron saturation, especially with large stator currents.

Rizzo and Savini (1995) studied whether there could be a law describing the down scaling of a linear reluctance motor. The investigation was done by studying the ratio of force and mass as a function of the mover position per unit. Several different scale factors were used. The scale factors were calculated using 2D-FEM-calculation. The results provided useful information on the optimal dimension of the motor for a specific use.

Imal and Williams (1994) illustrated the complexity of the 2D-modelling of a 3D-linear motor. They had to create a fictious 2D-model which illustrated a motor with a hollow can secondary

and a solid structure primary. The traction forces obtained by FEM-calculations differ -21 ... 10% from the measured ones and normal forces from -13.9 ... 7.5%.

Moghani & al (1994) studied a linear brushless PM-DC-motor using both the 2D- and 3D-FEM-analysis. According to their results the 3D-analysis is approximately 20% more accurate compared to the results of a 2D-analysis.

Moghani, Eastham, Akmese and Hill-Cottingham (1994) analysed the effect of slot skewing in order to reduce the cogging force of a single-sided permanent magnet brushless linear motor. They found out that it is impossible to analyse the slot skewing by means of a 2D-FEM. They modelled the same motor also using the 3D-technique. The 3D-FEM gave results that were close to the measured force values. They were also able to calculate the lateral forces caused by the slot skewing by 3D-FEM.

Michaelides and Pollock (1994) investigated an 8/6-SR-motor and showed in their paper that the magnetic end effects cause a significant error in 2D-FEM force calculations. Using the 3D-FEM they got force calculation results that were 8% more accurate than those obtained with 2D-FEM. The Maxwell stress tensor method was applied to both the 2D- and 3D-analysis.

Wakiwaka, Yajima, Senoh and Yamada (1996) validated the thrust limit equation of the linear DC-PM-motor by using 3D-FEM. The values obtained from the equation and the 3D-FEM-results were close to each other and the maximum error of 3D-FEM-calculated thrust constant was 26% to the measured thrust constant values.

York, Stephenson and Hughes (1997) calculated the static force characteristics of a linear variable-reluctance actuator by means of 3D-static-FEM-calculation. The results were used to validate the measured data and to describe the hysteretic friction loop in static force measurements.

Rizzo, Savini and Turowski (1997) compared the transversal tubular variable reluctance actuator and the longitudinal tubular variable reluctance actuator of the same size by using 2D-FEM and 3D-FEM. They found that the 3D-FEM-calculation gives exact results while the 2D-FEM results were not accurate.

Benhama, Williamson and Reece (1997) studied the effect of the flux in the core ends with the 2D- and 3D-FEM-analysis. The 3D-FEM-analysis gave approximately 20% more accurate force calculation results than the 2D-FEM-analysis when compared to the measured forces. The motor was a 3-phase 6/4-SR-motor and the stack length was about only 0.5 times the rotor diameter.

Rizzo, Savini and Turowski (1997) calculated the force and inductance characteristics of both the transversal and longitudinal structure tubular variable reluctance actuators. They analysed both motors by means of the 2D- and a 3D-FEM. The 3D-FEM was found to give quite exact force calculation results when compared to the measured results. The 2D-FEM force calculation results were about 15% smaller than the measured results of the transversal construction linear motor. The 2D-FEM force calculation results for the longitudinal structure linear motor were completely wrong. The same kind of results were obtained also in inductance calculations.

Basak, Filho, Nakata and Takahashi (1997) analysed the force production of a novel brushless-PM-DC linear motor. They showed that the use of a 3D-FEM to simulate the flux distribution and the static force production of this type of linear motor is necessary, efficient and accurate.

FEM-models are made of continuous shapes by discretisation into finite element meshes. The accuracy of FEM-calculation greatly depends on the mesh. In other words, the finer the mesh, the better the result will be. However, due to the rounding errors in computers when summing a large amount of small numbers, extremely fine meshes are useless. The quality of the mesh also depends on the regularity of the mesh elements. Small elements neighbouring close to cause discontinuities in the flux density. When solving field problems experience is needed in setting finite element meshes in order to get accurate results.

The magnetic circuit of an electric motor can be designed with the help of FEM-calculation, and the performance of the motor can then be predicted. The MagNet 5.2 Windows NT version package from Infolytica Co is used in this work. The FEM-modelling, solving and post-processing can be done with the MagNet™ in two dimensional (2D) as well as in three dimensional (3D) space. The MagNet 5.2 software is lacking the magnetic hysteresis modelling with magnetic materials. Moving of magnetic bodies is not allowed, thus simulation of the real running motor is not possible.

4.1.1 Calculation of the force by the means of FEM-analysis.

There are a few methods to evaluate forces in FEM-calculations. The Maxwell stress tensor method, the classical virtual work method and the Coulomb virtual work method are introduced here.

The traction force may be calculated from the flux linkage applying the classical virtual work principle e.g. the change in magnetic energy or the magnetic coenergy in relation to the change in position. The more elegant choice is to get the force directly from a single solved field problem. It gives a more accurate result than the calculation of force from field energies obtained from at least two separately solved field problems. The suitable methods for the force calculation of the SR-motor with FEM-calculation are the Maxwell stress tensor method and the Coulomb virtual work method.

The classical virtual work method is based on the energy balance. The example in figure 4.1. which is a very usual (ψ,i)-figure for SR-motors, shows that the energy balance of the motor with a constant current can be expressed by

$$i\psi = W_{\mathrm{f}} + W_{\mathrm{co}} \tag{4.1}$$

where W_{f} is the magnetic field energy and W_{co} is the magnetic coenergy.

When equation (4.1) is differentiated with respect to the distance x while the current is constant we get

$$i\frac{\partial \psi}{\partial x} = \frac{\partial W_{\mathrm{f}}}{\partial x} + \frac{\partial W_{\mathrm{co}}}{\partial x}. \tag{4.2}$$

The traction force is then

$$F_{\mathrm{t}} = i\frac{\partial \psi}{\partial x} - \frac{\partial W_{\mathrm{f}}}{\partial x} = \frac{\partial W_{\mathrm{co}}}{\partial x}. \tag{4.3}$$

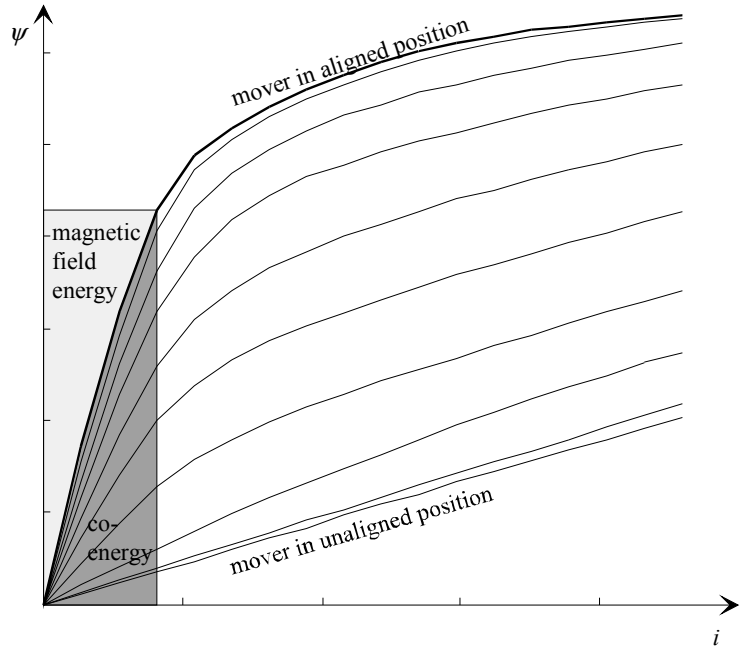

Figure 4.1. Magnetisation curves of a practical SR-machine. i is the current and ψ is the flux linkage. Each curve represent some mover or rotor position.

Global field energy and global coenergy obtained by FEM-calculation are not sensitive to local field density errors caused by the finite discretisation of a continuous shape. However, at least two field solutions are needed for two different meshes when the mover has been displaced by an arbitrary distance. It may look as if the most accurate value for the force is calculated when the movement is as small as possible. This causes a numerical problem when the difference of almost similar values has to be taken. The increase of the moving distance in order to get larger differences in global coenergy decreases the accuracy of the change in the global coenergy as a function of the mover position. This is also a discretisation problem, when the continuous movement is modelled by finite discrete steps (McFee, 1987. p. 3771).

Maxwell stress tensors for force calculations have been used especially in 2D-field problems. The method can be applied when the magnetic body is surrounded by air (vacuo). The total force can be found by integrating the Maxwell field stresses in a vacuo over this surface. The

surface force components can then be divided into the normal force component F_{n} and the tangential force component F_{t} (Carpenter, 1959. p. 21)

$$\begin{aligned} F_{\mathrm{n}} &= \tfrac{1}{2}\mu_0\left(H_{\mathrm{n}}^2 - H_{\mathrm{t}}^2\right), \\ F_{\mathrm{t}} &= \mu_0 H_{\mathrm{n}} H_{\mathrm{t}} \end{aligned} \tag{4.4}$$

where μ_0 is the permeability of the vacuo, H_{n} and H_{t} are the normal and the tangential components of the magnetic field strength in vacuo (air). When the relation $B = \mu H$ is substituted into equation (4.4) we get the following surface integration equation in vector notation (Benhama, 1997. p. 60) for the surface force $\boldsymbol{F}$

$$\boldsymbol{F} = \tfrac{1}{2\mu_0}\oint_s\left(B_{\mathrm{n}}^2 - B_{\mathrm{t}}^2\right) ds\cdot\boldsymbol{t} + \tfrac{1}{\mu_0}\oint_s B_{\mathrm{n}} B_{\mathrm{t}}\, ds\cdot\boldsymbol{n}\,, \tag{4.5}$$

where B_{n} and B_{t} are the normal and the tangential components of the magnetic flux density of the surface s surrounding the magnetic body. $\boldsymbol{n}$ and $\boldsymbol{t}$ are unit vectors in the normal and tangential directions of the surface s.

Only one solution for the magnetic field is needed to obtain the global force acting on the magnetic body when the Maxwell stress tensor is applied. The closed surface s must be entirely in the air. It must not pass through any material. The accuracy of the force computation is involved in the type of elements crossed by the integration path and placement of this path inside the elements. In 2D-problems the surface integration is reduced to a line integral around a closed path and is quite easy to implement, but the surface integral needed in 3D-problems when Maxwell stress tensors are used is quite cumbersome.

The Coulomb virtual work method is based on the application of the virtual work principle. The force is obtained as the derivatives of the magnetic energy or coenergy versus the displacement of the moving magnetic body. The force computation algorithm in the finite element field computation can be divided into three parts (Coulomb, 1984. p. 1894) :

1. Computation of the nodal values of the potentials.

2. Determination of the derivatives of the co-ordinates of the nodes versus the virtual displacement of the movable magnetic body.

3. Computation of the force by integration over virtually distorted finite elements.

The global force F_q acting on a magnetic body surrounded by air in direction q is

$$F_q = \frac{\partial W_{\text{co}}}{\partial q}. \tag{4.6}$$

The scalar vector potential is kept constant during the virtual translation. An alternative choice is to use the magnetic field energy and magnetic vector potential instead of the scalar potential and coenergy. The flux density is kept constant when the magnetic vector potential is used. The global force in direction q can be expressed as (Benhama, 1997. p. 60)

$$F_q = -\tfrac{1}{2\mu_0} \sum_{\text{e}} \left\{ \Omega_{\text{e}} \frac{\partial B^2}{\partial q} + B^2 \frac{\partial \Omega_{\text{e}}}{\partial q} \right\}, \tag{4.7}$$

where Ω_{e} is the finite element volume and B is the flux density in the element. The summation is performed over all the finite elements (e) in the layer of air surrounding the part on which the force is to be calculated. The general direction q can refer to (Benhama, 1999. p. 26):

$$q = \begin{cases} x \text{ or } y & \text{for 2D linear translations} \\ \theta_{\text{z}} & \text{for 2D rotation around the z - axis} \\ x, y \text{ or } z & \text{for 3D linear translations} \\ \theta_{\text{x}}, \theta_{\text{y}}, \theta_{\text{z}} & \text{for 3D rotation} \\ z & \text{for axisymmetric linear translations} \end{cases}$$

The finite element mesh of the device has to be divided into three regions: the movable region, the fixed region and the intermediate region (Coulomb, 1984. p. 1895) (Benhama, 1997. p. 60). The virtual displacement is done by the movable region which causes that the intermediate region is distorted.

As far the Maxwell stress tensor method, the Coulomb virtual work method needs only one field solution. The Coulomb virtual work method employs a volume integral to determine the global force in 3D-field problems. The volume integral is easier to implement in 3D-field problems than the surface integral needed in the Maxwell stress tensor method. The Coulomb virtual work method removes the dependency of the computed force towards position of the integration path within the element (Benhama, 1997. p. 60). The accuracy of both methods, the Maxwell stress tensor method and the Coulomb virtual work method, is sensitive to the mesh discretisation, because the force is computed by using only a small amount of finite elements i.e. the elements in the air which surround the movable magnetic body of the whole device (McFee, 1987. p. 3773).

According to Coulomb and Meunier (1984), McFee and Lowther (1987) with Benhama, Williamson and Reece (1997) and (1999), the Maxwell stress tensor method and the Coulomb virtual work method can be much more accurate than the multiple solution classical virtual work principle. Furthermore, the Coulomb virtual work method may be superior in terms of accuracy and implementation when compared to the Maxwell stress tensor method when the force of a 3D-magnetostatic field problem is to be solved (Benhama, 1997. p. 63), (Benhama, 1999. p. 31). The accuracy of both methods seems to be quite even in 2D-magnetostatics problems (McFee, 1987. p. 3773), (Gieras, 1997. p. 3593-3594). In the MagNet™ software package for the calculation of force the Coulomb virtual work method is used to solve 3D-problems and the Maxwell stress tensor method is used for 2D-problems.

4.1.2 Calculation of the flux linkage by means of FEM-analysis.

The flux linkage is a kind of measure of the electrical properties of an SR-motor. Figure 4.1. illustrates a typical fux linkage ψ and current i relationships of an SR-motor when the rotor position or the mover position is a parameter. The static magnetisation curves in figure 4.1. may be obtained from measurements or they may be calculated from the magnetic field energy or the magnetic coenergy. Magnetic energies can be obtained from the magnetic field solution. The magnetic field coenergy W_{co} is obtained as an integral over volume S.

$$W_{co} = \int_S \left(\int_0^H B\, dH \right) d\, S\,. \tag{4.8}$$

The magnetic field energy W_{lin} in a case of linear magnetic material is

$$W_{\text{lin}} = \frac{1}{2}\int_S B\,H\,d\,S\,. \tag{4.9}$$

When a scalar potential is used the magnetic field energy W_{f} can be obtained in a non-linear case by

$$W_{\text{f}} = 2\,W_{\text{lin}} - W_{\text{co}}\,. \tag{4.10}$$

The corresponding regions describing different energies are further illustrated in figure 4.2.

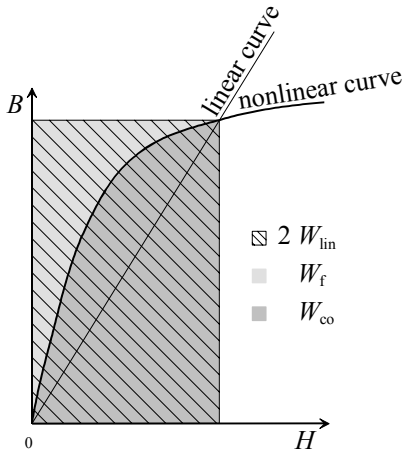

Figure 4.2. A (*B,H*)-curve and regions describing different energies. The area inside the quadrangle is two times linear energy and a sum of field energy and co-energy. Nonlinear curve spit the quadrangle into field energy (area above nonlinear curve) and co-energy (area under nonlinear curve).

The static magnetic field energy and magnetic coenergy are obtained directly from a log file after each MagNet™ FEM-solver run. The static flux linkage is then calculated by summing the field energy and coenergy and dividing it by the current used in each calculation when the mover position is kept constant. The method is clarified in figure 4.3. (Salo, 1996b. p. 5-5). The flux linkage as a function of the current and position can be obtained from

$$\psi(i,x) = \left(W_{\mathrm{f}}(i,x) + W_{\mathrm{co}}(i,x)\right)/i\ . \tag{4.11}$$

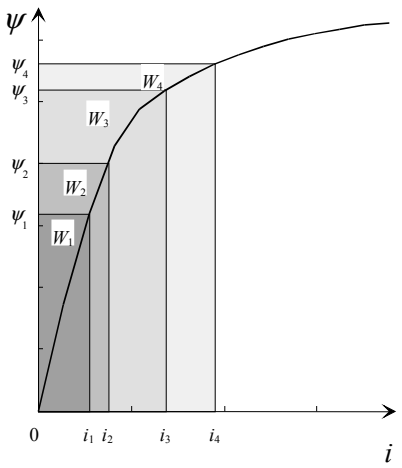

Figure 4.3. The calculation of the flux linkage by dividing the sum of field energy and co-energy in each (x,i)-point by current i. The curve represents magnetisation curve of some mover position x.

The flux linkages in figure 4.3. can be obtained by

$$\begin{aligned}
\psi_1(i_1) &= W_1/i_1 \quad & W_1 &= W_{\mathrm{f}}(i_1) + W_{\mathrm{co}}(i_1) \\
\psi_2(i_2) &= W_2/i_2 \quad & W_2 &= W_{\mathrm{f}}(i_2) + W_{\mathrm{co}}(i_2) \\
\psi_3(i_3) &= W_3/i_3 \quad & W_3 &= W_{\mathrm{f}}(i_3) + W_{\mathrm{co}}(i_3) \\
\psi_4(i_4) &= W_4/i_4 \quad & W_4 &= W_{\mathrm{f}}(i_4) + W_{\mathrm{co}}(i_4)
\end{aligned}\ . \tag{4.12}$$

The solving of static FEM-problems provides static energies as calculation results. Various kinds of losses in the windings and in the iron core change the static flux linkage so it occurs to be somewhat useless for the accurate dynamical analysis of an LSR-motor. The static flux linkages can be used as the basis for the designing of windings.

4.2 Dynamical modelling

A few possibilities for the dynamic modelling of the SR-motors are briefly consider here. Simultion models for the dynamic simulation with iron losses neglected and with iron losses included are porposed. One of the demanding goals of the LSR-motor research has been to achive

a complete dynamical simulation model of the iron circuit. Research is still in progress and it will take some years to obtain more accurate results.

The electrical circuit of a pole pair may be described by an equivalent circuit when iron losses are neglected. This is illustrated in figure 4.4.

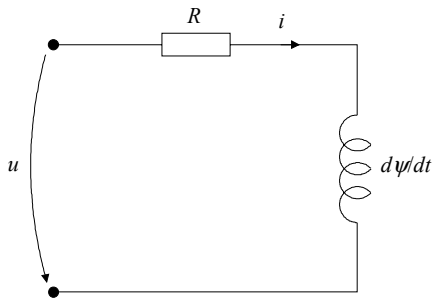

Figure 4.4. The equivalent circuit of a pole pair of an SR-linear motor. R is the resistance of the pole winding, i is the current in the pole winding and u is the supply voltage connected to the winding by power switches.

When iron losses are not considered, the voltage equation of the main circuit can be written as

$$\frac{d\psi}{dt} = u(t) - R\,i(t)\,, \tag{4.13}$$

The voltage u is a function of time only, $u=f(t)$. It has an intial value that is approximately equal to $\pm U_\mathrm{d}$ when switching occurs. U_d is a DC-link voltage of the supplying inverter (see figure 2.1.).

Equation (4.13) was adopted by Stephenson and Corda (1979) to describe the electro-magnetic circuit of the SR-motor. The strength of the model is its first order nature, which has no partial differential coefficients as the other forms of equation (4.13) have (Stephenson and Corda, 1979. p. 393).

The non-linear magnetic characteristics of the iron circuit are described by the flux linkage as a function of the mover position and current $\psi=f(i,x)$. This function is generally not known. Flux

linkage values can be obtained by measurements or by e.g. FEM-calculation. As a result, flux linkage is usually known in form of a table $\psi(i,x)$. The use of equation (4.13) requires the $\psi(i,x)$ table to be inverted into the table $i(\psi,x)$.

The most common method to interpolate the flux linkage as a function of the current and position is to use spline functions. Pulle (1991) used cubic spline technique to model the non-linear $\psi(i,x)$ characteristics of an SR-motor. The spline coefficients form a data base of the flux linkage base function $\Psi(i,x)$. The same technique was used to model the current base function $I(\psi,x)$ and the torque base function $T(i,x)$. Corda, Masic and Stephenson (1993) used also look-up tables $i(\psi,x)$ and $T(i,x)$ in their SR-drive simulation. The $i(\psi,x)$ and the $T(i,x)$ tables were generated numerically from the $\psi(i,x)$ table, which was modelled by using cubic spline interpolation. Abrahamsen, Ennemark and Jensen (1994) used also a table of $i(\psi,x)$ in their simulink model of a coil. Their simulation model for a linear reluctance actuator is based again on equation (4.13). They added a parallel resistor to the coil to model iron losses.

Most papers dealing with the controlling of SR-motors lack general equations. Control algorithms have to be based on tables of flux linkages, current and torque (force). Sjöberg and Alaküla (1996) used in simulations a 2D-look-up table for the current $i(\psi,x)$ and torque $T(i,x)$. Their actual control system used an EPROM-memory and microcontroller to interpolate the intermediate values of current and torque from the stored values. The control strategy was a hysteresis current control and pre-determined current reference values in order to minimise copper losses. Barrass and Mecrow (1996) used also current and torque tables in addition to a table for flux linkage, because their control strategy was to control the flux linkage. Their control system used a DSP-controller where the flux linkage reference values were modelled as piecewise linear functions. They still had to use a table for the flux linkage.

The real control system implementations need the tables of magnetisation data to be stored in the controller memory, but during the modelling phase there are a couple of alternative methods available. The fundamental idea of inductance is not valid because of the high non-linearity in the magnetic circuit and the presence of hysteresis and eddy currents. There are papers where inductance is used successfully for special cases.

Li and Jufer (1994) used equation (4.13) in a form where flux linkage is a product of the inductance and current. Their SR-motor was a high speed device with a solid iron rotor. They also added a short circuit winding to represent iron losses in the rotor side. They modelled the inductance of the stator side to be the sum of the constant inductance and a cosine term depending on the rotor rotation angle with respect to the stator. There is a mutual inductance between the stator winding and a fictious rotor short circuit winding. All inductances and iron loss resistances were found experimentally. The measured values and the simulated values were quite close to each other. The simulation with an iron loss equivalent circuit in the rotor side gave better results than without iron loss prediction.

Liu and Kuo (1994) used an inductance to represent the magnetic behaviour of their linear reluctance motor. They modelled the inductance as a Fourier series first order approximation. This enables the modelling of the machine secondary periodic salient poles. This model is a linear one neglecting iron loss and saturation. This of course causes differences between the measured results and the simulated values. The simulated traction forces have more or less sinusoidal shapes, whereas the measured values are flat topped versions of those simulated sinusoidal shapes.

Corda and Wilkinson (1995) used the inductance as a function of the mover position to represent the magnetic characteristics of their cylindrical linear switched reluctance actuator. They modelled the inductance of a linear SR-motor to be the sum of the constant term and four sinusoidal terms. The coefficients of the terms were determinated by using the data of only three mover positions: the aligned position, the unaligned position and the edge position. This method was meant for rapid performance evaluation and the calculated static traction force results were not quite so accurate when compared to the measured static traction force.

The optimisation of a control strategy in order to minimise copper losses is a task where magnetisation data has to be modelled in some functional form. Tolsa, Silventoinen, Salo and Pyrhönen (1996) used a sum of exponentials to represent the magnetisation data of their experimental SR-motor. The set of coefficients were found experimentally from static torque measurements (Salo, 1996a). This method allowed them to represent the magnetic behaviour of their experimental SR-motor quite accurately. A table of reference current values which give mini-

mum copper losses was found in an optimisation process. This table was then programmed into a microcontroller memory.

Cincotti, Marchesi and Serri (1997) used a neural network instead of tables to represent the inductance as a function of the current and position in their variable reluctance linear actuator. This neural network was used to find out the right value of inductance as well as to estimate the position of the mover. The neural network was trained by using a 2D-table of inductance. In fact, the normal interpolation of a 2D-table is just as accurate as the use of a neural network. The authors claimed that the programming and the use of a M86HC11E9 microcontroller is more effective when the neural network is used instead of normal look-up table.

In addition to equation (4.13) a few more equations are needed in the simulation of the dynamical state of the LSR-motor. The coenergy W_{co} is found from the integral of the flux linkage

$$W_{co}(i,x) = \int_0^i \psi(i,x)\,di\,. \tag{4.14}$$

The traction force F_t is then obtained by differentiating the coenergy with respect to the distance of movement

$$F_t(i,x) = \frac{d\,W_{co}(i,x)}{d\,x}\,. \tag{4.15}$$

The equation of the motion is needed for the force balance

$$M\frac{d^2x}{dt^2} = F_t(i,x) - F_L\,, \tag{4.16}$$

where M is the total mass of the moving parts, F_L is a load force consisting of all kinds of mechanical forces, for example friction force.

4.2.1 A simulation model based on tables with neglected iron losses

Functions $\psi(i,x)$ and $i(\psi,x)$ are not known in an analytical form but tables representing them can be generated for example from FEM-calculation results. Because of tables the simulation model may be formed to be a lumped parameter model, which may be programmed to a simulation pakages like MATLAB™. The traction force of a pole pair can be calculated from equation (4.15), but the accuracy is better when the table of the force is generated directly from the FEM-analysis by using single solution methods described in chapter 4.1.1. This way calculation of the derivates is avoided. When the tables of the current and force are generated the simulation model of figure 4.5. can be created.

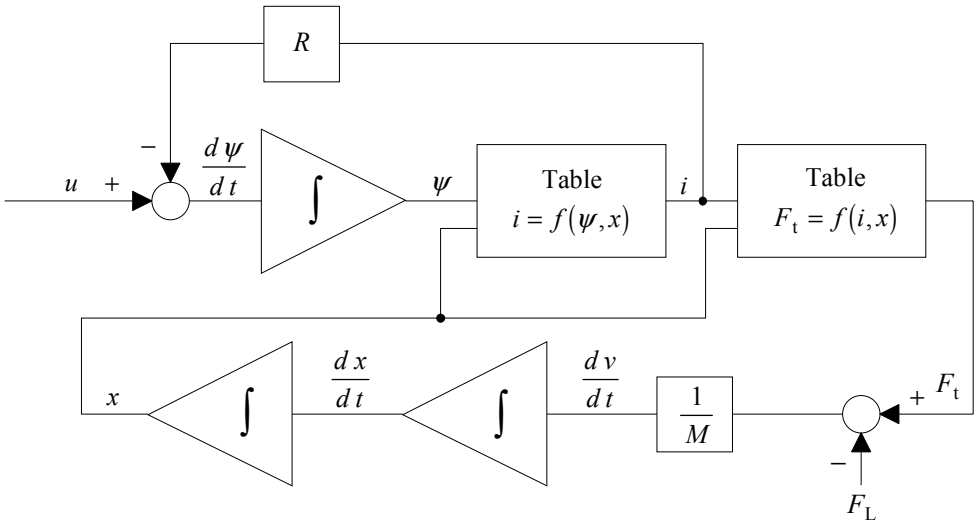

Figure 4.5. A simulation model of one phase of an LSR-motor based on tables of current and force. The model is valid for machines with neglible iron losses.

The simulation model in figure 4.5. is based on tables of the current and force. *R* is the resistance of one phase. *M* is the mass of all moving parts. Iron losses are not included in this simulation model. If all phases are controlled separately the whole motor simulation requires a simulation model as in figure 4.5. for each phase. The integration of the velocity and the position of the mover is common for all phases.

4.2.2 Iron losses

It is extremely difficult to predict the iron losses of electric machines, because the operation of an iron circuit and the iron circuit geometry might be complex. The scientist studying iron loss phenomena is normally concentrating on material physics and the results of the work are usually best suited for single electrical steel sheets and structures made of thin electrical steel sheets laminations. However, precise iron loss studies of complete electric machines are rarely reported. The most difficult task seems to be the evaluation of the iron losses of solid iron structures.

Iron losses are power losses that are generated inside the iron core. Iron losses are due to variations of the flux density because of the alternating flux itself and the flux density change in iron when iron moves in a magnetic field. Iron losses might be large depending on the rate of flux density changes. The knowledge can be obtained by computational methods or by measuring the losses from an actual electric machine.

The excitation and the flux of the TF-LSR-motor are unidirectional. During excitation multiple-pole pairs do not share the same magnetic circuit parts as one-pole pair. The magnetic circuit is always consisting of one or two mover poles and one or more stator poles of the same phase per time. There is no mutual coupling between the phases. This makes it possible to study iron losses by an excited pole pair basis. The iron losses of a periodic operation of a multiphase motor can be obtained simply by summing up the losses of individual active pole pairs.

It is widely accepted that the total iron power losses P_{Fe} can be expressed as a sum of the hysteresis power loss P_{hys} and the dynamic power loss P_{dyn} (Bertotti, 1988. p. 621), (Fiorillo, 1990. p. 2904)

$$P_{\mathrm{Fe}} = P_{\mathrm{hys}} + P_{\mathrm{dyn}} . \tag{4.17}$$

The dynamic iron loss can be divided into classical eddy current power loss P_{cla} and excess power loss P_{exe}

$$P_{\mathrm{dyn}} = P_{\mathrm{cla}} + P_{\mathrm{exe}} . \tag{4.18}$$

The classical eddy current loss is the only dynamic iron loss component when there are no moving parts of the magnetic core in a magnetic field, when the magnetic material is a perfectly homogenous material, when the magnetic domains are absent and when the flux waveform is sinusoidal. Eddy currents are generated by Faraday's induction law, when the flux penetrating a conducting material is changing. It is also known that every real magnetic material has a magnetic domain structure, which has an important role in the magnetisation process of the magnetic material. It has been found that the dynamic iron loss cannot be explained only by the classical eddy current power loss, when P_{dyn} is found larger than P_{cla} even in sinusoidal excitation conditions (Bertotti, 1988. p. 621). Additional power losses are generated, when the walls of magnetic domains are moving and there is a new balance of local magnetic fields (caused by local eddy currents) and external magnetic fields. These losses are explained by the excess power losses. The iron loss separation (Bertotti, 1985. p. 2110), (Fiorillo, 1990. p. 2904) can be then written as

$$P_{\mathrm{Fe}} = P_{\mathrm{hys}} + P_{\mathrm{cla}} + P_{\mathrm{exe}} . \tag{4.19}$$

Iron losses have been found to be proportional to the time derivative of the flux density (Fiorillo, 1990. p. 2904)

$$P_{\mathrm{hys}} \propto \frac{dB}{dt}, \quad P_{\mathrm{cla}} \propto \left(\frac{dB}{dt}\right)^2, \quad P_{\mathrm{exe}} \propto \left|\frac{dB}{dt}\right|^{\frac{3}{2}} . \tag{4.20}$$

The same iron loss components can also be found when a conductive part is moving in a magnetic field. The mover of a TF-LSR-motor is moving in the main field of a magnetised pole pair. The iron loss components of the changing main flux and velocity effects may be found by doing different kinds of measurements with the mover standstill and running. The prediction of iron loss separation can be found by transient FEM-calculations.

4.2.3 A simulation model based on tables with included iron losses

A simulation model based on tables with included iron losses is illustrated in figure 4.6. Functions of the parameters of the model are found numerically from the iron loss data. The most accurate simulation results may be obtained when iron losses are included into model. The supply voltage of the phase is u. The current of the phase winding is i. The DC-resistance of the phase winding is R. The stray flux inductance of the coil is L_σ. The current of the iron losses of velocity effects is i_v. R_v represents the power losses of eddy currents caused by velocity effects. The fictious iron loss flux caused by the velocity effects is ψ_v. The current of eddy current iron losses is i_d. R_d represents the power losses of eddy currents caused by alternating main flux. The fictious eddy current flux caused by the alternating main flux is ψ_d. The hysteresis current component of the hysteresis iron losses is i_h. The magnetising current of the main flux is i_M. The main flux transferring electric power to mechanical work is ψ_M. The mass of all moving parts is M. The parameters of the simulation model illustrated in figure 4.6. are obtained by measurements and FEM-calculations. The ideal traction force production can be obtained by static-FEM-calculation and by static traction force measurements. All dynamical effects decrease force production. This fact is employed in the simulation model in figure 4.6. in which the current producing traction force is reduced by the current components of the dynamic effects.

The velocity effects are taken into account by the current component i_v which is a function of ψ_v, and of the velocity and position. R_v provides damping and it can be also a function of the velocity and position. The power losses of the eddy currents caused by velocity effects P_v are obtained by the classical power loss equation

$$P_v = i_v^2 \cdot R_v \,. \tag{4.21}$$

The eddy current effects caused by the alternating main flux are taken into account by the current component i_d which is a function of ψ_d, main flux rate and position. R_d provides damping and it can be also a function of the position and the rate of the change of the main flux. The power losses of the eddy currents caused by the alternating main fluxP_d are

$$P_\mathrm{d} = i_\mathrm{d}^2 \cdot R_\mathrm{d} \,. \tag{4.22}$$

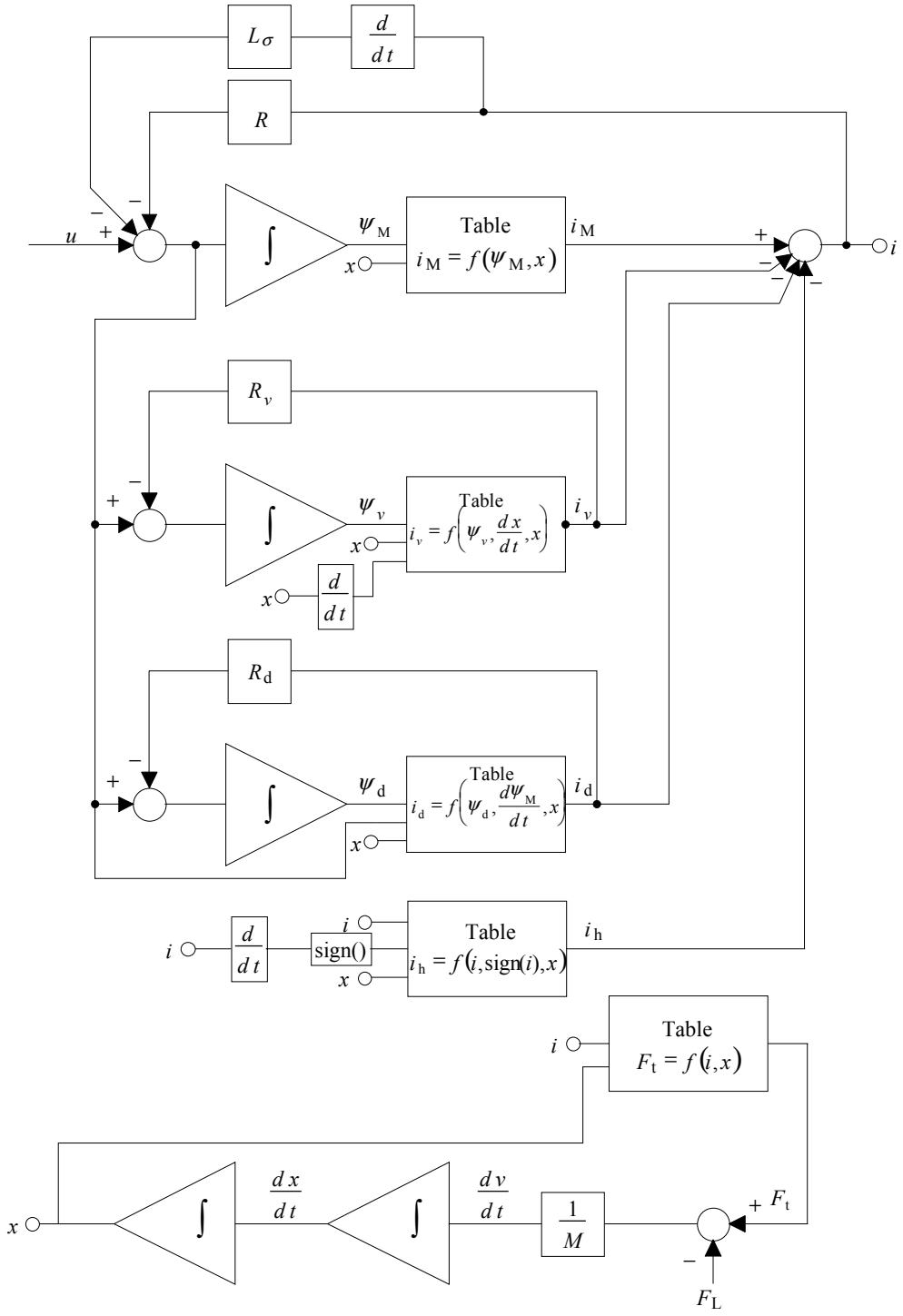

Figure 4.6. A simulation model of one phase of an LSR-motor based on tables of the current and force including iron losses caused by alternating main flux and velocity effects.

The hysteresis current component is measured in the static traction force measurement. The traction force is smaller than the mean traction force when the current is increasing and the traction force is larger than the mean traction force, when the current is decreasing. The mean traction force and the upward and downward lines of the traction force are shown in figure 4.7.

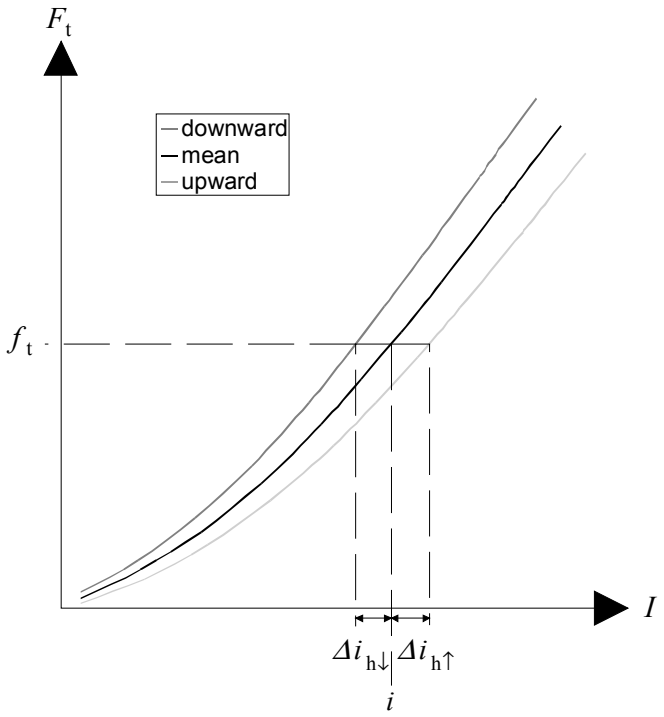

Figure 4.7. The mean traction force and the upward and downward curves of the traction force. The upward curve means the traction forces obtained by increasing current (0 → maximum current). The downward curve means the traction forces obtained by decreasing current (maximum current → 0).

The mean traction force has the value f_t when current is i and the mover is in position x. In case of hysteresis $\Delta i_{h\uparrow}$ is the amount of the current needed to add to the current of the mean traction force in order to transfer it from the mean curve to the upward curve. $\Delta i_{h\downarrow}$ is the amount of the current needed to subtract from the current of the mean traction force in order to transfer it from the mean curve to the downward curve. The hysteresis current component i_h in the simulation model is $\Delta i_{h\uparrow}$ with an increasing current and $\Delta i_{h\downarrow}$ with a decreasing current. i_h is also a func-

tion of the position. The power losses of the hysteresis currents caused by the alternating main flux P_{h} are naturally

$$P_{\mathrm{h}} = i_{\mathrm{h}}^2 \cdot R_{\mathrm{h}} \,. \tag{4.23}$$

4.3 Conclusions from the modelling

FEM-calculation has proved to be a quite useful tool for the studying of magnetic structures, which are to be modelled numerically. The static and transient FEM-analysis can provide force calculation and energy calculation results which may be used as data bases for the simulation models of the LSR-motors.

Simple voltage equation (4.13) is the basis for the simulation models, though there exist many methods to model the magnetic characteristics. All kinds of losses decreases the ideal performance. The losses must include to simulation model in order to get accurate simulation results. It depends on the actual machine structure how strong the effect of losses are on the motor performance.

All the research papers listed in chapter 4.2 have in common, that equation (4.13) is used to determine the flux linkage and then the current from the modelled magnetisation data. The torque or the force is normally calculated from the change of coenergy in respect of the change of position. Iron losses are usually neglected in the modelling, when laminated structures and relatively low speeds are used. None of the methods for the modelling of dynamical non-linear magnetic behaviour seem to be better than the others. Tables of values and interpolation between values are found to be the most popular method, when the dynamical state of the SR-machine is to be simulated.

5 FEM-CALCULATIONS AND THE MEASUREMENTS OF THE LABORATORY PROTOTYPE

FEM-calculation is a very suitable tool for design. However some simplifications and idealisations must be done when using FEM-analysis. It is still a good research practice to make laboratory prototypes in order to make sure that the calculation results approach as good as possible the real values and to enable error estimations. Developed FEM-models are introduced in this chapter. Calculation and measurement results are compared also.

The static properties of an LSR-motor; traction force and flux linkage can be calculated by FEM-analysis. It is enough to model the magnetic circuit parts of the basic pole pair system of the TF-LSR-motor. This is done by 2D- and by 3D-FEM-modelling. Other 2D- and 3D-FEM-models are also considered and comparative results are illustrated. The key result of the FEM-calculation is the generated traction force of the pole pair as a function of the cross-sectional area of the pole face and the total MMF of the pole. The magnetic material used, the phase number and the air gap length have their own influence on the generated force. However, the most important problem is the modelling of the solid magnetic material used in FEM-calculations.

5.1 Modelling of the magnetic materials used in FEM-calculations

When non-linear magnetic field problems are to be solved, the non-linear magnetic material must be modelled somehow. In the MagNet™ software FEM-package used the magnetic material modelling is done by using the relative magnetic reluctivity of the material ν_r (Edwards, 1995). The relative magnetic reluctivity is taken as a function of the square of flux density

$$\nu_r = f\left(B^2\right). \tag{5.1}$$

Reluctivity values are stored at forty evenly spaced intervals in B. At intermediate positions data is obtained within the program by interpolation. The stored values are derived by least-squares curve fitting to the (B,H)-input data. The maximum number of the allowed points in the input data is 48. The input information is obtained from electrical steel manufacture's data which is

provided in catalogues describing different electrical steel products. This data is available only for electrical steel sheets meant to be used in laminated magnetic cores. Alternatively the magnetisation data may be measured if suitable and accurate devices are available.

Solid cores are made of some steel or iron. The magnetisation data of normal constructional steels are normally not available. Some measured data may be found in literature, but the data can give only an estimate of the magnetisation properties of the particular piece of material. Constructional steels are meant to be used in machine construction and not for magnetic cores, thus magnetic properties are not guaranteed to be the same all the time. In order to obtain right and accurate results from the FEM-calculations the magnetic properties of steel or iron must be measured if it is going to be used as a solid magnetic core.

The (*B,H*)-curves of the magnetic materials used in FEM-calculation in this study are illustrated in figure 5.1.

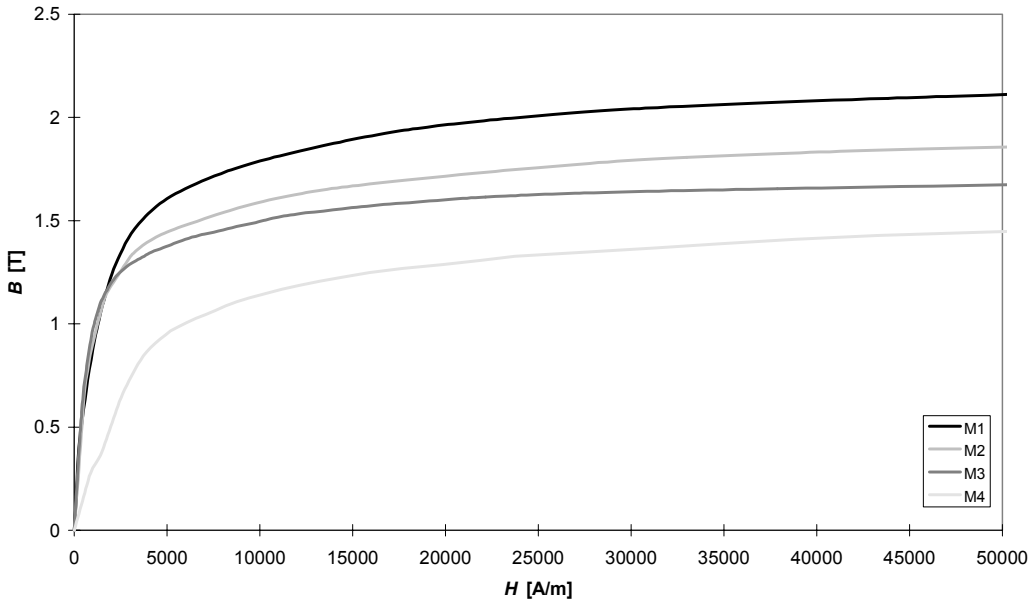

Figure 5.1. The (*B,H*)-curves of the magnetic materials M1, M2, M3 and M4 used in FEM-calculations in this study.

Material M1 was used in the laboratory prototype of the five-phase pole pair of the TF-LSR-motor and the magnetic data was measured on a rod (diameter 10 mm, height 10mm) of solid steel. Direct current was used in the measurement and the data used is the mean curve of the hysteresis loop of the measured material. The material is constructional steel and it has some additives such as C, Si, Mn, P, S, Cr, Ni, Mo, V, or Co. Material M2 is a constructional steel commonly used in all kinds of steel structures. Data was measured from a ring by using direct current (Pyrhönen, 1991. p. 69). Material M2 has more additives than material M1. The magnetic data of materials M3 and M4 are found from MagNet™ material library. They have even more additives to make them harder than materials M1 and M2.

5.2 2D-FEM-models

2D-FEM-models are quite quick to generate and quick to solve. 2D-FEM-models are an attractive choice for pre-design, because many ideas can be rapidly analysed. 2D-FEM-calculation is valid only when the main flux is about the same in every cross-sectional cut of the magnetic circuit (in depth) and the magnetic circuit can be infinitely long (in depth). This condition is met in general in rotating electrical motors made of electrical steel laminations.

5.2.1 2D-FEM-model of the basic transversal flux pole pair (BTFPP) of the TF-LSR-motor

Figure 2.7. shows clearly that the main flux goes in every direction of space. The flux creating the force in the air gap goes mainly in a 2D-plane perpendicular to the pole length, thus it is possible to generate a 2D-FEM-model of the basic transversal flux pole pair of TF-LSR-motor (BTFPP) illustrated in figure 5.2.

Different regions have their own labels in figure 5.2. Label B indicates the stator poles. The height of region B corresponds to stator pole length in a TF-LSR-motor. Label C indicates an active mover pole generating the traction force. The height of region C corresponds to the mover pole length and two times the mover pole height in a TF-LSR-motor. The passive mover pole required in the basic pole pair of the TF-LSR-motor is made of regions D, D1, D2, D3 and D4 depending on phase number. Regions D, D3 and D4 make the passive mover pole for a

three-phase motor. Regions D, D2 and D3 make the passive mover pole for a four-phase motor. Regions D, D1 and D2 make the passive mover pole for a five-phase motor. Region E is needed for magnetisation and regions S and T indicate the coil sides.

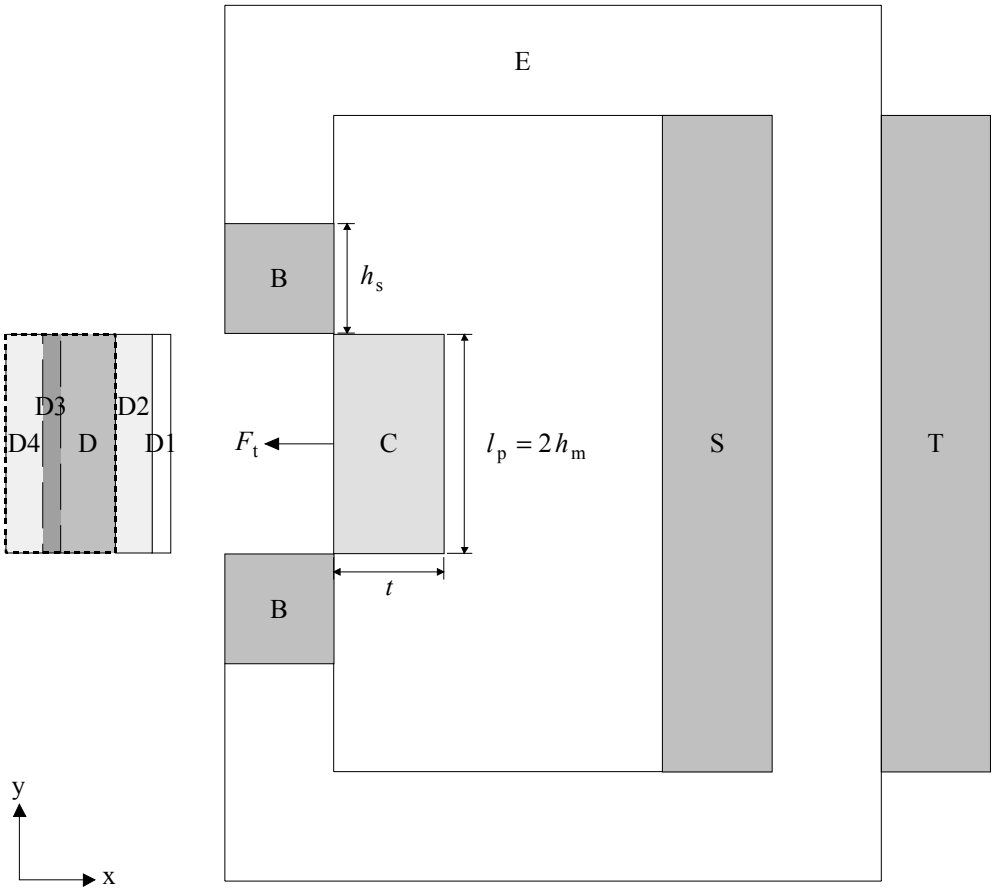

Figure 5.2. The geometry of the 2D-FEM-model of the basic transversal flux pole pair (BTFPP) of the LSR-motor. The mover is in the edge position. The dashed line indicates a passive mover pole when the phase number of the model is three. The resultant traction force F_t and the movement are in the x-direction.

The force is generated in the air gaps between regions B and C. The component of the force in the x-direction generates the traction force (tangential force component). The component of the force in the y-direction generates the normal force. The geometry illustrated in figure 5.2. has two air gaps as has the real basic pole pair of the TF-LSR-motor. The main flux goes in the (x,y)-plane and the force can be calculated by using a 2D-FEM-calculation. The flux inside the

poles goes mainly in (y,z)-plane in the real basic pole pair of the TF-LSR-motor. This flux can be modelled to go in the (x,y)-plane in the 2D-FEM-calculation, because the flux inside the poles does not generate a force. The stray flux that goes through the air from the end of the stator pole to the end of the mover pole and at the same time does not go through the air gap between the pole faces is not included in the 2D-FEM-calculation. The region E is needed to transport the flux because there is no third dimension available. Every position of the mover requires a new geometry where the mover poles are shifted to the wanted position.

The finite element mesh is generated from the geometry illustrated in figure 5.2. Figure 5.3. shows a finite element mesh containig 3034 nodes and 6025 finite triangular elements.

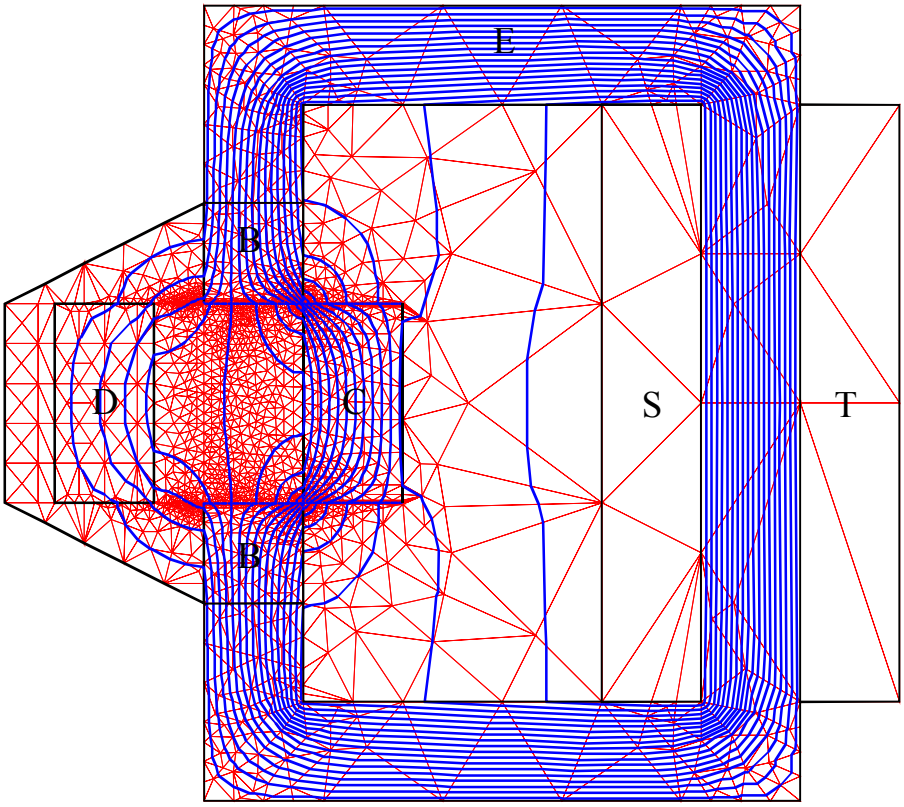

Figure 5.3. The finite element mesh of the geometry in figure 5.2. containig 3034 nodes and 6025 elements. The outer boundary is restricted with Dirichlet boundary condition (flux is tangential to the boundary). Force is calculated with body which consists of B and E regions. A five phase mover consists of C and D regions. Flux lines are calculated using material M2 and 32 kA total MMF. Region E has relative permeability 10^6.

The labels B, C and the D labels which create the passive mover pole are set to be of a non-linear magnetic material when the 2D-FEM-problem is defined to be solved. Label E is set to be of a linear material having relative permeability 10^6 (almost infinite permeable material) so it should have no effect on the calculation. It is working as a magnetic super conductor. Labels S and T are set to be of copper. Labels S and T have a current density which contributes the needed total current of the coil regions. The region around and inside the geometry is set to be air.

There is always a stray flux that goes through air between the upper and lower yoke of the region E. This stray flux can not be avoided since there is the maximum magnetic potential difference between the yokes of the region E.

The element mesh in figure 5.3. can be scaled in x- and y-directions thus the same mesh can be used for models having a different cross-sectional pole face area. Table 5.1. shows the dimensions of the basic transversal flux pole pair of the TF-LSR-motor (BTFPP) used in the 2D-FEM-calculations.

Table 5.1. The dimensions of the basic transversal flux pole pair of the TF-LSR-motor (BTFPP) used in 2D-FEM-calculations.

Dimension	Magnitude
t [mm]	100
l [mm]	100
A [mm^2]	10000
δ [mm]	0.2
h_s [mm]	150
h_m [mm]	100
d_w [mm]	50
k_w	0.6

Other dimensions not mentioned in table 5.1. are depending on the current density.

5.2.2 Other 2D-FEM-models of LSR-motors

The main flux of an LF-LSR-motor goes mainly in a true 2D-plane and the 2D-FEM-model is justified. Of course, the end effects of the poles are not included in the 2D-FEM-model. The 2D-FEM-model of the two-sided three-phase LF-LSR-motor phase 2 in the edge position is illustrated in figure 5.4.

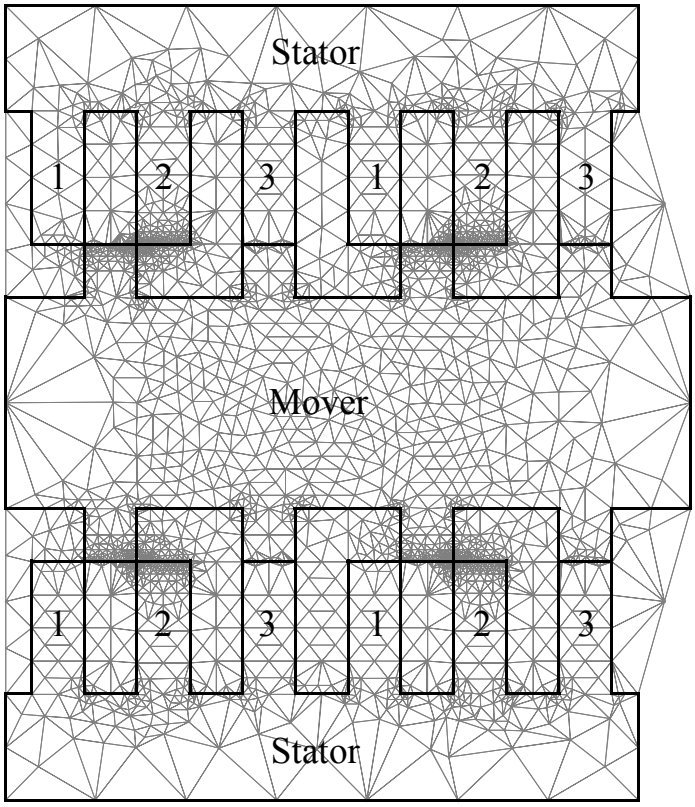

Figure 5.4. The geometry of the 2D-FEM-model of the two sided three-phase TF-LSR-motor phase 2 in the edge position. The model has 2538 nodes and 5036 elements. The stator phase poles are marked as 1, 2 and 3. Force is calculated using body which consists of the stator regions.

The LF-TLSR-motor can be analysed with the same model as the two-sided LF-LSR-motor, but the poles of the LF-TLSR-motor are round and there are no ends at all. The round shape makes it possible to use an axi-symmetric-model for the LF-TLSR-motor when the coils are round too. The axi-symmetric-model is a kind of a semi 3D-model, but it calculates as quickly as 2D-models.

5.2.3 Comparison of 2D-FEM-models

There is a comparison of different LSR-motor structures in chapter 3.5 calculated by using the 2D-FEM-model of the basic transversal flux pole pair (BTFPP), when the mover is in the edge position. The dimensions of the 2D-FEM-models and calculation results (a three-phase two sided LF-LSR-motor and a three-phase tubular LF-TLSR-motor) are given in table 3.3. and in table 3.4. The traction forces calculated by using the 2D-FEM-models of the LF-LSR-motor and the LF-TLSR-motor are compared to the results of tables 3.3. and 3.4., when the mover is in the edge position, the magnetic material is M2 and the traction force is 1000 N. The results of comparison are given in table 5.2.

Table 5.2. Comparison between the calculation results of the two-sided three-phase LF-LSR-motor found by the 2D-FEM-model (3p 2s LF-LSR) and by the 2D-FEM-model of the basic transversal flux pole pair (BTFPP 3p 2s LF-LSR, table 3.3.) and the tubular three-phase LF-LSR-motor (3p LF-TLSR) and by the 2D-FEM-model of the basic transversal flux pole pair (BTFPP 3p LF-TLSR, table 3.4.). The mover is in the edge position, the magnetic material is M2 and the traction force of all models is 1000 N.

	3p 2s LF-LSR	BTFPP 3p 2s LF-LSR	3p LF-TLSR	BTFPP 3p LF-TLSR
A [mm^2]	900	900	1600	1600
Θ[A]	6056	5825	10327	8853

The 2D-FEM-model of the LF-LSR-motor (see figure 5.4.) requires 231 A more total MMF than the BTFPP-model in order to produce 1000 N traction force in the edge position. The 2D-FEM-axi-symmetric-model of the LF-TLSR-motor requires 1474 A(turns) more total MMF than the BTFPP-model in order to produce 1000 N traction force in the edge position. It is quite clear that the LF-TLSR-motor has a large stray flux passing through the winding windows, because the width of the winding window is narrow compared to the length of the stator pole height. This can be concluded from the fact that the calculation of the 2D-FEM-axi-symmetric-model of the LF-TLSR-motor needs a larger current than the calculation of the BTFPP-model. The BTFPP-model works better when the ratio of the pole and the pole length is near unity. Although the mover of the LF-TLSR-motor can be light the construction is less practical due to the stray flux and mechanical weakness common to that kind of a construction.

5.3 3D-FEM models of TF-LSR-motors

The full model of the basic pole pair of TF-LSR-motor illustrated in figure 2.7. can be reduced to half of the model in order to reduce the size of the device to be modelled. The modelling work is started from a 2D-cross-sectional plane of the device to be modelled. Every geometrical detail has to be included into the 2D-base plane, when an extrusion technique is used to build up a 3D-mesh. The extrusion technique is used in MagNet™. The 2D-base geometry is illustrated in figure 5.5 showing a solid iron mover and a stator, the air surrounding the iron parts and the finite element mesh. The outer boundary acts as a Dirichlet boundary where the magnetic vector potential is fixed which forces the flux lines to be tangential to this boundary. In MagNet™ this is done by leaving the boundary unconstrained in 3D-models when there is air next to the boundary. The model is going to be half of the full model and there is a symmetry line in the z-direction acting as a Neumann boundary where flux lines are perpendicular to the boundary. In MagNet™ this is done by constraining every node of the symmetry plane to be a face constrain in 3D-models. The base plane mesh illustrated in figure 5.5. shows a dense and regular mesh near the air gap. The stator has the element label C, the active mover pole has the element label B and the passive mover pole has the element label D. The air is labelled as A.

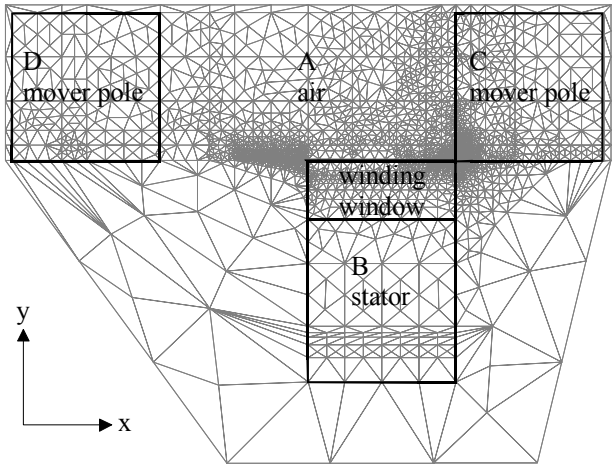

Figure 5.5. The base plane geometry and the finite element mesh of the basic transversal flux pole pair. The distance between the mover poles corresponds to a three phase motor. The active mover pole C is in the edge position. The mesh has 2862 nodes and 5686 elements.

The air gap between the stator and the mover is the most important region in the model of the prototype. The air gap should be filled with at least three layers of elements for accurate force calculation. The flux density is not changing so much in intermediate layer compared to neighbouring layers. The force calculation algorithm used in the MagNet™ software used is then able to find that intermediate layer to be the best itegration bath.

When the third dimension is added the air gap has to be considered there as well. All the nodes of the base plane mesh must have a corresponding node at the next plane i.e. all the base plane elements can be seen through the whole device in the direction of the extrusion. If the air gap is filled with very many elements, it limits the amount of planes and subdivisions which can be used to discretisate the device in the third dimension. 3D-bricks are saved when the model is extended into the direction where the air gap length of the base plane is the shortest.

The extrusion from a 2D-mesh to a 3D-mesh is done by adding copies of the base plane mesh after each other. The stator and the mover are assigned by different element labels which are changed in every plane so that the 3D-device is constructed in a proper way. The wire frame view and the surface picture of the 3D-mesh describing one half of the basic transversal flux pole pair of the TF-LSR-motor is illustrated in figure 5.6. The 3D-mesh size is 221754 bricks when the maximum allowed number of bricks is 222000 in the MagNet™ system used.

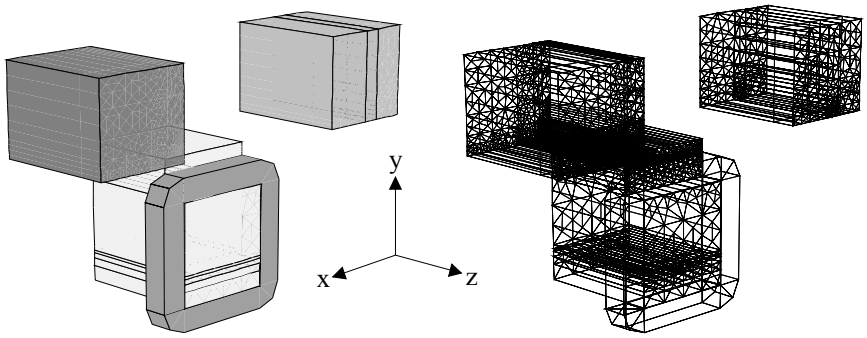

Figure 5.6. The surface picture and the wire frame view of the 3D-FEM-model describing one half of the basic transversal flux pole pair of the TF-LSR-motor. The active mover pole is in the edge position. The 3D-mesh size is 221754 bricks. The surrounding air is not shown. The planes are shown but the subdivisions of the planes are not shown.

A coil is modelled by using a separate mesh. The coil mesh actually tells which elements have the current density. The solver is then able to assign the current density to the elements in the material mesh which are common to the coil mesh and the material mesh. Coils may be current driven, or voltage driven if resistivity of the coil is also given.

The discretisation in z-direction is made by adding planes in different distances and the subdividing the space between the planes. The z-direction plane co-ordinates, the subdivisions and the brick height in z-direction of the half-model illustrated in figure 5.6. are given in table 5.3. The plane positions are shown in figure 5.7. The outer boundary closes the surrounding air inside it.

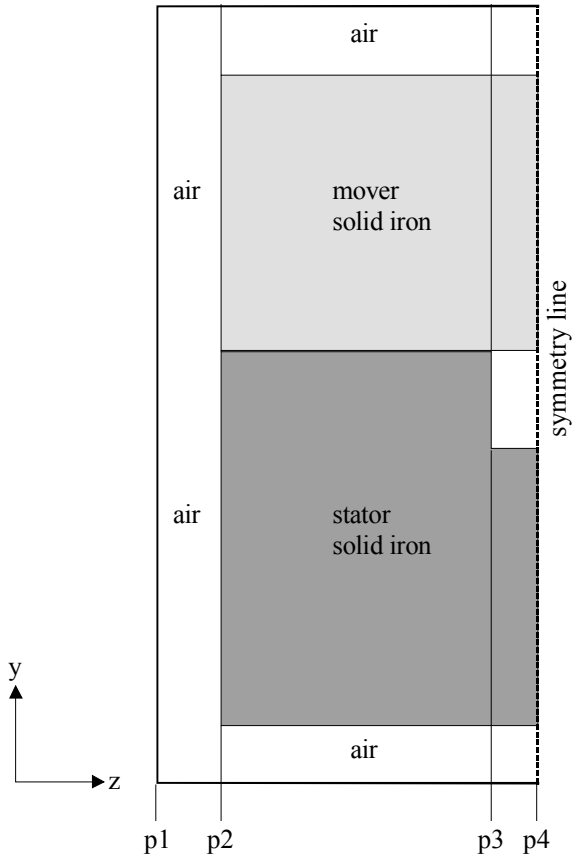

Fig.5.7. The discretisation of 3D-FEM-half-model in z-direction. The lines marked with p1, p2, p3 and p4 show the plane positions.

Table 5.3. Plane number, z-co-ordinate, subdivision between planes and corresponding brick height of 3D-FEM-half-model in figure 5.6. The plane positions in z-direction are shown in figure 5.7.

Plane number	z-co-ordinate [mm]	subdivisions	brick height [mm]
1	-127	1	2
2	-125	33	3
3	25	5	5
4	0		

The more practical transversal flux LSR-motors are studied in chapter 2.1.2. The four-sided TF-LSR-motor and tubular TF-LSR-motor can be modelled for 3D-FEM-calculations as well. The quarter-model of the four-sided TF-LSR-motor is illustrated in figure 5.8.

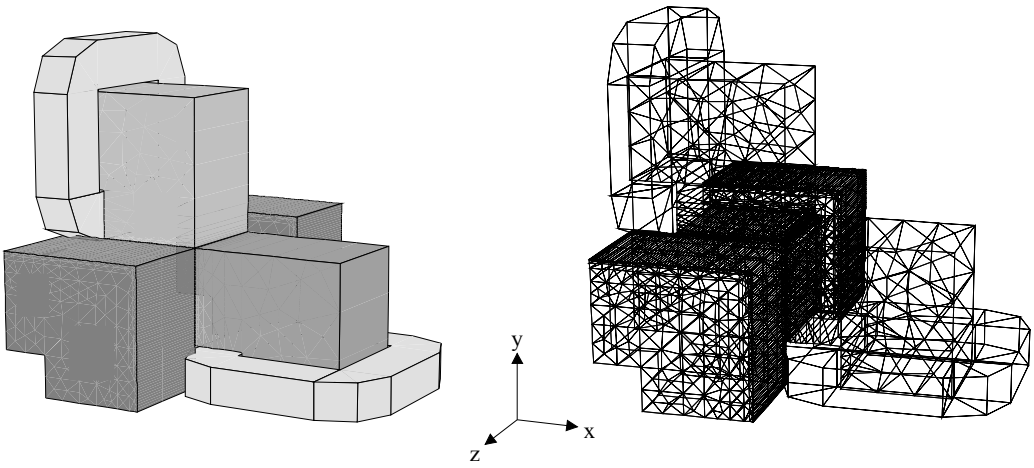

Figure 5.8. The quarter-model of the four-sided TF-LSR-motor of one pole pair in the edge position. Left picture shows the surface model and right picture shows the wire frame view of the model.

The quarter-model of the four-sided stator TF-LSR-motor with a cylindrical geometry is illustrated in figure 5.9.

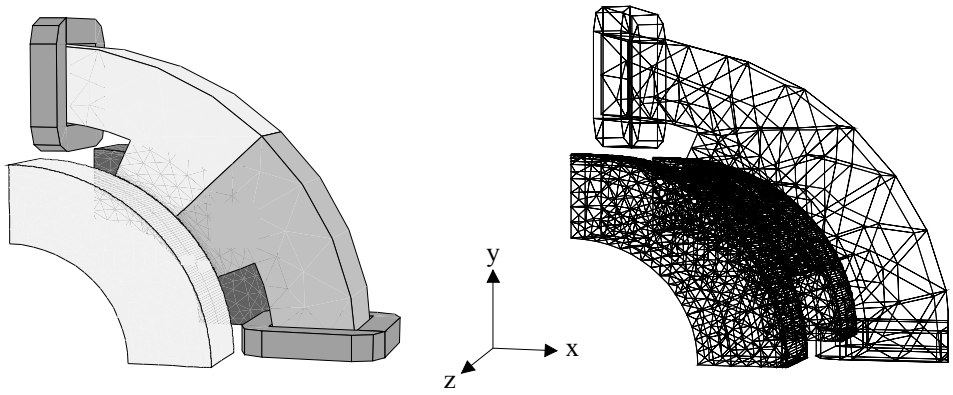

Figure 5.9. The quarter-model of the four-sided stator cylindrical TF-LSR-motor. Left picture shows the surface model and right picture shows the wire frame view of the model.

Vectorised quantities are avoided in the case of a 3D-FEM-calculation, because they cause three unknown components at each node. A static magnetic field can be solved by using scalar magnetic potentials with only one unknown to be solved at each node of the mesh. It is valid to use the total scalar potential only if there are no distributions of current density *J*. The reduced scalar potential is used to avoid the problem of existing current densities. The normal way is to use the so called two potential technique. The total scalar potential is used in ferromagnetic materials and the reduced scalar potential is used elsewhere. The mathematical presentation of FEM-implementations can be found in many text books, a good example of which is "Finite elements for electrical engineers" written by Silvester and Ferrari (1983).

5.3.1 Comparison of 3D-FEM-models of TF-LSR-motors

The dimensions of the four-sided TF-LSR-motor and the cylindrical TF-CLSR-motor were calculated in the comparison of different LSR-motor structures in chapter 3.5. The machines were calculated by using the 2D-FEM-model of the basic transversal flux pole pair (BTFPP), when the mover is in the edge position. The 3D-FEM-models illustrated in figures 5.8. and 5.9. are created by using the dimensions in tables 3.1., (a three-phase TF-LSR-motor) and 3.2. (a three-phase TF-CLSR-motor). The traction forces calculated by using 3D-FEM-models illustrated in figures 5.8 and 5.9. are compared to the results of tables 3.1. and 3.2., when the mover is in the edge position and the magnetic material is M2. The results of the comparison are given in table 5.4.

Table 5.4. Comparison between traction forces of the four-sided three-phase TF-LSR-motor calculated by the quarter 3D-FEM-calculation model (3D TF-LSR, see figure 5.8.) and by the 2D-FEM-calculation model of the basic transversal flux pole pair (BTFPP 2D TF-LSR, table 3.1.) and the cylindrical three-phase TF-LSR-motor (3D TF-CLSR, see figure 5.9.) and by the 2D-FEM-calculation model of the basic transversal flux pole pair (BTFPP 2D TF-CLSR, table 3.2.). The mover is in the edge position and the iron core material is M2.

	3D TF-LSR	BTFPP 2D TF-LSR	3D TF-CLSR	BTFPP 2D TF-CLSR
A [mm^2]	1600	1600	900	900
Θ[A]	4167	4167	5529	5529
F_t [N]	1021	1000	969	969

Because the force values of BTFPP-model and 3D-models are quite close to each other, it can be said that the BTFPP-model estimates the required size of the four-sided TF-LSR-motor and the cylindrical TF-CLSR-motor very well. The ratio of the pole width and pole length is unity for all the examined models. This might explain the good results. The 2D-arrow plot of the magnetic field and the 2D-region plot of the magnitude of the flux density is illustrated in figures 5.10a. and 5.10b. The 2D-view in figures 5.10a. and 5.10b. is taken as a slice from the overlapping edges of the poles of the quarter-3D-model in figure 5.8.

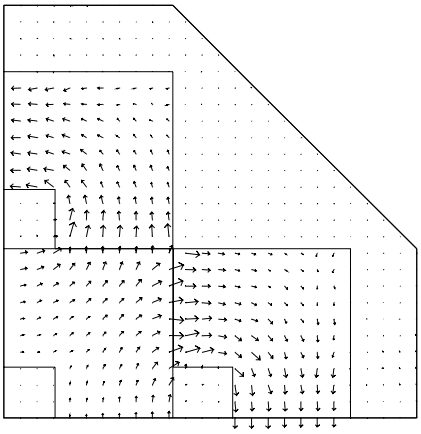

Figure 5.10a. The arrow plot of the magnetic potential of the model in figure 5.8. The position of the slice of the 3quarter-3D-model illustrated is the overlapping edges of the poles.

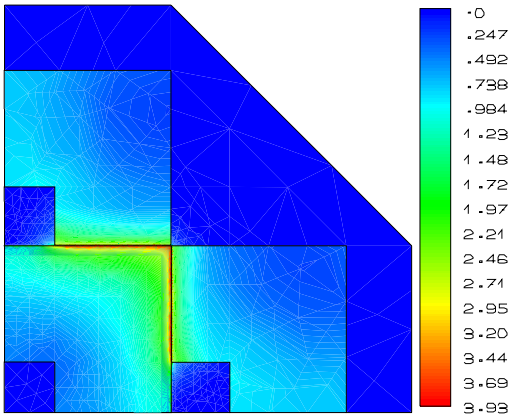

Figure 5.10b. The region plot of the magnetic flux density of the quarter-3D-model in figure 5.8. There is a strong local saturation in the overlapping pole edges. The flux density is about 3 T.

The 3D-surface plot of the magnetic flux density on the surfaces of the stator and the mover of the cylindrical TF-LSR-motor is illustrated in figure 5.11., showing the flux density distribution in the pole edges.

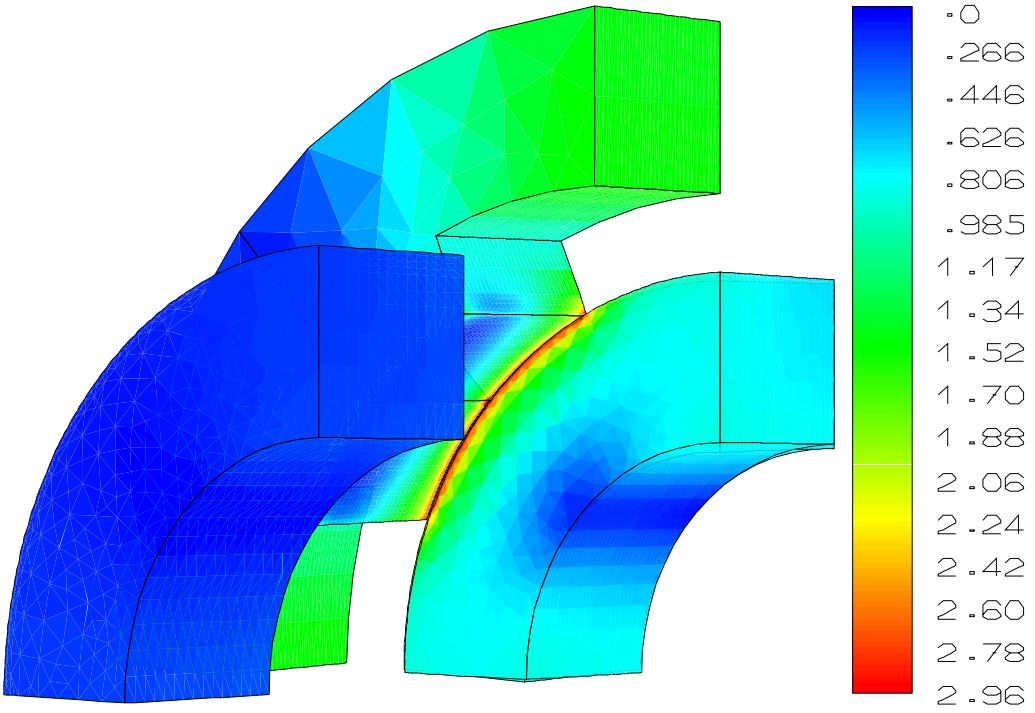

Fig.5.11. The 3D-surface plot of magnetic flux density on the surfaces of stator and mover of cylindrical TF-LSR-motor. The dark gray in the overlapping pole edges indicates a strong local saturation with flux density about 3 T.

Figures 5.10. and 5.11. show how strong the local saturation is in the overlapping pole edges of the stator and the mover. By comparing the force calculation results of the BTFPP-model and 3D-FEM-models, the BTFPP-model seems to be reasonably good for the size estimation of the four-sided TF-LSR-motor and the cylindrical TF-CLSR-motor.

5.4 Static traction force calculations of the 2D-FEM-model of the basic pole pair of an LSR-motor

The amount of force from a certain piece of iron is the initial information needed when designing an LSR-motor. The problem of forces in overlapped poles has interested many researchers during past years. *"A wide range of electromechanical devices exploits the tangential forces acting between overlapping poles or teeth, or between pairs of poles or plates and an inserted slab or plunger. A device with a single overlap zone is the most elementary and is repeated many times in conventional rotating machines"*; (Byrne, 1972. p. 2). There have been attempts to solve this force generation problem by analytical methods, which lead to a need of idealisations and restrictions, because the magnetic field distribution must be known. *"Assuming that the poles have infinite permeability and that there is a uniform-field region between adjacent pole tips and negligible field intensity at remote tips, the alignment force (per meter) is*

$$F = \tfrac{1}{2}\mu_0 H^2 g$$

where H is the field strength in the uniform-field region and g is the air gap length."; (Carpenter, 1959. p. 24). Byrne (1972. p. 2) said also: *"In general, the tangential force can be derived only from a knowledge of the field spatial distribution, which is a function of overlap."*

O'Connor (1980) studied forces in idealised saturable pole configurations by using an ideal-square (*B,H*)-material characteristic for the pole material. He proved that a non-linear magnetic field solution can be scaled under the assumption of an ideal square (*B,H*)-material characteristic.

In reality materials are non-linear and maximum saturation field density is near 2.0 T. Real magnetic fields are usually not uniformly distributed. This makes it very hard to find the solution for a force problem for practical devices on the basis of analytical hand calculations. Today's powerful low price computers and suitable software even for free make complex hand calculations useless, when the same work can be done numerically in a short time. In fact it is quite complicated to try to make an estimation of field distribution on the basis of hand calculation as

Corda and Wilkinson (1994) did in their paper "Prediction and measurement of magnetic parameters of cylindrical linear switched reluctance actuator".

The force characteristic of the transversal flux basic pole pair is studied by using the 2D-FEM-analysis and the BTFPP-model of the basic transversal flux pole pair. The mover is in the edge position except when the traction force as a function of the mover position is studied. The largest traction force is expected to appear in the edge position. The maximum traction force is obtained with somewhat overlapped poles in real devices, but the degree of overlapping depends on the geometry, phase number, material and the strong local saturation in the overlapped pole tips, which is very hard to estimate beforehand for each case. The phase number can vary and different LSR-motor structures can be analysed when the mover is in the edge position.

5.4.1 The static traction force as a function of the cross-sectional pole face area and the total MMF

The traction force is generated between the mover and the stator pole faces. The traction force is a function of the cross-sectional pole face area, the exciting total MMF of the stator pole, the material used in magnetic circuit, the air gap length between the stator and the mover pole, the phase number and the position of the mover. The effect of those variables are examined with 2D-FEM-calculation and the BTFPP-model of the basic transversal flux pole pair. The effect of the material is illustrated in figure 5.12., where the traction force is a function of the total MMF, and of the cross-sectional pole face area, and of the magnetic material. The model is a three-phase BTFPP mover in the edge position. The air gap length is scaled down from 0.2 mm of the model having the cross-sectional pole face area 10000 mm^2 (t=100 mm, l=100 mm). When the cross-sectional pole face area is 1000 mm^2 (t=10 mm, l=10 mm), the air gap length is 0.02 mm, which is not practical, but this follows the scaling law.

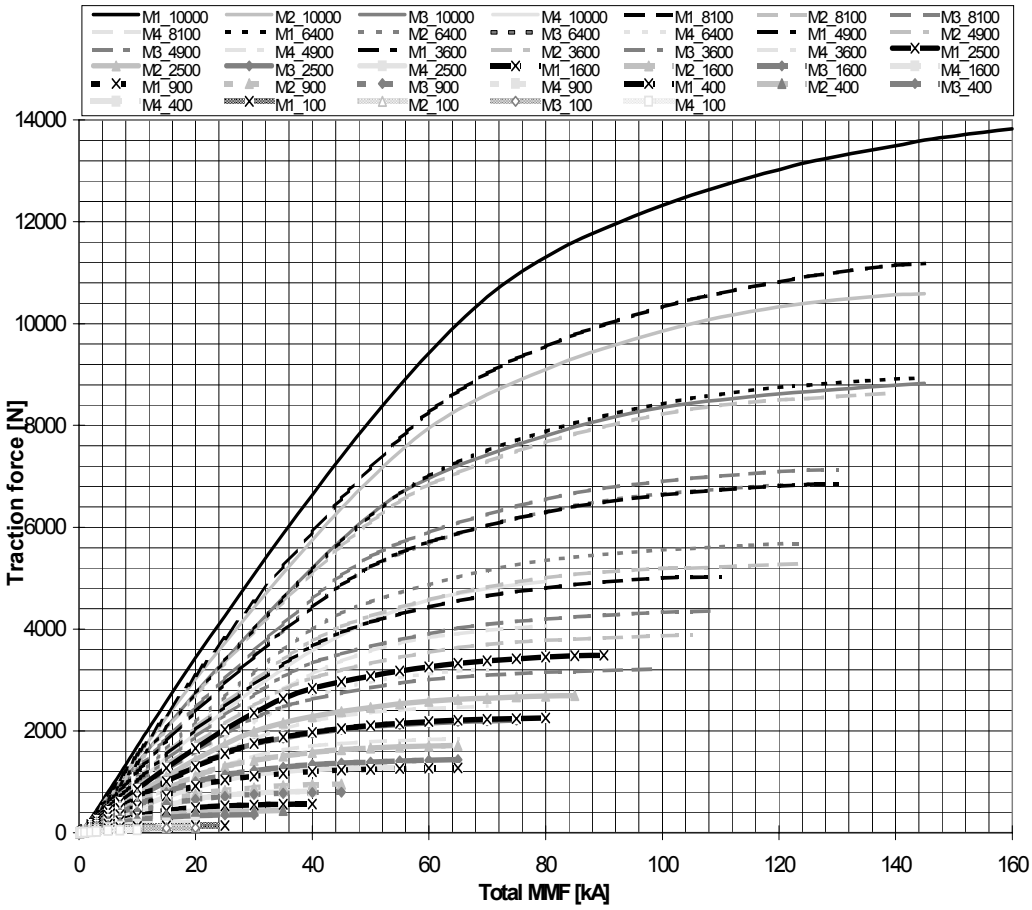

Figure 5.12. The traction force of the three-phase BTFPP mover in the edge position. Materials are M1, M2, M3 and M4 when the cross-section area of the pole is 100, 400, 600, 100, 2500, 3600, 4900, 6400, 8100 and 10000 mm^2. The labels next to the picture indicate the material and the cross-section area of the pole in mm^2 respectively. $t/l = 1$.

The effect of the material used in the magnetic circuit of the BTFPP is examined more deeply in figure 5.13. which illustrates the traction force of the BTFPP as a function of different materials, the phase number and total current, when the cross-sectional pole face area is 10000 mm^2 and the mover is in the edge position. The total MMF is limited to the linear region of the traction force which is not clearly visible in figure 5.12. Figure 5.13. shows how strongly the material characteristic affects the traction force. Materials M1, M2, M3 and M4 are only examples of the magnetic characteristic of solid steels. The material M2 is used in further studies because it may be the material closest to average constructional steel.

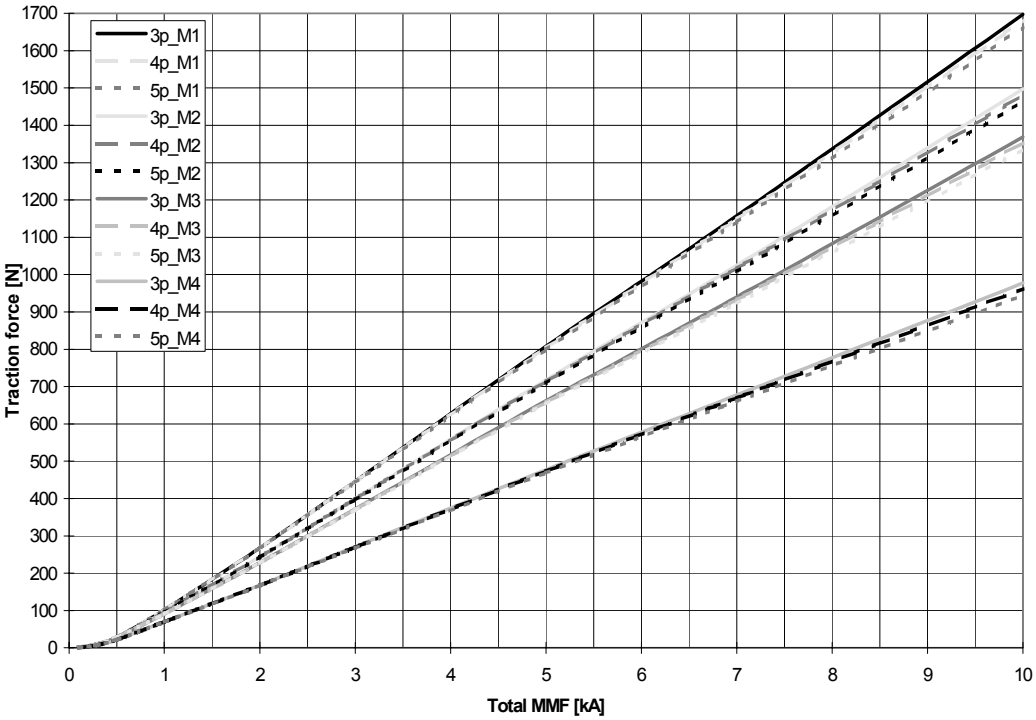

Figure 5.13. The traction force of BTFPP as a function of the total MMF, and of materials M1, M2, M3, and M4, and of phase numbers 3, 4 and 5. The cross-sectional pole face area is 10000 mm^2 and the mover is in the edge position. Labels next to the figure indicate the phase number and the material respectively. $t/l = 1$.

The traction force as a function of the phase number is illustrated in figure 5.14. The phase number does not have a considerable effect in the linear region of the traction force. The effect of the phase number is amplified when the magnetic saturation of the poles increases. Figure 5.15. shows a more detailed view of the linear region of the traction force.

Figures 5.16., 5.17., and 5.18. illustrate the traction force as a function of the cross-sectional pole face area and the total MMF. The phase numbers are three, four and five respectively. The pole material is M2 and the mover is in the edge position.

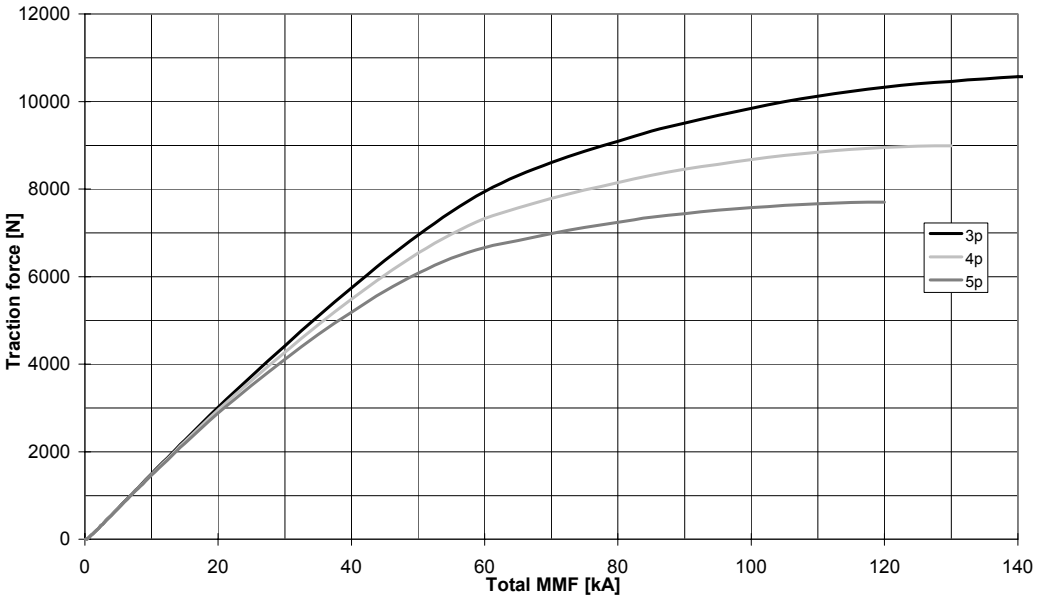

Figure 5.14. The traction force of a three-, four- and five-phase BTFPP as a function of the total MMF and phase number. The pole material is M2, the cross-sectional pole face area is 10000 mm^2 and the mover is in the edge position. Labels next to the figure indicate phase numbers three as 3p, four as 4p and five as 5p. $t/l = 1$.

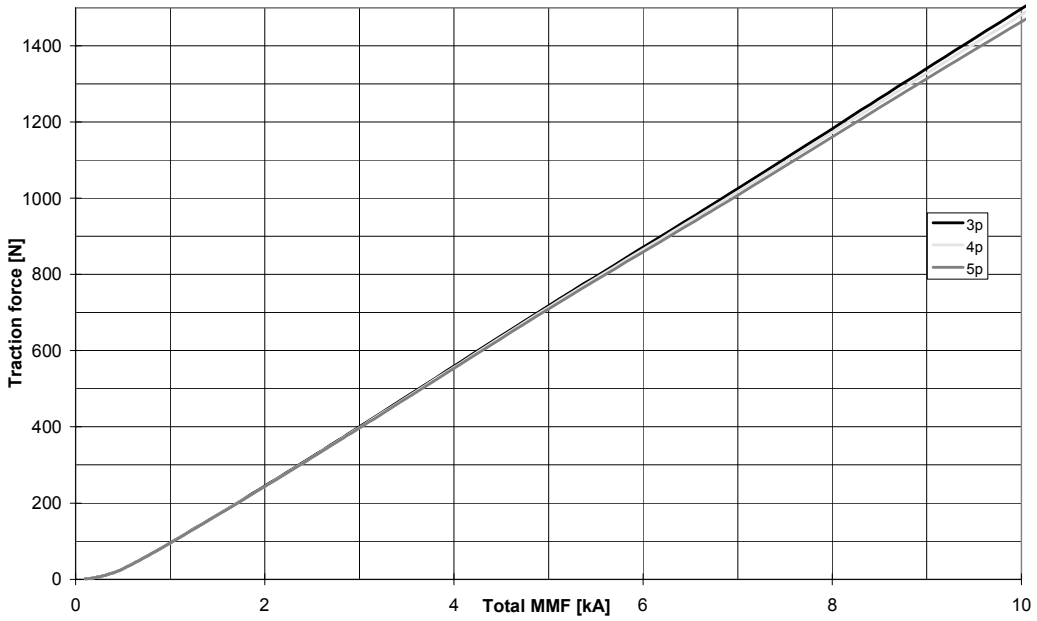

Figure 5.15. A zoomed view of figure 5.14.

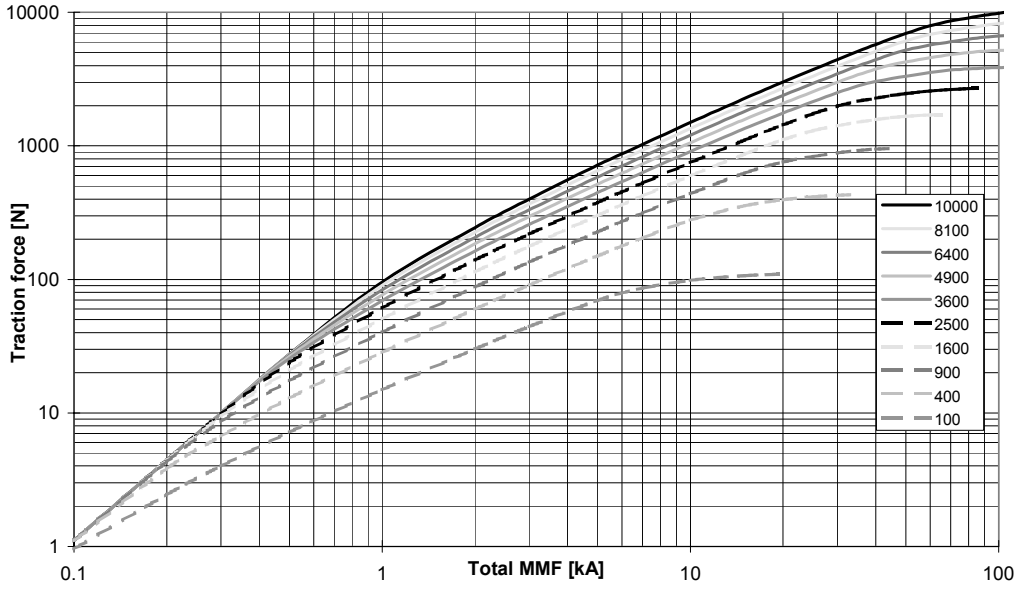

Figure 5.16. The traction force of a three-phase BTFPP as a function of the total MMF for different values of the cross-sectional pole face area. The labels next to the figure indicate the cross-sectional area 100, 400, 900, 1600, 2500, 3600, 4900, 6400, 8100 and 10000 mm^2. The pole material is M2 and the mover is in the edge position. $t/l = 1$.

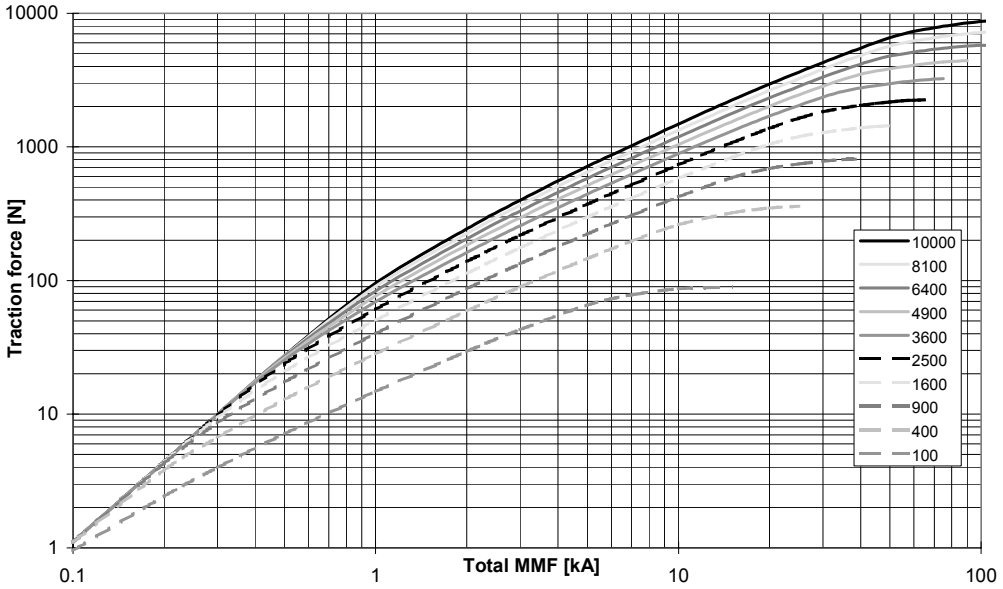

Figure 5.17. The traction force of a four-phase BTFPP as a function of the total MMF for different values of the cross-sectional pole face area. The labels next to the figure indicate cross-sectional area 100, 400, 900, 1600, 2500, 3600, 4900, 6400, 8100 and 10000 mm^2. The pole material is M2 and the mover is in the edge position. $t/l = 1$.

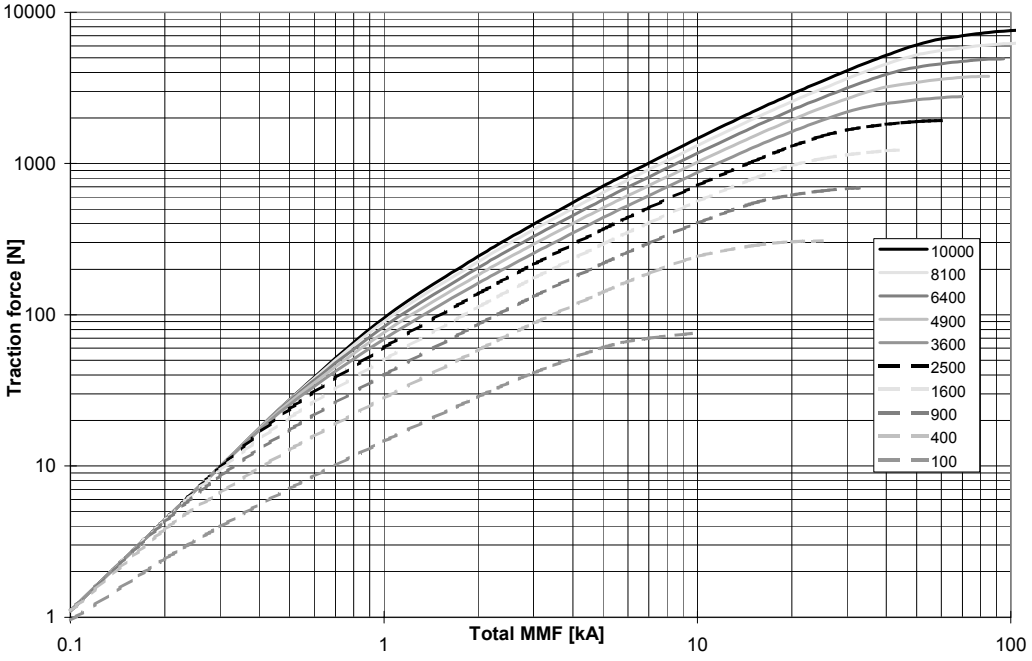

Figure 5.18. The traction force of a five-phase BTFPP as a function of the total MMF for different values of the cross-sectional pole face area. The labels next to the figure indicate the cross-sectional area 100, 400, 900, 1600, 2500, 3600, 4900, 6400, 8100 and 10000 mm^2. The pole material is M2 and the mover is in the edge position. $t/l = 1$.

5.4.2 The scaling of dimensions, current and force

Scaling is done on the basis of the air gap shear stress which is maintained constant during scaling. The air gap shear stress can be defined by means of the Maxwell stress tensors (Carpenter, 1959. p. 21). The air gap shear stress is resolved into a normal component σ_n (perpendicular to pole face) and a tangential component σ_t (perpendicular to normal component)

$$\sigma_t = \frac{B_n \cdot B_t}{2 \cdot \mu_0} = \frac{F_t}{A_\delta}, \tag{5.2}$$

$$\sigma_n = \frac{B_n^2 - B_t^2}{\mu_0} = \frac{F_n}{A}, \tag{5.3}$$

where B_n is the normal component of the flux density in the air gap between the stator and the mover pole and B_t is the tangential component of the flux density in the air gap between the stator and the mover pole. A is the cross-sectional pole face area in figure 5.19. and A_δ is the area of the air gap in the direction of movement. F_n and F_t are the normal and tangential force components (the tangential force is the traction force also) acting on the poles. Only the pole faces are shown in figure 5.19. with the fictious overlapped pole faces of the stator and the mover poles.

The scaling law can be defined only by studying the air gap region, because equations (5.2) and (5.3) are defined in vacuo. The iron in the poles can be assumed to have an infinite permeability and there is a remote winding in the magnetic circuit to provide the magnetomotive force.

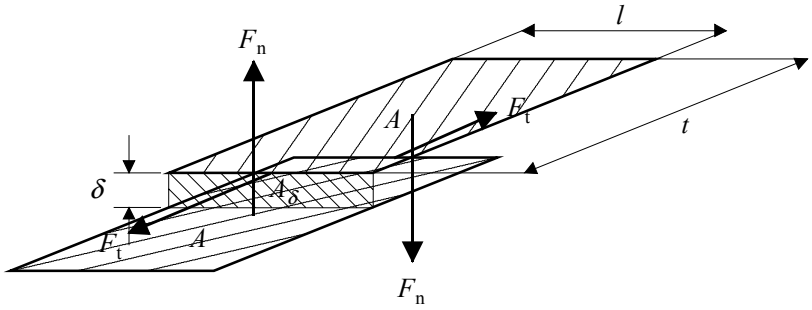

Figure 5.19. Pole faces and air gap region between the poles.

It can be seen from equations (5.2) and (5.3) that if the air gap shear stress is maintained constant during the scaling, then also the flux density has to remain the same. The flux densities and the permeabilities of equations (5.2) and (5.3) can be replaced by constants C_n and C_t

$$\sigma_t = C_t = \frac{F_t}{A_\delta}, \tag{5.4}$$

$$\sigma_n = C_n = \frac{F_n}{A}. \tag{5.5}$$

Dimensions are multiplyed by scaling factor k_{sc}

pole width: $$t_{sc} = k_{sc} \cdot t \,, \tag{5.6}$$

pole length: $$l_{sc} = k_{sc} \cdot l \,, \tag{5.7}$$

pole face area: $$\Rightarrow A_{sc} = k_{sc}^2 \cdot A \,, \tag{5.8}$$

air gap: $$\delta_{sc} = k_{sc} \cdot \delta \,, \tag{5.9}$$

air gap region: $$\Rightarrow A_{\delta sc} = k_{sc}^2 \cdot A_{\delta} \,, \tag{5.10}$$

pole height: $$h_{sc} = k_{sc} \cdot h \,, \tag{5.11}$$

pole volume: $$\Rightarrow V_{sc} = k_{sc}^3 \cdot V \,, \tag{5.12}$$

pole mass: $$\Rightarrow M_{sc} = k_{sc}^3 \cdot M \,, \tag{5.13}$$

where h is the height, V is the volume and M is the mass of the mover or stator pole. Subscript sc indicates a scaled value.

When equation (5.10) is substituted to equation (5.4), and equation (5.8) is substituted to equation (5.5) the scaling law of the normal and the tangential forces are obtained

$$F_{nsc} = k_{sc}^2 \cdot F_n \,, \tag{5.14}$$

$$F_{tsc} = k_{sc}^2 \cdot F_t \,. \tag{5.15}$$

The scaling law of the total current Θ can be defined by means of the normal flux density component. If the poles are shifted in alignment, then the tangential flux density component vanishes and there is only the normal flux component and its field strength left

$$\Theta = \delta \cdot H_{\mathrm{n}} = \delta \cdot \frac{B_{\mathrm{n}}}{\mu_0} = \delta \cdot \mathrm{C_a}\,, \tag{5.16}$$

where Θ is the total MMF in the coil and $\mathrm{C_a}$ is a constant in scaling.

The total MMF scaling law is then obtained from equation (5.2)

$$\Theta_{\mathrm{sc}} = k_{\mathrm{sc}} \cdot \Theta\,. \tag{5.17}$$

Traction forces of a three-phase BTFPP have been illustrated in figure 5.12. as a function of the total MMF, and of the cross-sectional pole face area, and of the magnetic material. The mover is in the edge position. The traction force values and the currents of three-phase, four-phase and five-phase BTFPPs with a cross-sectional pole face area of 100 mm^2 (material M2, t/l = 1) have been scaled up by 2. The scaled values have been compared to the 2D-FEM-calculated traction force values of three-phase, four-phase and five-phase BTFPPs with a cross-sectional pole face area of 400 mm^2 (material M2, t/l = 1). The comparison result is illustrated in figure 5.20.

The difference of the scaled traction force values and the directly calculated traction force values are mainly resulting from discretisation errors in a FEM-model. This makes it possibile to estimate the error in the force calculation caused by the software used. The difference as a function of the scaling factor can be taken as an average error of force calculation accuracy. The 2D-FEM-results of BTFPP with a cross-sectional pole face area of 100 mm^2 (t/l = 1) are scaled up by scaling factors 2, 3, 4, 5, 6, 7, 8, 9 and 10 and are then compared to corresponding 2D-FEM-calculation results as a function of the current of each cross sectional pole face area. The average error is illustrated in figure 5.21.

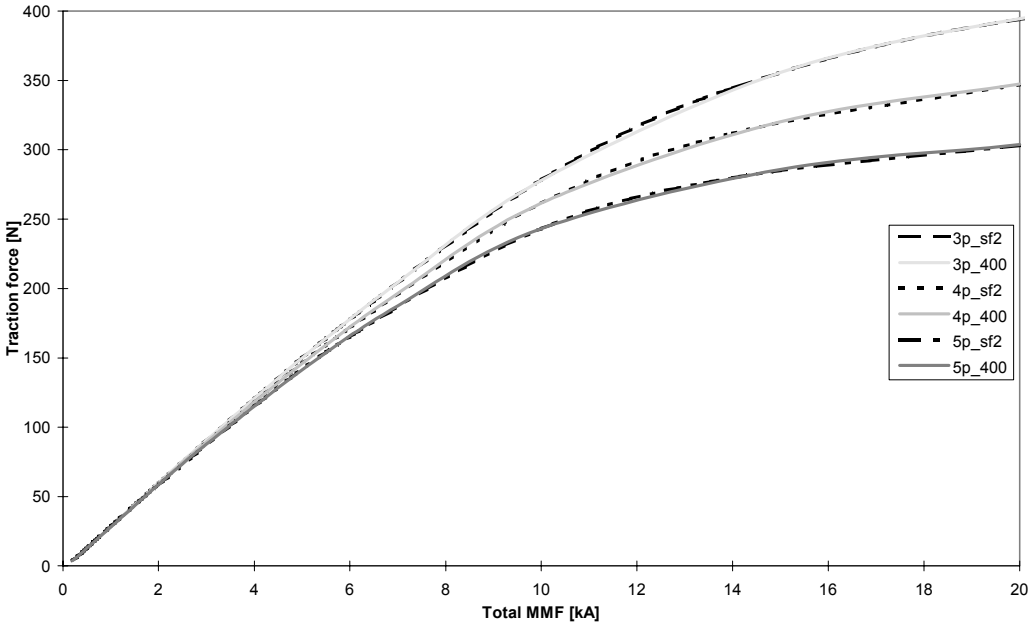

Figure 5.20. The comparison of traction forces as a function of the total MMF between the scaled values (scaling factor 2, indicated as sf2) of three-phase (indicated as 3p_sf2), four-phase (indicated as 4p_sf2), and five-phase (indicated as 5p_sf2) BTFPPs, and 2D-FEM-calculated values of three-phase (indicated as 3p_400), four-phase (indicated as 4p_400) and five-phase (indicated as 5p_400) BTFPPs with the cross-sectional pole face area of 400 mm^2. $t/l = 1$.

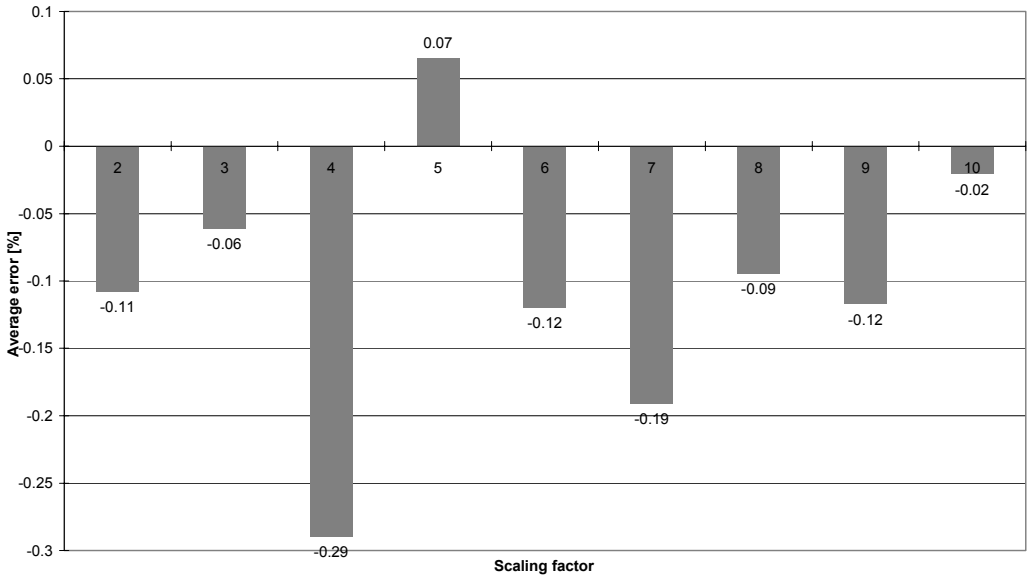

Figure 5.21. The average error of the force calculation of the FEM-software used as a function of the scaling factor. The error is the difference between the scaled traction force calues and the directly FEM-calculated traction force values.

5.4.3 The static traction force as a function of the length of air gap

The reluctance of an LSR-motor is an increasing function of the air gap length. The total current which is required in order to produce the wanted traction force is at a minimum when the air gap length is the shortest allowed. The air gap length should be as small as practicable (Stephenson, 1989. p. 57). The shortest length of the air gap is limited by mechanical and constructional restrictions. The effect of the length of the air gap on the traction force when the mover is in the edge position, is illustrated in figure 5.22. for the three-phase BTFPP, and in figure 5.23. for the four-phase BTFPP, and in figure 5.24. for the five-phase BTFPP. The pole material is M2 and the cross-sectional pole face area is 10000 mm^2 (t/l = 1). The length of the air gap varies from 0.2 mm to 1.0 mm. The effect of the air gap length on the traction force seems to be quite linear.

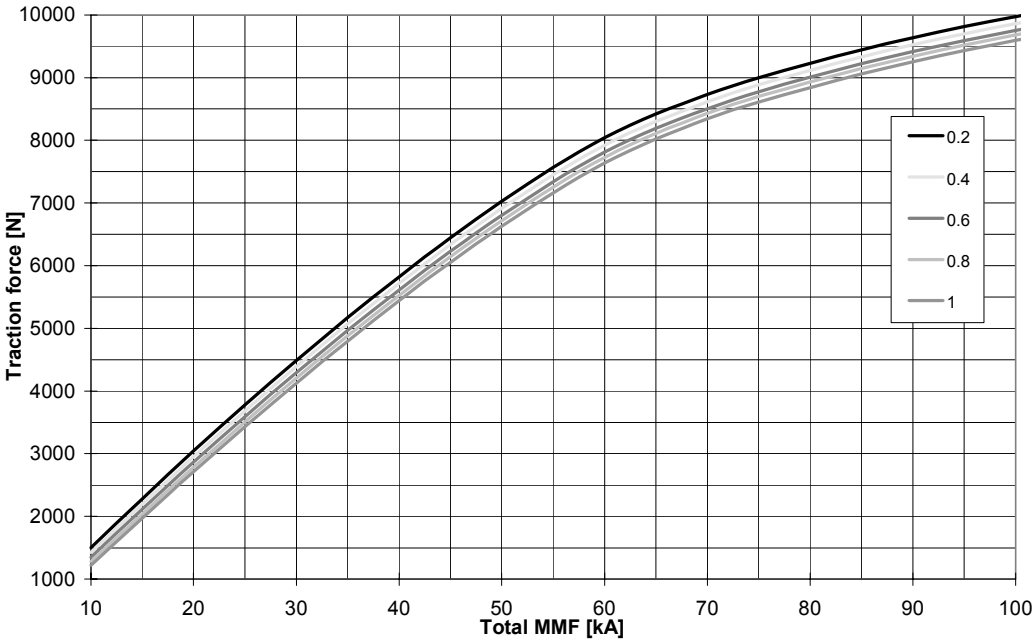

Figure 5.22. The traction force of a three-phase BTFPP as a function of the length of the air gap and the total MMF. The mover is in the edge position and the pole material is M2. The labels next to the figure indicate the length of the air gap 0.2, 0.4, 0.6, 0.8 and 1.0 mm.

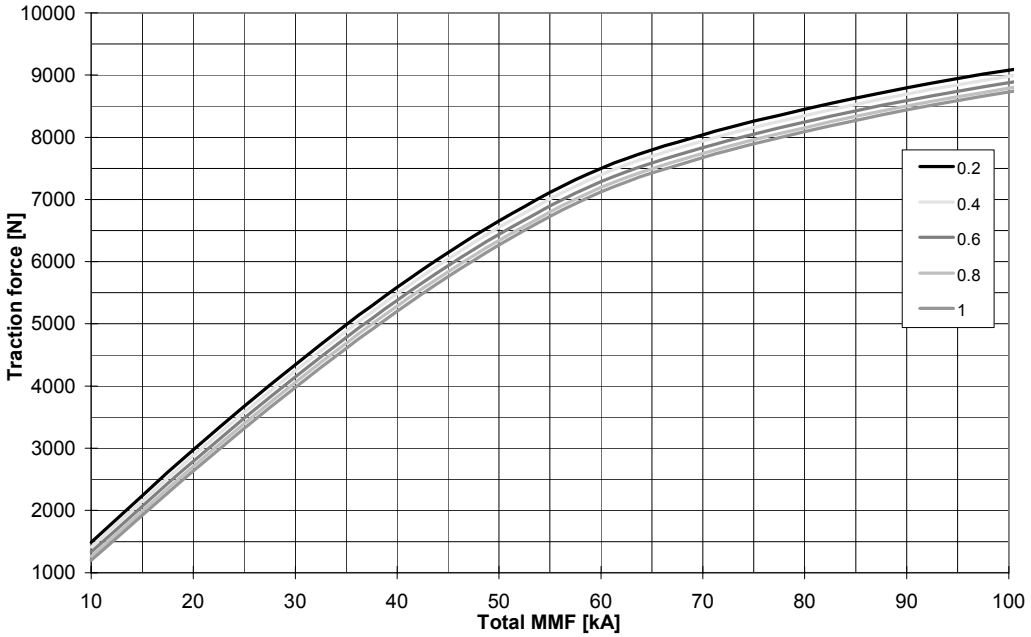

Figure 5.23. The traction force of a four-phase BTFPP as a function of the length of the air gap and total MMF. The mover is in the edge position and the pole material is M2. The labels next to the figure indicate the length of the air gap 0.2, 0.4, 0.6, 0.8 and 1.0 mm.

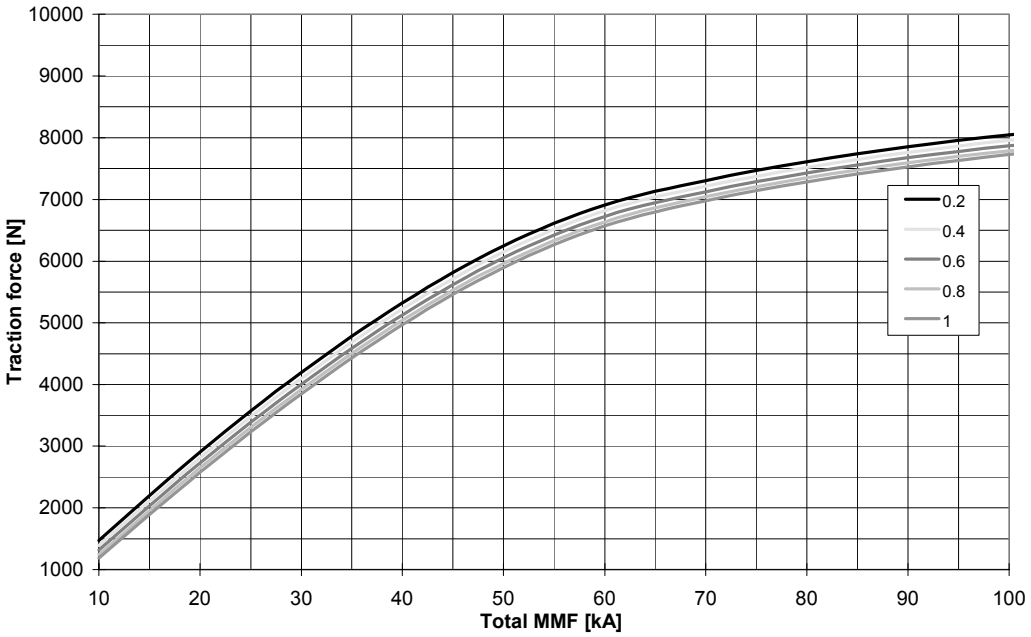

Figure 5.24. The traction force of a five-phase BTFPP as a function of the length of the air gap and total MMF. The mover is in the edge position and the pole material is M2. The labels next to the figure indicate the length of the air gap 0.2, 0.4, 0.6, 0.8 and 1.0 mm.

5.4.4 The static traction force as a function of the mover position

An estimation of the available continuous traction force in any mover position is obtained, when the static traction forces are calculated in different mover positions and the forces of the individual poles are combined. Although an individual phase of a three-phase LSR-motor has the largest traction force compared to four and five-phase LSR-motors, the continuous traction force production is quite different. Continuous traction forces of three-phase, four-phase and five-phase BTFPP-models illustrated in figures 5.25., 5.26, 5.27. are calculated by means of a 10000 mm^2 cross-sectional pole face area (100mm x 100mm pole). The pole material is M2. The pole width and the cross-sectional pole face area and the current density are the same for the examined three-phase, four-phase and five-phase motors.

The traction force curves of the individual phases are more overlapped when the phase number increases. The three-phase LSR-motor can actually have only one active phase per time as it is illustrated in figure 5.25. The four-phase LSR-motor can have two active phases nearly all the time. The change of phase leaves only one phase active as it is illustrated in figure 5.26. The five-phase LSR-motor has two active phases all the time as it is illustrated in figure 5.27. The continuous traction forces of three-phase, four-phase and five-phase LSR-motors are illustrated in figure 5.28.

The LSR-motor can produce a traction force in the same direction with half of a mover pole pitch. The positions determinig properties of the continuous traction force curve can be defined, when the zero point of the position is fixed to the point of the unaligned mover position of one phase. The traction force pulse pitch of one phase τ_p (see figure 5.27.) is then

$$\tau_p = \frac{\tau_m}{2}. \tag{5.18}$$

The traction force pulse pitch of the next phase follows after distance τ_d (see figure 5.27.)

$$\tau_d = \tau_m - \tau_s. \tag{5.19}$$

The point of the minimum traction force of the continuous traction force curve $x_{\min}$ (see figure 5.27.) is

$$x_{\min} = \tau_{\mathrm{m}} - \tau_{\mathrm{s}} . \tag{5.20}$$

The point of the maximum traction force of the continuous traction force curve $x_{\max}$ (see figure 5.27.) is

$$x_{\max} = \frac{x_{\min}}{2} . \tag{5.21}$$

The individual traction force pulses of phases neighbouring each other are overlapping by the distance τ_{ovl} (see figure 5.27.)

$$\tau_{\mathrm{ovl}} = \tau_{\mathrm{s}} - \frac{\tau_{\mathrm{m}}}{2} . \tag{5.22}$$

The minimum traction force of the continuous traction force curve $F_{\min}$ determines the force available for the starting of the motor in any mover position. The mean value of the continuous traction force curve F_{mean} can be taken as a nominal traction force which corresponds to the chosen nominal total current in steady state, when iron losses are neglected. Table 5.5. shows the minimum traction force of the continuous traction force curves and the mean traction force of three-phase, four-phase and five-phase BTFPPs as a function of some constant total MMFs.

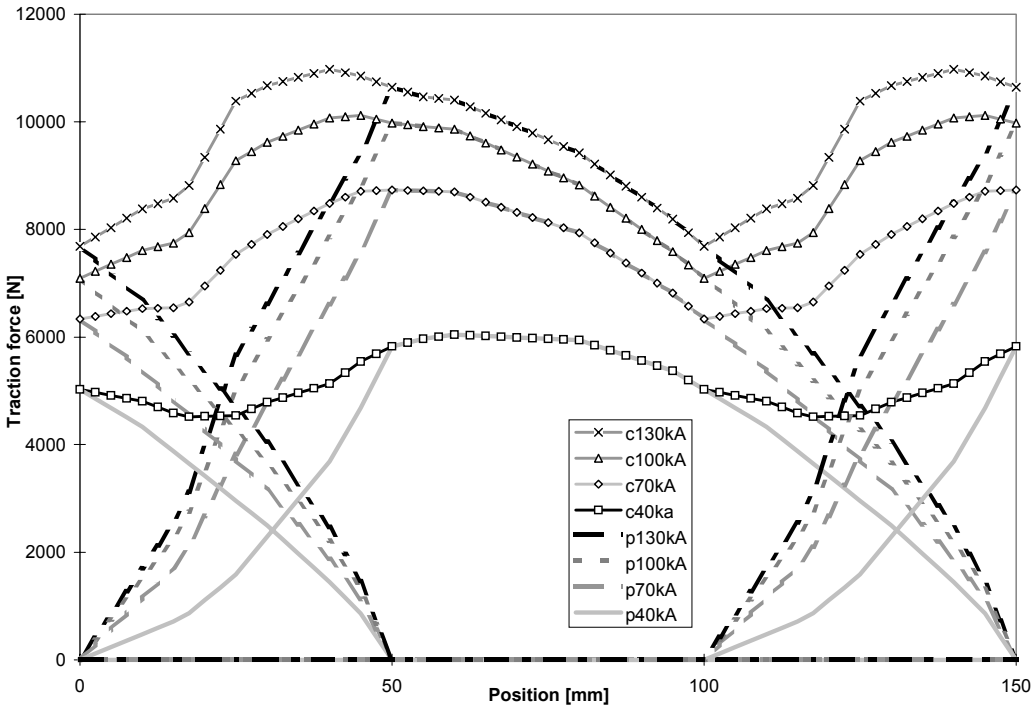

Figure 5.25. The traction force of a three-phase BTFPP as a function of mover position and total current. The cross-sectional pole face area is 10000 mm^2 (t 100 mm, l 100 mm) and the pole material is M2. The continuous traction force is obtained by summing up the individual traction force pulses. The labels next to the figure indicate the continuous traction force (c) and the force per phase (p) and the total MMF used in [kA].

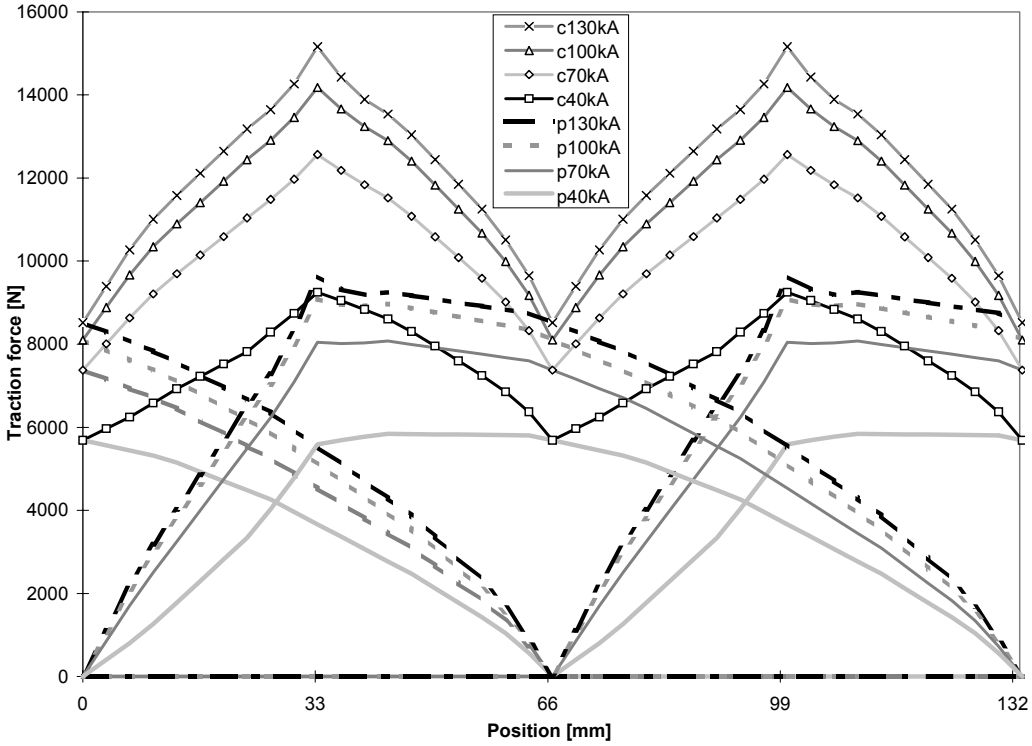

Figure 5.26. The traction force of a four-phase BTFPP as a function of mover position and total current. The cross-sectional pole face area is 10000 mm^2 (t 100 mm, l 100 mm) and the pole material is M2. The continuous traction force is obtained by summing up the individual traction force pulses. The labels next to the figure indicate the continuous traction force (c) and the force per phase (p) and the total MMF used in [kA].

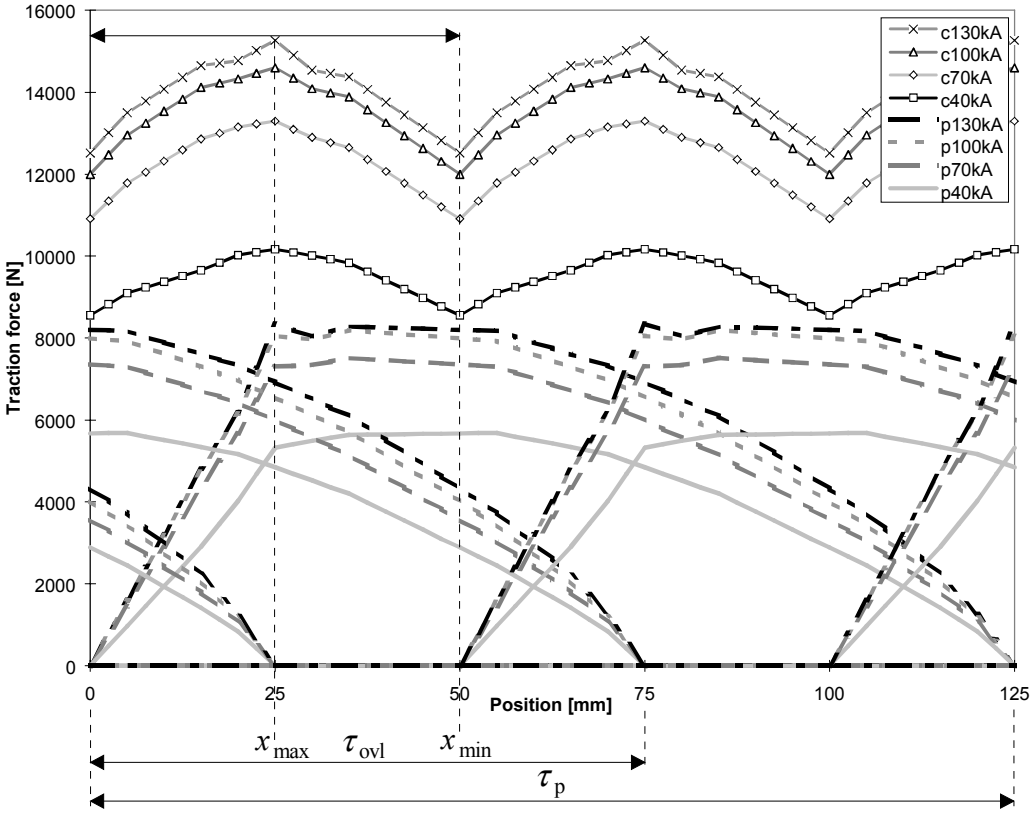

Figure 5.27. The traction force of a five-phase BTFPP as a function of mover position and total current. The cross-sectional pole face area is 10000 mm^2 (t 100 mm, l 100 mm) and the pole material is M2. The continuous traction force is obtained by summing up the individual traction force pulses. The labels next to picture indicate the continuous traction force (c) and the force per phase (p) and the total MMF used in [kA].

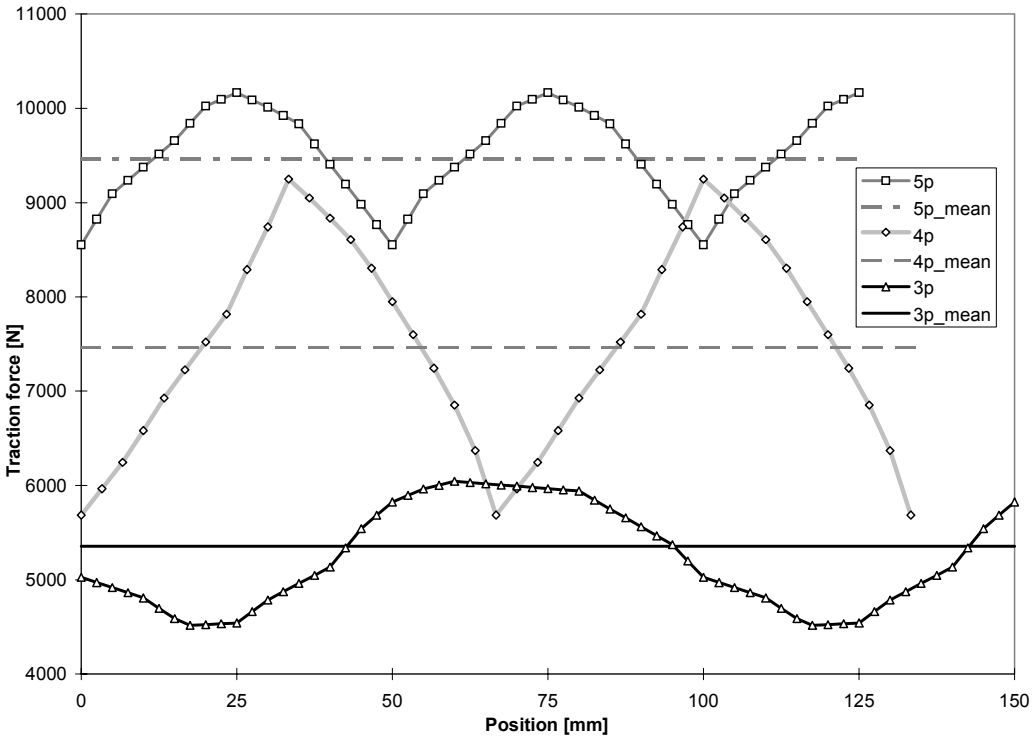

Figure 5.28. The continuous traction force of three-phase, four-phase and five-phase BTFPPs as a function of the mover position with 40 kA total MMF . The cross-sectional pole face area is 10000 mm^2 (t 100 mm, l 100 mm) and the pole material is M2. The pole width and the cross-sectional pole face area and the current density are the same for the three-phase, four-phase and five-phase motors. The continuous traction force is obtained by summing up the individual traction force pulses. The labels next to picture indicate the three-phase motor (3p), four-phase motor (4p) and five-phase motor (5p) and the mean values of the curves as "mean".

Table 5.5. The minimum traction force F_{min}, and the mean value F_{mean} of the continuous traction force curve of three-phase, four-phase and five-phase BTFPPs. The cross-sectional pole face area is 10000 mm^2 (t 100 mm, l 100 mm) and the pole material is M2. F_{max} is the maximum traction force of the continuous traction force curve. F_{ep} is the traction force mover in the edge position.

m	Θ [kA]	F_{mean} [N]	F_{min} [N]	F_{min}/F_{mean}	F_{ep}/F_{mean}	F_{min}/F_{ep}	F_{min}/F_{max}
	40	5354	4517	0.84	1.09	0.78	0.75
3	70	7675	6336	0.83	1.14	0.73	0.73
	100	8840	7093	0.80	1.13	0.71	0.70
	130	9559	7687	0.80	1.11	0.72	0.70
	40	7464	5685	0.76	0.75	1.02	0.61
4	70	10110	7377	0.73	0.80	0.92	0.59
	100	11308	8100	0.72	0.80	0.89	0.57
	130	11950	8519	0.71	0.81	0.88	0.56
	40	9464	8552	0.90	0.56	1.61	0.84
5	70	12274	10911	0.89	0.60	1.49	0.82
	100	13466	11997	0.89	0.60	1.49	0.82
	130	13897	12519	0.90	0.60	1.50	0.82

It can be concluded from (F_{min}/F_{ep}) values that the three-phase motor is not able to use all the traction force potential of one phase, because the ratio (F_{min}/F_{ep}) is below unity. Four-phase and five-phase motors can have two active phases per time. The four-phase motor has the ratio (F_{min}/F_{ep}) just under unity. The five-phase motors has the ratio (F_{min}/F_{ep}) always above unity, about 1.5. The ratios shown in table 5.5. are valid when the mover and the stator poles have an equal width and the space between two stator poles is equal to the pole width.

The pulsating traction forces illustrated in figure 5.28. must be smoothed by a proper current control. As the ratio (F_{min}/F_{ep}) shows, the three-phase motor needs always current profiling in order to have a smooth continuous traction force. The need for current profiling in the four-phase and five-phase case is much less than in the three-phase case.

The ratio (F_{min}/F_{ep}) shows also that a five-phase motor can have smaller poles than the three and four-phase motors, when the criterion for dimensioning is the maximum starting traction force required in order to the start motor in every mover position. As table 5.5. shows the four- and the five-phase motors have a stronger starting traction force than the three-phase motor, when pole dimensions are the same. The sizes of the four and the five-phase BTFPP-models have been scaled down from the three-phase BTFPP-model by using the values of table 5.5. in order to get the 4500 N starting traction force. The scaled values (in p.u.) are shown in table 5.6. The t and l are same and the ratio of t and l is unity and it remains the same during the scaling.The stroke length is not considered in table 5.6. so the mass of the mover must be calculated during the design process. Table 5.6. can give some guidelines which may be useful for the design.

Table 5.6. The scaling factor, the total MMF, the cross-sectional pole face area, and the total mass of the three-phase, the four-phase and the five-phase BTFPP-models. The starting traction force is 4500 N. t/l=1.

m	k_{sc}	Θ [p.u.]	A [p.u.]	M [p.u.]
3	1	1	1	1
4	0.89	0.89	0.79	0.71
5	0.72	0.72	0.52	0.37

Figures 5.25., 5.26. and 5.27. show that only sample mover positions need to be analysed with FEM-calculations for a rough estimation of the minimum, maximum and mean values of the continuous traction force. The minimum and the maximum traction force composition per phase number is shown in table 5.7., when the cross-sectional pole face area is 10000 mm^2 (t 100 mm, l 100 mm) and the pole material is M2. The shapes of the continuous traction force curves are pulsating with the constant feed current. The traction force pulses of the different phases are overlapping. The amount of overlap is determined by the phase number and the pole width. The functions of the minimum traction force value F_{min} and the maximum traction force value F_{max} can be derived by using the curve of the corresponding phase $F(x)$ due to periodicity.

The rough estimate of the mean value of the continuous traction force curve can be found by deriving the average value F_{ave} from the minimum and the maximum values of the traction forces of the continous traction force curve F_t

$$F_{\text{ave}} = \frac{1}{2}\left(F_{\min} + F_{\max}\right). \tag{5.23}$$

The mean values of the curves in Figure 5.28. are compared in table 5.8. to the average values calculated by equation (5.23). The comparison shows that the average traction force value calculated by equation (5.23) can estimate the available mean traction force in any mover position with a few percent uncertainty in this case.

Table 5.7. Composition of the minimum $F_{\min}$ and the maximum $F_{\max}$ traction forces of the continuous traction force curves. Function $F_{\text{tp}}(x)$ is the traction force curve of the individual phase.

m	$F_{\max}$	$F_{\min}$
3	$F_{\text{tp}}\left(\frac{1}{6}\tau_{\text{m}}\right)$	$F_{\text{tp}}\left(\frac{1}{3}\tau_{\text{m}}\right)$
4	$F_{\text{tp}}\left(\frac{1}{8}\tau_{\text{m}}\right) + F_{\text{tp}}\left(\frac{3}{8}\tau_{\text{m}}\right)$	$F_{\text{tp}}\left(\frac{1}{4}\tau_{\text{m}}\right)$
5	$F_{\text{tp}}\left(\frac{1}{10}\tau_{\text{m}}\right) + F_{\text{tp}}\left(\frac{3}{10}\tau_{\text{m}}\right)$	$F_{\text{tp}}\left(\frac{1}{5}\tau_{\text{m}}\right) + F_{\text{tp}}\left(\frac{2}{5}\tau_{\text{m}}\right)$

Table 5.8. Comparison between the mean values of continuous traction force curves and average values, when the cross-sectional pole face area is 10000 mm^2 (t 100 mm, l 100 mm) and material is M2.

m	Θ [kA]	F_{mean} [N]	F_{ave} [N]	error [%]
	40	5354	5425	-1.3
3	70	7675	7534	1.8
	100	8840	8534	3.5
	130	9559	9163	4.1
	40	7464	7468	-0.1
4	70	10110	9972	1.4
	100	11308	11141	1.5
	130	11950	11842	0.9
	40	9464	9359	1.1
5	70	12274	12104	1.4
	100	13466	13296	1.3
	130	13897	13893	0.7

5.4.5 The air gap shear stress

The ratio of the static traction force and the cross-sectional area of the air gap can be defined to be the air gap shear stress σ [N/m^2]. The air gap shear stress, or its equivalent TRV (torque per unit rotor volume) in rotating motors, forms usually the basis of design. The air gap shear stress is the basis of the initial guess of the pole face area of the TF-LSR-motor and is related to the current density and the virtual current loading A_{e}. The virtual magnetomotive force waveforms of the air gap can be defined by looking figures 5.25., 5.26. and 5.27. Figure 5.29. illustrates the magnetomotive force curve in the air gap which can be drawn if the current is DC-current and the mover is moved slowly by the distance of the stator pole pitch τ_{s} and each phase capable to produce traction force is magnetised. The MMF pulses of the individual phases are added to each other at the distance of the L_{e}. in the same way as when the MMF-curve of the SM- or IM-machine is constructed.

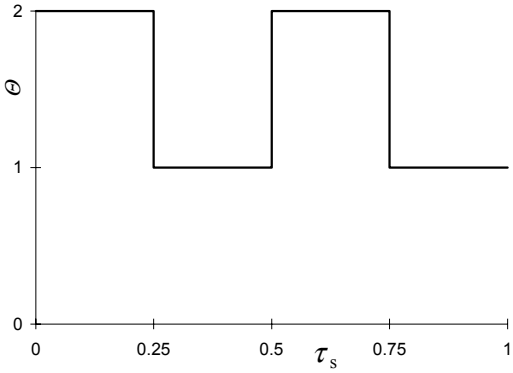

Figure 5.29a. The virtual magnetomotive force curve of the three-phase TF-LSR-motor. Θ is the total MMF of the individual phase winding.

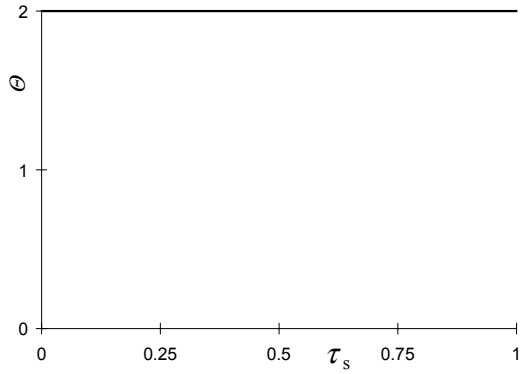

Figure 5.29b. The virtual magnetomotive force curve of the four-phase TF-LSR-motor. Θ is the total MMF of the individual phase winding.

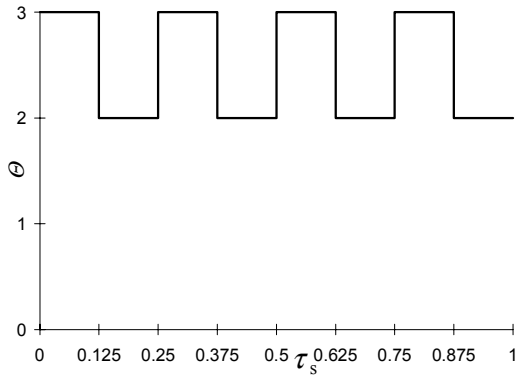

Figure 5.29c. The virtual magnetomotive force curve of the five-phase TF-LSR-motor. Θ is the total MMF of the individual phase winding.

The virtual current loading can be defined to be the mean magnetomotive force in the air gap divided by the electrical length of the stator. The current loading is derived by using figure 5.29.

$$A_{\mathrm{e}} = \begin{cases} \dfrac{1.5\Theta}{L_{\mathrm{e}}} & ,m = 3 \\ \dfrac{2\Theta}{L_{\mathrm{e}}} & ,m = 4 \\ \dfrac{2.5\Theta}{L_{\mathrm{e}}} & ,m = 5 \end{cases} \tag{5.24}$$

$$\Rightarrow A_{\mathrm{e}} = \frac{m}{2}\frac{\Theta}{L_{\mathrm{e}}} = \frac{\Theta}{4t}. \tag{5.25}$$

The area from which the traction force is found has to include the winding window area of the TF-LSR-motor as well. The area covered by the stator A_s is

$$A_s = L_e \cdot l_p = 4m\left(A + \frac{\Theta}{k_w J} \right). \tag{5.26}$$

The air gap shear stress σ can be now defined to be

$$\sigma = \frac{F_{mean}}{A_s}. \tag{5.27}$$

The output equation for AC-machines (torque per unit rotor volume) is normally represented as

$$\frac{T_{em}}{V_r} = K_1 \hat{B} A_e, \tag{5.28}$$

where K_1 is a coefficient based on machine type and $\hat{B}$ is the magnetic loading. For AC-machines K_1 is (Harris, 1991. p. 304)

$$K_1 = \frac{\pi}{\sqrt{2}} \xi_1 \eta \cos(\varphi), \tag{5.29}$$

where ξ_1 is the winding factor for the fundamental wave, η is the efficiency of the stator winding and $\cos(\varphi)$ is the stator power factor.

According to Miller (1993. p. 164) the air gap shear stress and the torque per unit rotor volume has a relation

$$\sigma = \frac{K_1}{2} \hat{B} A_e = K_2 \hat{B} A_e. \tag{5.30}$$

Vogt (1996) has published tables for the electrical loading A_e (p. 433) and for the magnetical loading (p. 435) of the normal sinusoidal flux rotating electrical machines. If ideal conditions are assumed, then ξ and η are 1. cos(φ) can be fixed to 1 for the SM-machine. Because the power factor of the IM-machine depends on the machine size it is assumed to be 0.9 for the IM-machine. Now, the koefficient K_2 can be assumed to be about 1. Because of the sinusoidal flux distribution, the air gap shear stress for the SM- and IM-machines can be defined to be A_e times $\hat{B}$. This air gap stress definiton can be taken as a comparison rate value, which can be used to compare the tangetial force production of the SM- and IM-machines to the air gap shear stress of the LSR-motor. The air gap shear stress, the current density and the electrical loading values are collected to table 5.9. with the calculated shear stress values of the five-phase laboratory prototype TF-LSR-motor, and with the calculated shear stress values of the three-phase longitudinal flux laboratory prototype rotating 6/4-SR-motor (T_n = 50 Nm, I_n = 32 A) (Salo, 1996b).

Table 5.9. Comparison of the available air gap shear stress of different electrical machines.

Machine type	J [A/mm^2]	A_e [kA/m]	σ [kN/m^2]
SM	3	30	32
	6.5	65	68
IM	3	25	22.5
	8	65	58.5
3 phase 6/4-SR-motor prototype	7.1	25	24
5 phase TF-LSR prototype	7.6	25	15
	15.2	50	30

Values for the SM- and IM-machines are for the rotating machine in table 5.9. The air gap shear stress values for the linear counterparts might be somewhat lower. TF-LSR-motor needs much more current to produce the same amount of traction force out of the unit area. The location of the winding of the TF-structure increases the required total area covered by the stator.

5.4.6 Conclusions from the FEM-calculations of the static traction force

The finite element method and the scaling law are global, but the results obtained are local. The 2D-FEM-calculation is fast, but the 3D-FEM-calculation provides better force calculation results. This conclusion can be done by studing literature given in chapter 4.1 and figure 5.35.

The continuous traction force curves obtained from static FEM-calculations are always fictious to some extent, because the real motor is never supplied by a constant current from the unaligned mover position to the aligned mover position. Despite of this, the continuous traction force curves can be used to predict the traction force production in any mover position.

Direct scaling of an existing design is one method to design a motor of different size. The designer should notice that scaling can be done also by adding more motors one after the other, if more traction force is reguired. A short example can explain this idea. The new required traction force is assumed to be $4\times F_{t1}$ (F_{t1} is the traction force of the known design). The first case is a direct scaling, in the second case three more motors are added and in the third case the known design is first scaled down in order to obtain $1/4 \times F_{t1}$ and then 15 more new motors are added to which results finally $4\times F_{t1}$ traction force. Table 5.10. describes different masses and lenghts obtained in different cases.

Table 5.10. Comparison of the different scaling cases. F_{t1} is the traction force, M_1 indicates masses and L_1 indicates lenghts of the initial design. F_t is the traction force, M indicates masses and L indicates lenghts of the final design. k is scaling factor, which is unity when motors are added one after other.

Case	F_t	k	L	M
Case 1	$4\times F_{t1}$	2	$2\times L_1$	$8\times M_1$
Case 2	$4\times F_{t1}$	1	$4\times L_1$	$4\times M_1$
Case 3	$16\times\frac{1}{4}\times F_{t1} = 4\times F_{t1}$	$\frac{1}{2}$ 1	$16\times\frac{1}{2}\times L_1 = 8\times L_1$	$16\times\left(\frac{1}{2}\right)^3\times M_1 = 2\times M_1$

As the results in table 5.10. show the designer should always use as small poles as possible, if the stroke length of the mover is not a restriction.

The functions for the minimum and maximum traction forces are global, because the positions and the overlap of the traction force pulses depend on the phase number and the pole width. Definitions are valid when the dimensional design is done by using the equations described in chapter 3.

5.5 The effect of pole width to pole length ratio on traction force production

The pole width / pole height -ratio (*t*/*l* -ratio) has an effect on the traction force production of the LSR-motor due to the stray fluxes and local saturation depth in the overlapping pole edges. The rational portion of the stray flux from the stator pole end to the mover pole end decreases when the *t*/*l* -ratio decreases. This increases the traction force at smaller current values, when the *t*/*l* -ratio decreases. The local saturation in the overlapping pole edges spreads deeper and faster in the poles at small currents when the *t*/*l* -ratio is well below unity. This is the reason why the magnitude of the traction force is smaller at *t*/*l* -ratios less than unity at very high currents. The effect of the *t*/*l* -ratio is illustrated in figure 5.30. calculated by using the 3D-FEM-model of the five-phase basic transversal flux pole pair, when the cross-section of the pole is 10000 mm^2 and the pole material is M2. The mover is in the edge position.

It might be advantageous to have the *t*/*l* -ratio well below unity, because it seems to increase the traction force in the nearly linear region. The *t*/*l* -ratio has to select optimally. Unity *t*/*l* -ratio gives the smallest mover pole of the TF-LSR-motor when the cross-sectional pole face area has desided at first. However, if the *t*/*l* -ratio is below unity the required cross-sectional pole face area can be smaller than with unity *t*/*l* -ratio. This situation happens when the total MMF is below 20 kA in the case of figure 5.30.

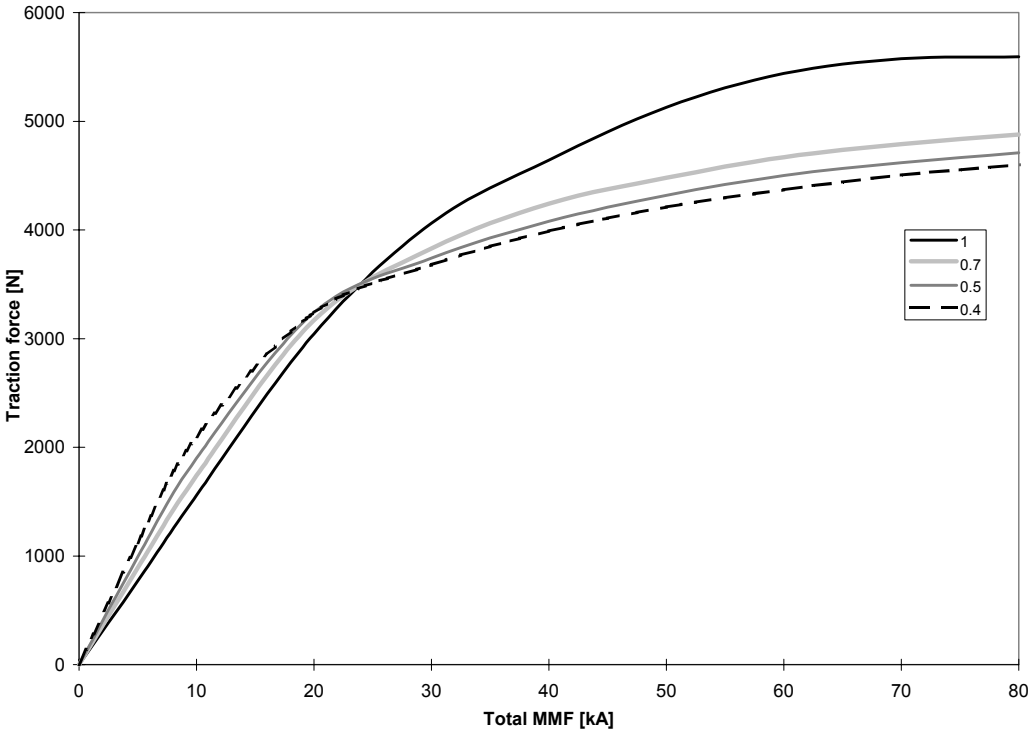

Figure 5.30. The traction force of the five-phase TF-LSR-motor as a function of the *t*/*l* -ratio and the total MMF. The cross-section of the pole is 10000 mm^2 and the pole material is M2. The mover is in the edge position. The labels next to the figure indicate *t*/*l* -ratios 1.0, 0.7, 0.5 and 0.4.

The scaling example given in the previous chapter shows that the poles should be as small as possible. The poles should also be narrow compared to the pole length. Too many small poles may cause problems in arranging the coils. It may be even better to have many teeth in one pole than a greater amount of poles. Gu and Stiebler (1997) studied the torque of a normal rotating three-phase 6/4-SR-motor and a three-phase 84/100 multi-tooth per stator pole SR-motor of the same size. The 84/100-SR-motor has a magnetic gear ratio of 25 (100/4) when compared to the 6/4-SR-motor. Magnetic gearing works like a mechanical gearing. The torque is increased by the same factor by which the speed is decreased. Magnetic gearing gives quite good results when iron is not heavily saturated and the stray flux is small. The authors analysed a 84/100-SR-motor with the specific torque per stator volume 2.8 times that of a 6/4-SR-motor. The specific torque per rotor volume of the 84/100-SR-motor was 0.7 times that of the specific torque of the 6/4-SR-motor. The authors concluded that with high magnetic gear ratios (very many poles with low speed), *"a higher specific torque at lower copper mass can be achieved"*.

5.6 Design procedure of a TF-LSR-motor

The thesis gives some methods and guidelines for the designing of linear movement SR-motors. The basic dimensioning can be done by using the developed dimensioning equations when the cross-sectional area of the pole, the total MMF, the current density and the required traction force are known. The traction force is a function of the cross-sectional area of the pole and the total MMF of the stator pole. The required cross-sectional area of the pole and the total current can be calculated by performing first a 2D-FEM-calculation for the initial design and then a 3D-FEM-calculation for the final design. The flowchart of the design process is illustrated in figure 5.31.

The number of the coil turns N is selected by using dynamical simulation. The required boundary conditions are the maximum speed of the mover, the maximum acceleration and deceleration, and the required starting traction force. An initial value of the number of turns can be derived from the time interval Δt required for the current to rise to the value that gives the maximum traction force at the edge position while the mover travels with speed v from an unaligned position to an edge position. The product of the flux linkage and the current at the edge position is the sum of the magnetic field energy W_{f} and the magnetic co-energy W_{co}. The product can be calculated with any total MMF Θ. If the intermediate circuit voltage is U_{d} the initial N can be defined to be

$$N = \frac{U_{\mathrm{d}}\, x_{\mathrm{ep}}\, \Theta}{v\,(W_{\mathrm{f}}(x_{\mathrm{ep}}, \Theta) + W_{\mathrm{co}}(x_{\mathrm{ep}}, \Theta))}, \tag{5.31}$$

where the edge position of the mover is

$$x_{\mathrm{ep}} = \frac{\tau_{\mathrm{m}}}{2m}. \tag{5.32}$$

If the iron core is made of thin iron laminations the simulation model presented in chapter 4.2.1 may be applied to find the best value for the number of turns. The simulation model presented in chapter 4.2.2 should be used when losses are remarkable.

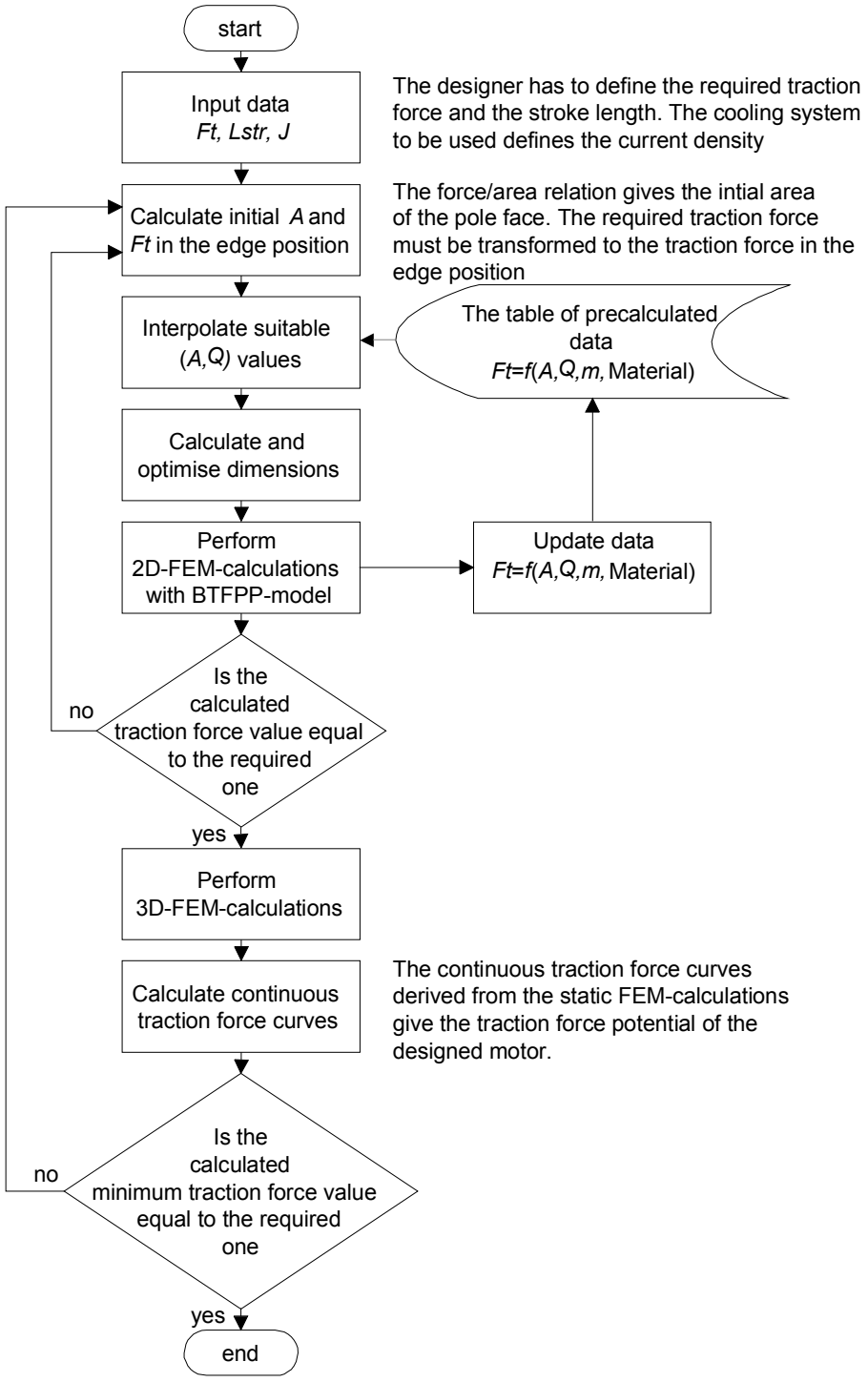

Figure 5.31. Flowchart of the design process of a TF-LSR-motor to produce the required static traction force.

5.7 The laboratory prototype of the basic pole pair of TF-LSR-motor

To validate the calculation methods developed a five phase one sided transversal flux basic pole pair laboratory prototype was constructed and measured. Solid steel is chosen for simplicity and ease of manufacture. Iron losses limit the solid steel core constructions to low speeds. The main dimensions are the same as for the previous rotating 6/4-SR-motor (Salo, 1996b) and the prototype is not optimised at all. The height of the stator and mover pole are for a 100 mm pole length from the first prototype, thus there is too much iron in the poles in the final design. The winding window dimensions are chosen so that there is enough space for the main coil and for a measuration coil. The prototype is illustrated in figures 5.32., 5.33. showing the basic construction and photographs of the laboratory prototype. Final dimensions of laboratory prototype are shown in table 5.11. Definitions of the dimensions are described in chapter 3.1.

Table 5.11. The dimensions of the laboratory prototype.

Dimension		Magnitude
Pole face area	A [mm^2]	1500
Total MMF	A_t [A]	3000
Number of turns	N [turns]	1000
Current density	J [A/mm^2]	7.6
Phase number	m	5
Length of the air gap	δ [mm]	0.5
Pole width	t [mm]	30
Pole length	l [mm]	50
Stator pole heigth	h_s [mm]	135
Mover pole heigth	h_m [mm]	100
Depth of the winding window	d_w [mm]	35
Length of the winding window	l_w [mm]	35
Total length of the stator pole	l_p [mm]	135
Stator pole number	p_s	1
Mover pole number	p_m	2
Mass of the stator pole	M_{sp} [kg]	4
Mass of the copper	M_{cu} [kg]	1
Mass of the mover pole	M_{mp} [kg]	3.2
Total mass of the mover	M_m [kg]	6.4

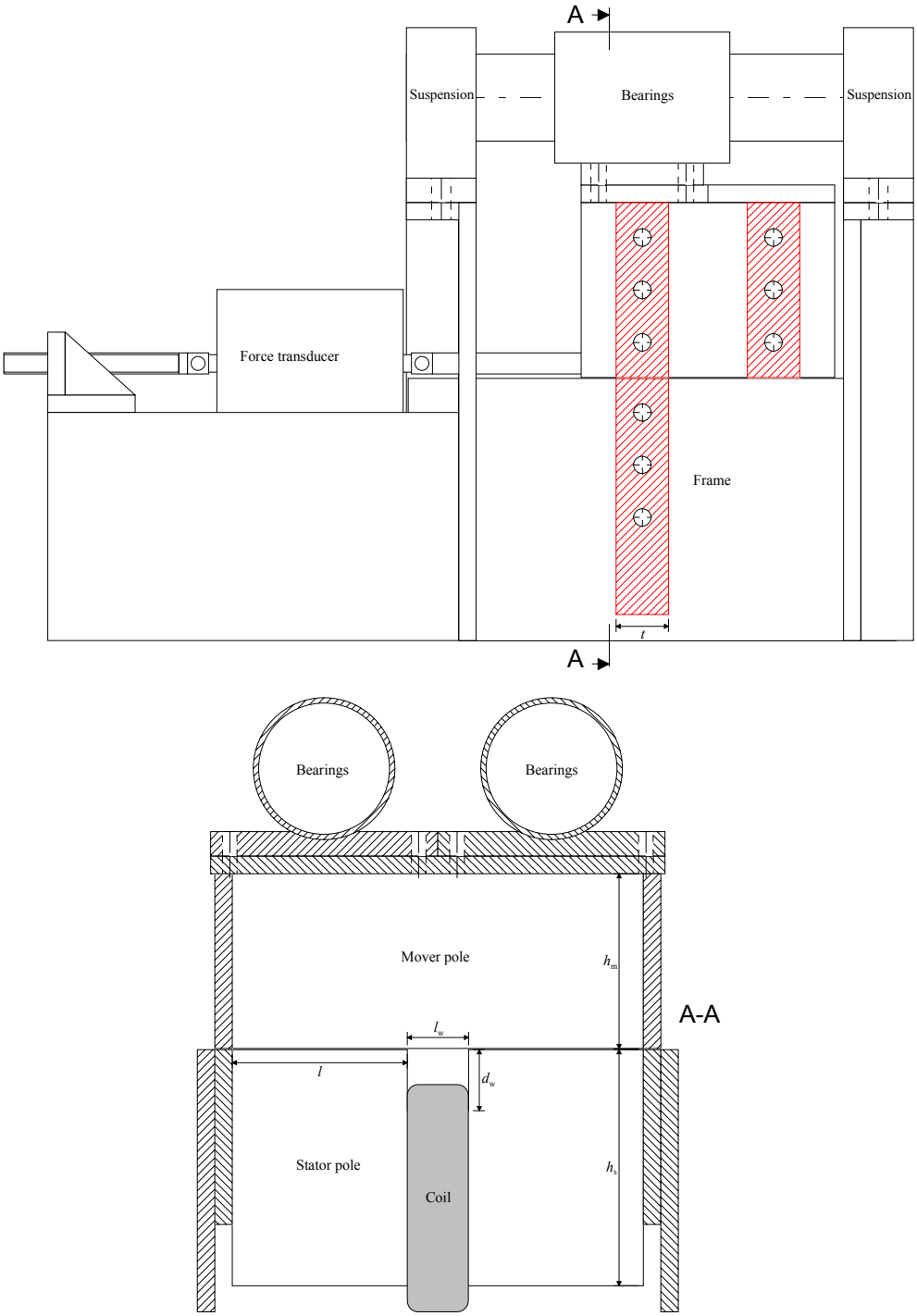

Figure 5.32. The laboratory prototype of the basic transversal flux pole pair. The design is for a five-phase one-sided machine. Upper picture shows the basic construction of the prototype with hatched poles. Lower picture shows cut A-A from upper picture.

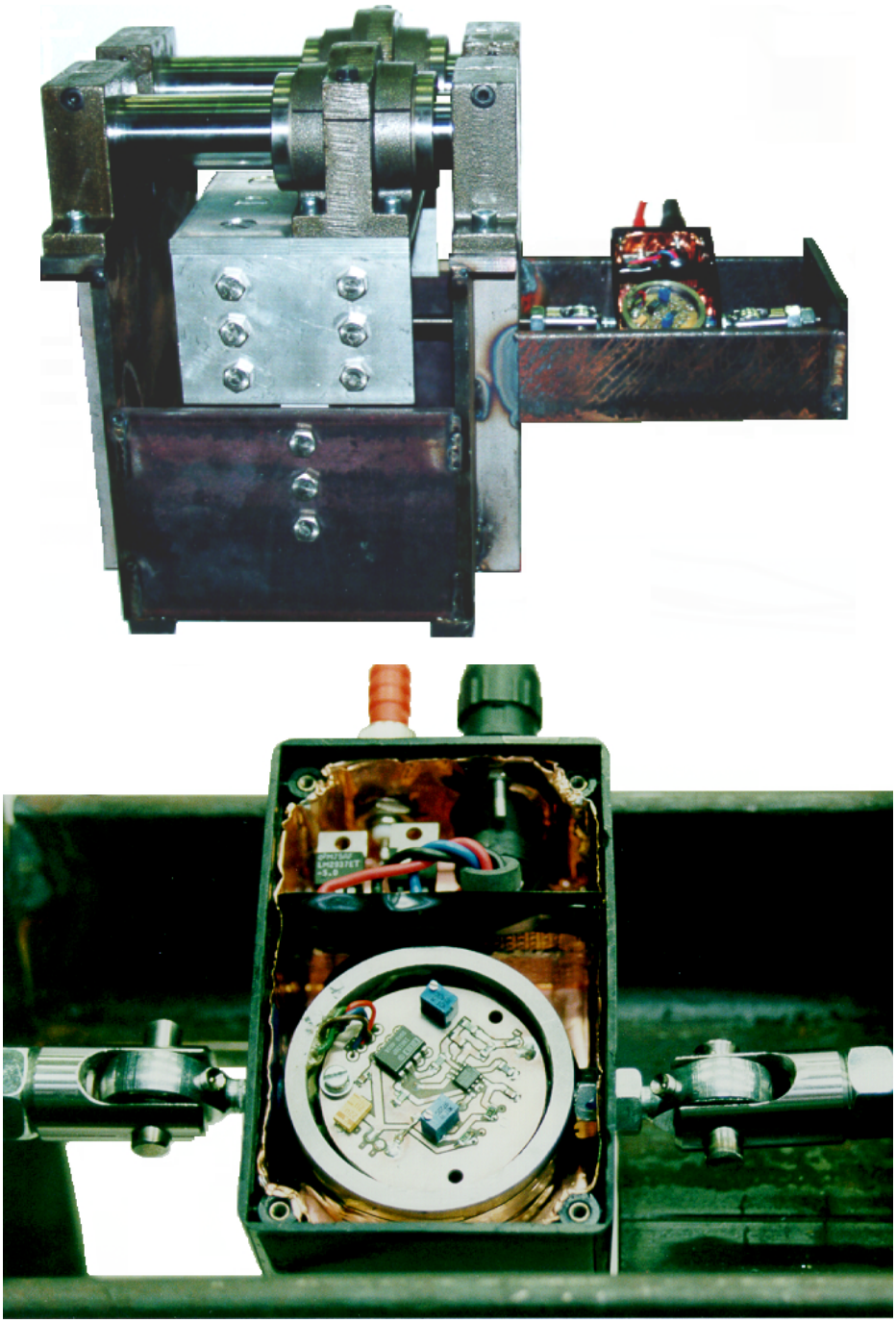

Figure 5.33. The photographs of the laboratory prototype which consists of the one-sided transversal flux basic pole pair (upper picture) and the force transducer (lower picture). Note the ball bearings used to attach transduer to the mover. They are used to avoid bending which causes errors to traction force measurement.

The material of the iron circuit of the laboratory prototype is solid steel that has very little amount of blend components. The magnetic (B,H)-curve of the material are close to that of pure iron. The material is called M1 in this study. The supporting frame should have been aluminium, but because of manufacturing problems it is reblaced by normal construction steel. The support and fastening parts of the mover are aluminium. All the bolts are stainless steel. The bearing system used is of the ball bushing type.

The main coil with 1000 turns is wound from 0.767 mm diameter round enamelled copper wire. The measuration coil is wound on the main coil in the same direction. The measuration coil has also 1000 turns and its wire diameter is 0.25 mm.

Figure 5.33. shows a photograph of the force transducer. The transducer is used in the traction force measurements. It is of the strain gauge type and the amplifier is built inside an iron ring where the strain gauges are glued on (Kuisma, 1997). The dynamic range of force measurement is 400 N and the resolution is 1 N.

The power switches form one leg of a switched reluctance motor inverter shown in figure 2.1. The power stage is controlled by a digital signal generator. The DC-values are measured by digital true RMS multimeters. The transient signals are measured by using a four channel digital oscilloscope.

5.7.1 The measurement of static traction force and static FEM-calculation results of the prototype

The static traction force measurement is done by using controlled DC-voltage and true RMS multimeters. The current and voltage of the main coil is measured. The traction force is measured with the force transducer and the value is obtained as voltage. The mover position is measured with a calliper rule. The static traction force measurement assembly is shown in figure 5.34.

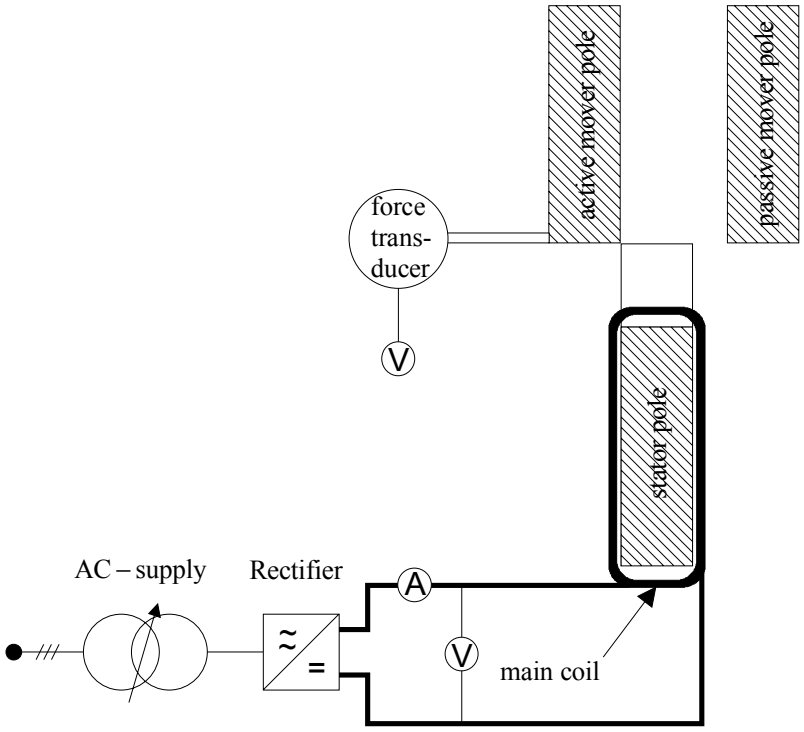

Figure 5.34. The static traction force measurement assembly. The current and voltage of the main coil is measured with true RMS multimeters. The traction force transducer gives a voltage which is measured with true RMS multimeter. Three phase voltage is controlled by a variable transformer. A DC-voltage is then got by rectifiering and smoothing an AC-voltage.

The static traction force is measured by fixing the mover in a certain position and by setting the direct current to be 0.6, 0.9, 1.2, 1.5, 1.8, 2.0, 2.2, 2.4, 2.7, 3.0 and 6.0 A. The upward measurement is done by setting the current to be first 0.6 A and then the other current points one by one increasing the current without letting the current decrease in middle. The downward measurement is done by setting the current to be first 6.0 A and then the other smaller current points one by one decreasing the current without letting the current increase in the middle. The upward and downward measurements were repeated four times at each mover position. The lower curve in figure 5.35. is measured by using the upward technique and the upper curve was measured by using the downward technique. The curve between upper and lower curves in figure 5.35. is the mean curve of the upper and the lower curve. The mover is in the edge position.

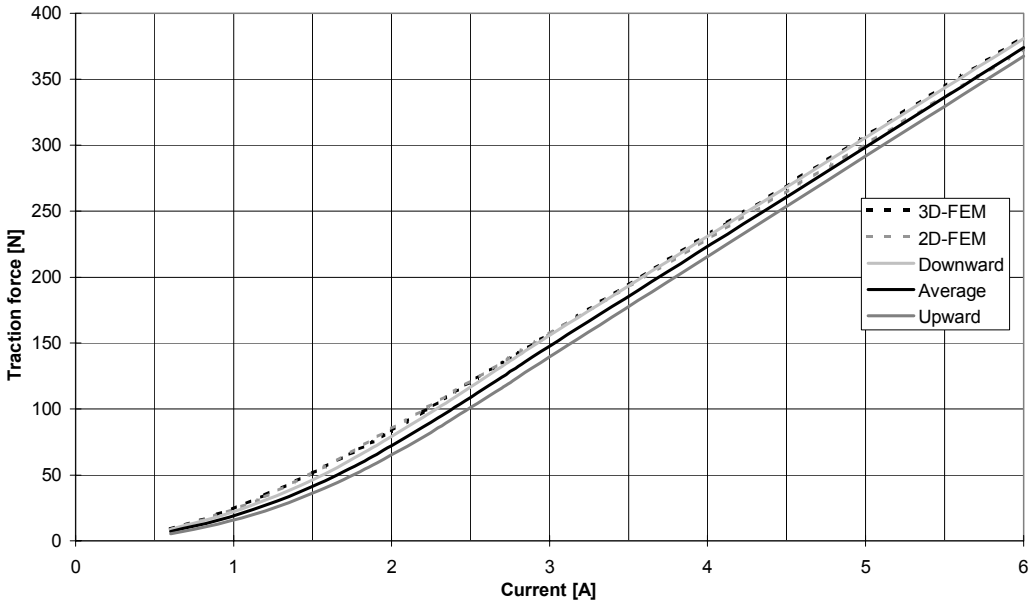

Figure 5.35. The static force of the laboratory prototype as a function of the current, when the mover is fixed in the edge position. The difference between downward and upward curves is caused by magnetic hysteresis.

The total amount of points in the static fixed mover force measurement is 1408 at 16 different mover positions. The static traction force as a function of the mover position and current is illustrated in figure 5.36. with both the 2D-FEM and 3D-FEM traction force calculation results. The normal force of the prototype calculated by means of 3D-FEM is illustrated in figure 5.37. as a function of the position of the mover and the current.

The standard deviation of upward measurement and downward measurement scaled to the mean value of the measured traction force as function of current and the position of mover are illustrated in figures 5.38. and 5.39. respectively. The relative error of the traction force of 3D-FEM-calculation and 2D-FEM-calculation to measured traction force as function of mover position is illustrated in 5.40. and 5.41. respectively.

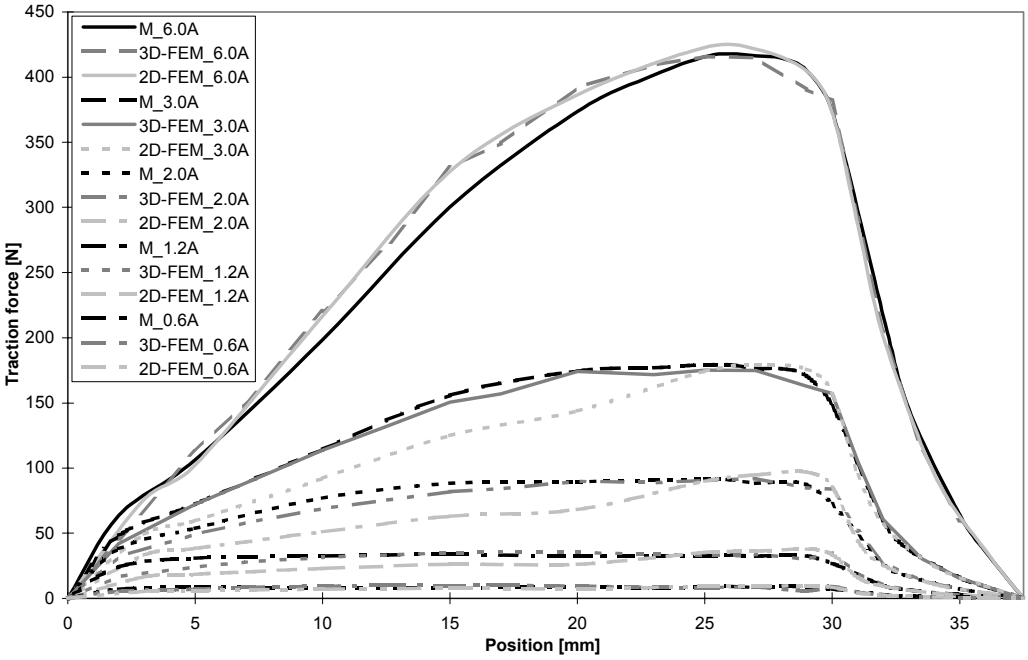

Figure 5.36. Static traction force of the prototype as a function of current and the position of the mover. The labels next to the figure indicate the measured value as M, the 2D-FEM-calculated value as 2D-FEM, the 3D-FEM-calculated value as 3D-FEM and corresponding current value 0.6, 1.2, 2.0, 3.0 and 6.0 A. The aligned mover position is equal to 0 mm and the unaligned mover position is equal to 37.5 mm. The edge position is equal to 30 mm.

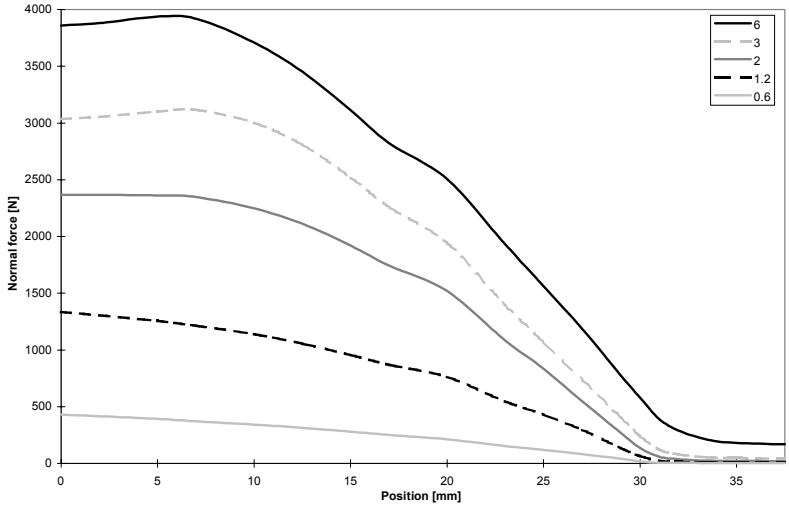

Figure 5.37. The normal force of the prototype calculated by means of 3D-FEM as a function of the position of the mover and the current. The aligned mover position is equal to 0 mm and the unaligned mover position is equal to 37.5 mm. The edge position is equal to 30 mm.

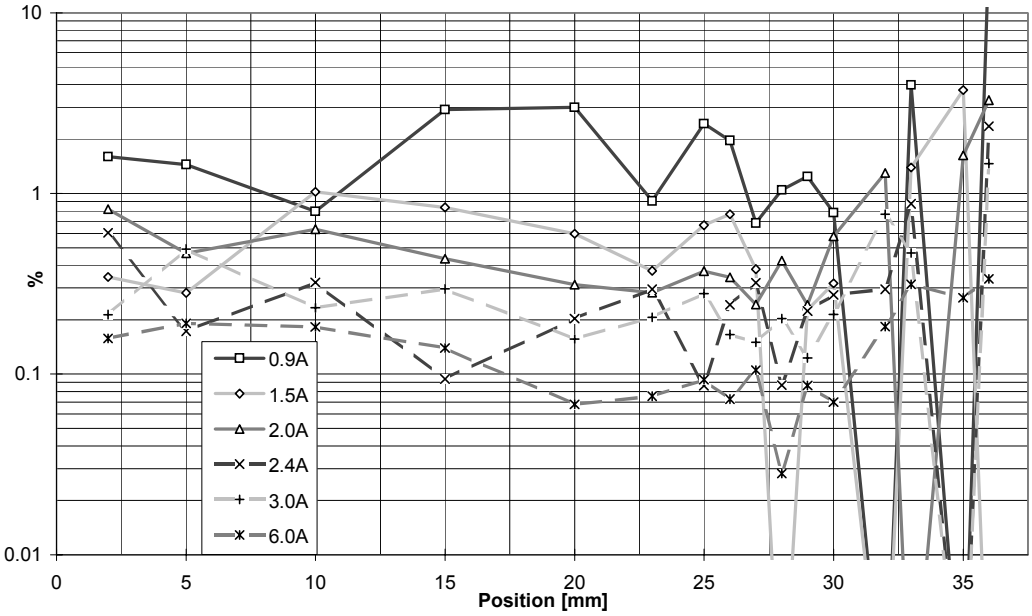

Figure 5.38. The standard deviation of upward measurement scaled to the mean value of the measured traction forces as a function of the current and the position of the mover. The labels next to the picture indicate the current value used.

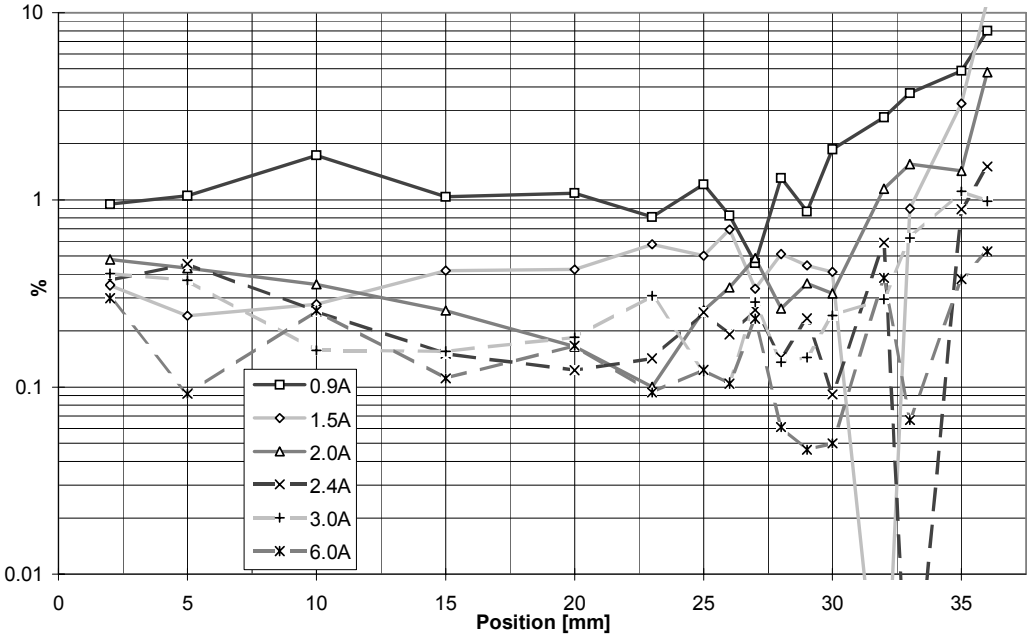

Figure 5.39. The standard deviation of downward measurement scaled to the mean value of the measured traction forces as a function of the current and the position of the mover. The labels next to the picture indicate the current value used.

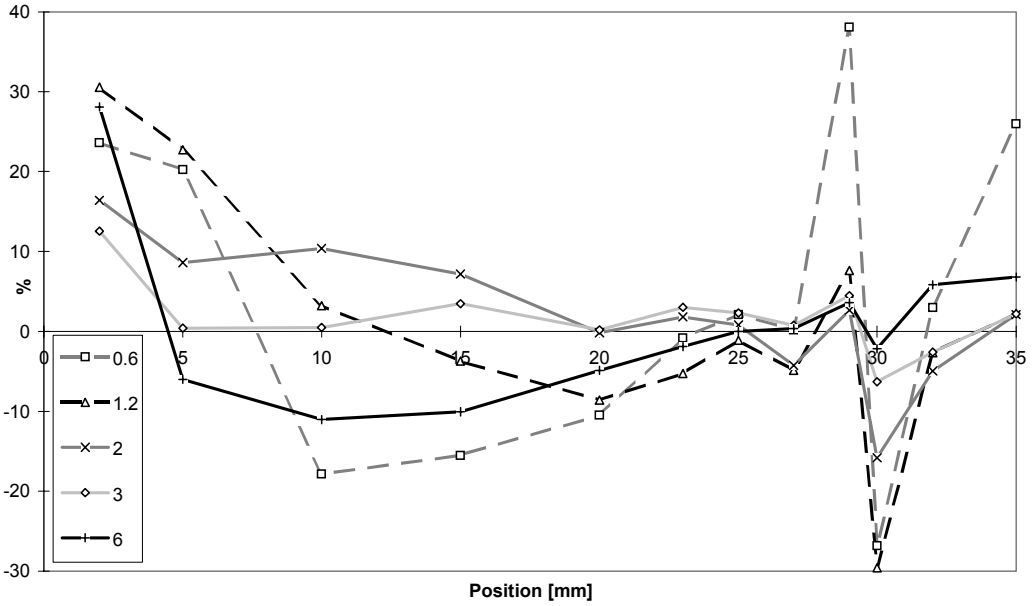

Figure 5.40. The relative error of the traction force of 3D-FEM-calculation compared to the measured values as a function of the mover position. The labels next to the figure indicate the current value used. The aligned mover position is equal to 0 mm and the unaligned mover position is equal to 37.5 mm. The edge position is equal to 30 mm.

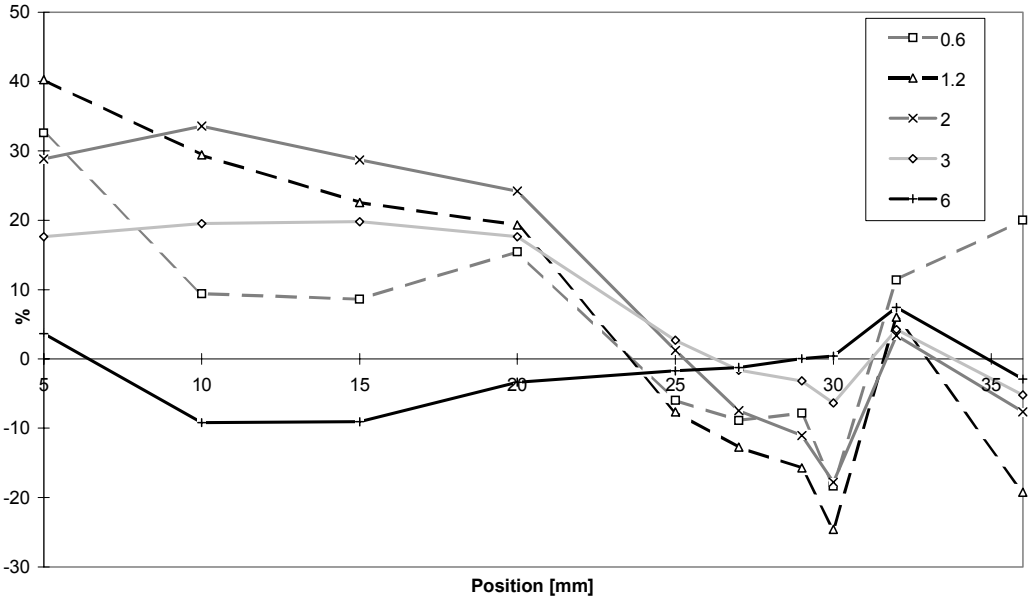

Figure 5.41. The relative error of the traction force of 2D-FEM-calculation compared to the measured values as a function of the mover position. The labels next to the figure indicate the current value used.

The laboratory prototype is only a one-pole pair system, thus no stray flux between is occuring the different phases. Stray flux between the frame and the pole pair is existing, but difficult to estimate. The 3D-FEM-model of the prototype is also only a one-pole pair system. It is possible to model also other phases of the motor with 3D-FEM, but the result is a too extensive and unaccurate 3D-FEM-model. The stray flux through the winding window and the stray flux in the coil region can be estimated with the 3D-FEM-analysis. The stray flux is also affected by the position of the coil. The used half-model of the prototype with horizontal coil is illustrated in figure 5.42. The stray flux through the winding window is calculated by taking the z-component of the flux density on the symmetry plane. The location of the vertical coil can be seen in figure 2.7.

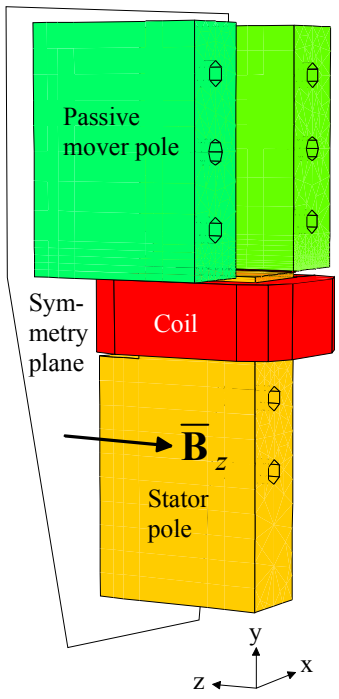

Figure 5.42. The half-model of the prototype with horizontal coil showing also the symmetry plane. The mover is in the edge position.

The 3D-FEM-analysis of the same half-model of the prototype is done with both the vertical and horizontal coil. The z-component of the flux density on the symmetry plane with both the vertical and horizontal coil is illustrated as a regional plot in figure 5.43.

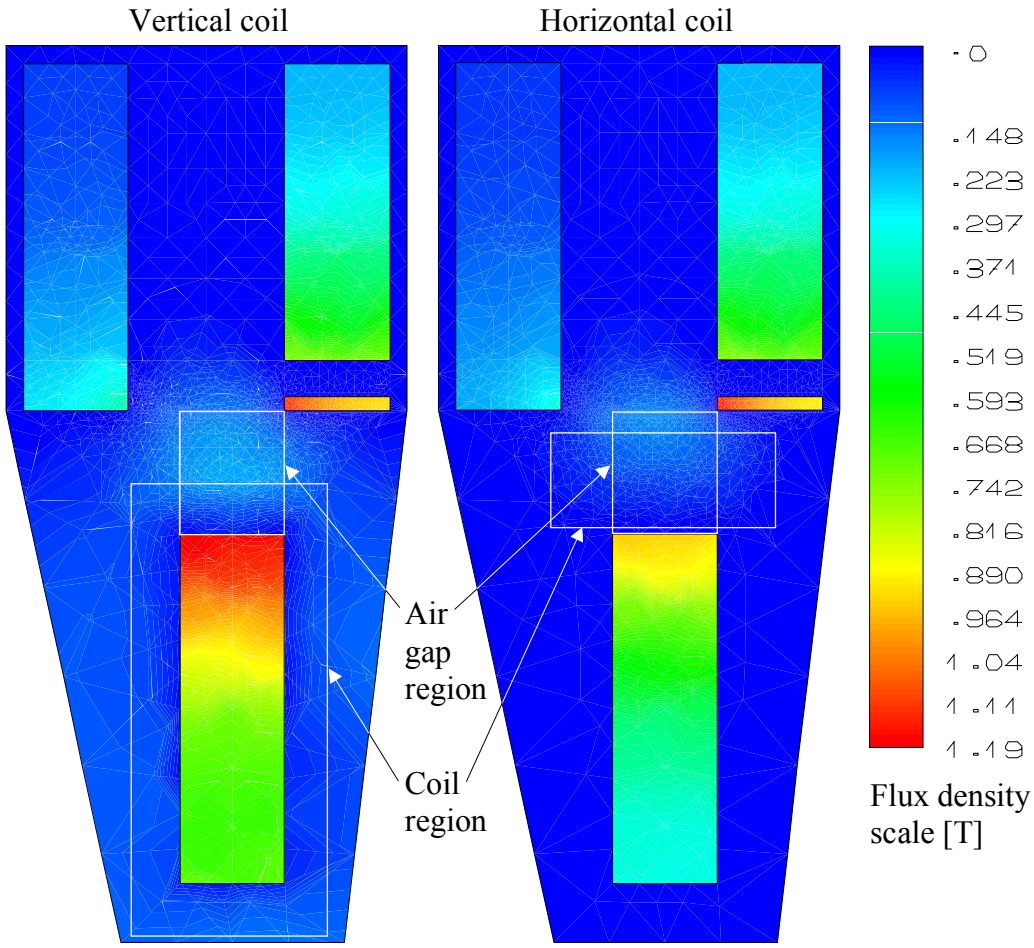

Figure 5.43. The regional plot (gray scale indicates flux density in Teslas) of the z-component of the flux density on the symmetry plane. The left picture is of the vertical coil and the right picture is of the horizontal coil. The current is 6 A. The movers are in the edge position. The air gap and coil regions are also shown. Note the flux density difference in the air gap regions. Holes in the bottom ends of the right mover poles are for the rod connecting the mover and the force transducer in the real prototype.

The stray flux through the winding window is larger in the case of the vertical coil than that in the case of the horizontal coil. This can be seen in figure 5.43. which compares the flux densities in the air gap regions. Some stray flux is appearing also in the vertical coil region. The ratio of the stray flux to the main flux going through the symmetry plane (figure 5.42.) is described in table 5.12. as a function of the current.

Table 5.12. The stray flux as a function of the current in the case of the vertical coil and in the case of the horizontal coil. The stray flux is the relational portion of the main flux going through the symmetry plane in figure 5.42.

Current [A]	Stray flux in the case of the vertical coil [%]	Stray flux in the case of the horizontal coil [%]
2	24	11
6	26	12

The results in table 5.12. indicate the weakness of the magnetic design of the prototype in terms of stray flux. It should be emphasized that the laboratory prototype is not at all optimised and its purpose is only to validate some of the design methods.

The errors in the static traction force measurement are mainly resulting from the mechanical friction, the force transducer range and the temperature sensitivity. The friction of the mechanic bearing system is worse than expected due to the one-sided structure of the prototype which has a severe normal force problem as illustrated in figure 5.37. Due to the normal force the effect of friction is gained when the overlap is increased. The inversion point in the measured traction force in the position of 5 mm can be seen in figure 5.36. The shapes of the measured traction force curves are bulged between positions 0 and 5 mm, while the traction force curves calculated by means of 3D-FEM are smooth in the same area. This bulged shape is caused by effects combining the friction and the normal force. The force transducer is sensitive to temperature change in the transducer. This causes drift in the zero point of the transducer. This effect has been observed when the measurement of the same position has been repeated the next day whit out adjusting the zero point position meanwhile. The measurements of static traction force points out, that the laboratory prototype should be at least two-sided structure to have balanced normal forces.

The error in the 3D-FEM-calculation of the traction force is mainly resulting from inaccurate material modelling and discretisation errors in the finite element mesh. The error in the 2D-FEM-calculation can be explained for the same reasons and by the stray flux that is not possible

to calculate with 2D-FEM-calculation. The flux plot of the 2D-BTFPP-model (see figure 5.2.) with the dimensions of the prototype is illustrated in figure 5.44. The stray flux of the model is about 10% in the case of 6 A current.

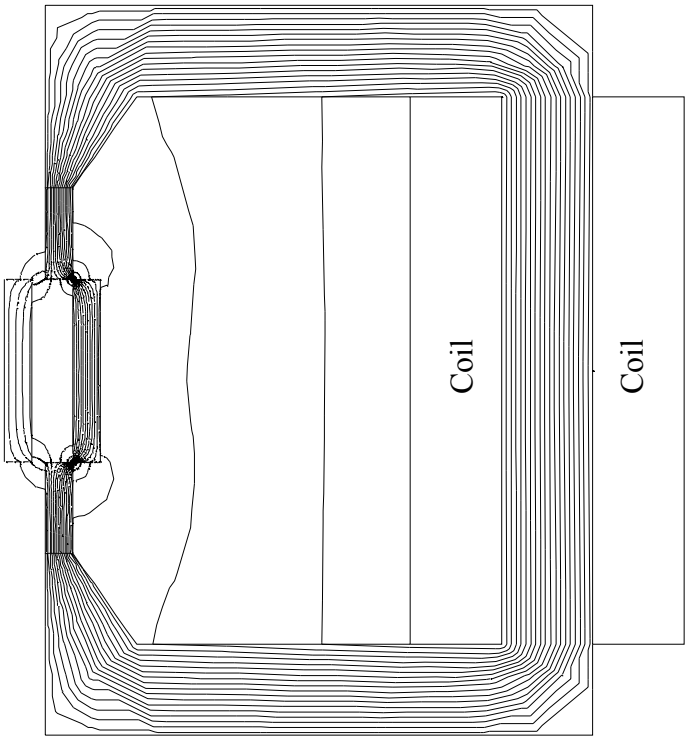

Figure 5.44. The flux plot of the 2D-FEM-model of the prototype. The current is 6 A and the mover is in the edge position. Note two flux lines going through air compared to the total 20 flux lines. That stray flux is caused by model not beacause of the prototype itself.

The stray flux is small when there is a vertical air gap between the stator and the mover poles, but when the stator and the mover poles are well overlapped, the stray flux has a remarkable effect on the traction force calculation. This effect can be seen in figures 5.36. and 5.40. where the error between the measured traction force and the 2D-FEM-calculated traction force increases, when the overlap increases. Some of the errors between the measured traction force and the FEM-calculated traction forces are caused due to above described measurement errors with positions from 0 to 5 mm.

Some performance values of a one-sided five phase TF-LSR-motor are calculated from the values of the prototype. Table 5.13. describes ideal static values when iron losses and friction are not taken into account.

Table 5.13. Ideal static performance values of a five phase one-sided TF-LSR-motor calculated from the prototype values. Iron losses and friction are not taken into account.

Dimension		Magnitude
Stator pole number		5
Mover pole numeber		4
Electrical length and stroke length	[mm]	300
Phase number		5
RMS current of the motor	[A]	7.5
DC-voltage	[V]	540
Phase resistance	[Ω]	20
Iron and copper mass	[kg]	38
Maximum traction force	[N]	304
Average traction force	[N]	287
Air gap shear stress	[kN/m^2]	15
Traction force per iron and copper mass	[N/kg]	7.6
Motor input power at standstill	[W]	1125
Traction force per power at standstill	[N/W]	1.6
Motor input power with maximum speed	[W]	4050
Traction force per power with maximum speed	[N/W]	0.07
Maximum speed	[m/s]	10
Effciency with maximum speed	[%]	72

5.7.2 The transient measurement and FEM-calculations of the mover fixed in the edge position

The transient measurement of the mover fixed in the edge position is done by supplying the coil by a square wave voltage and by measuring the induced voltage in the measuration coil, the current in the main coil, the supply voltage and the traction force. The measurement assembly is shown in figure 5.45.

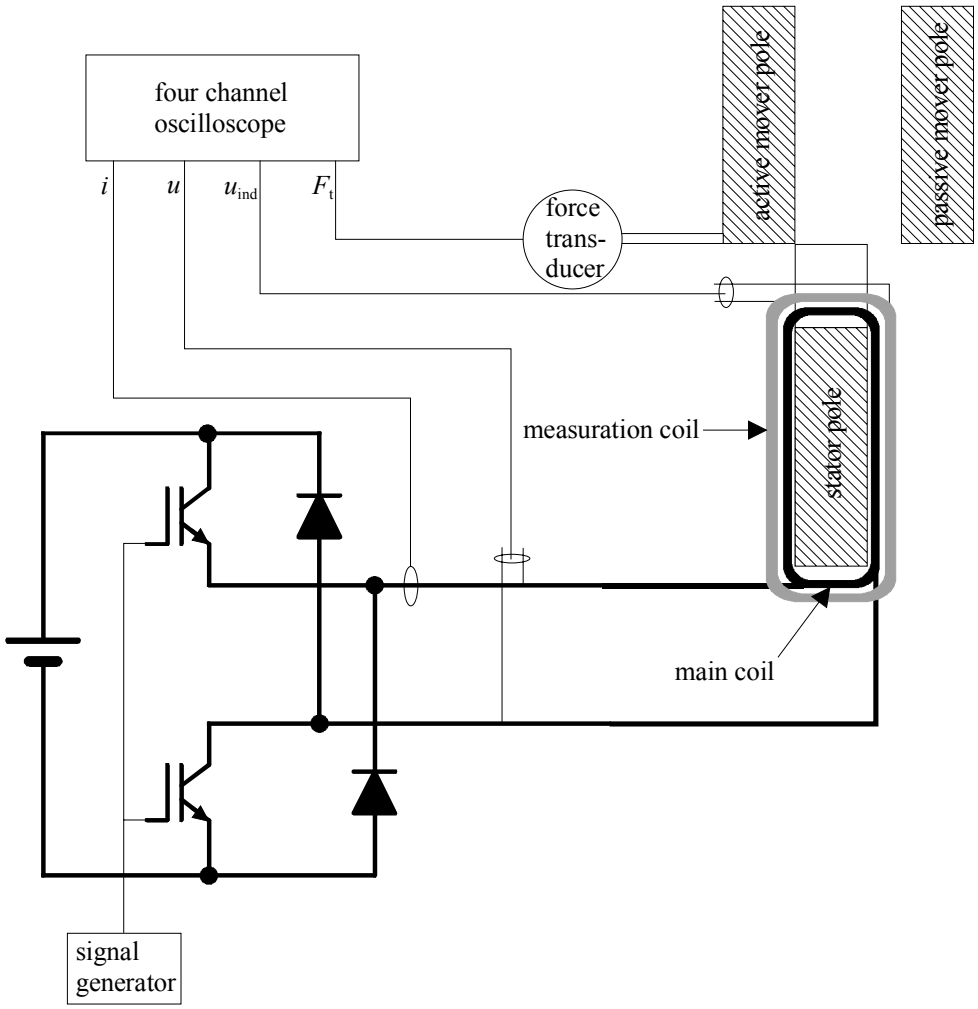

Figure 5.45. The transient measurement assembly.

The supply frequency is as low as it is possible to adjust the duty cycle of the digital signal generator to let all current die before the next cycle. The lowest possible frequency is 2 Hz due to disturbances when the maximum current is about 3 A. The transient test is done to find out how well the transient 3D-FEM-calculation can predict the traction force production. The low frequency is selected in order to keep the transient results near the static traction force production results. The supply voltage, the induced voltage and the current are illustrated in figure 5.46.

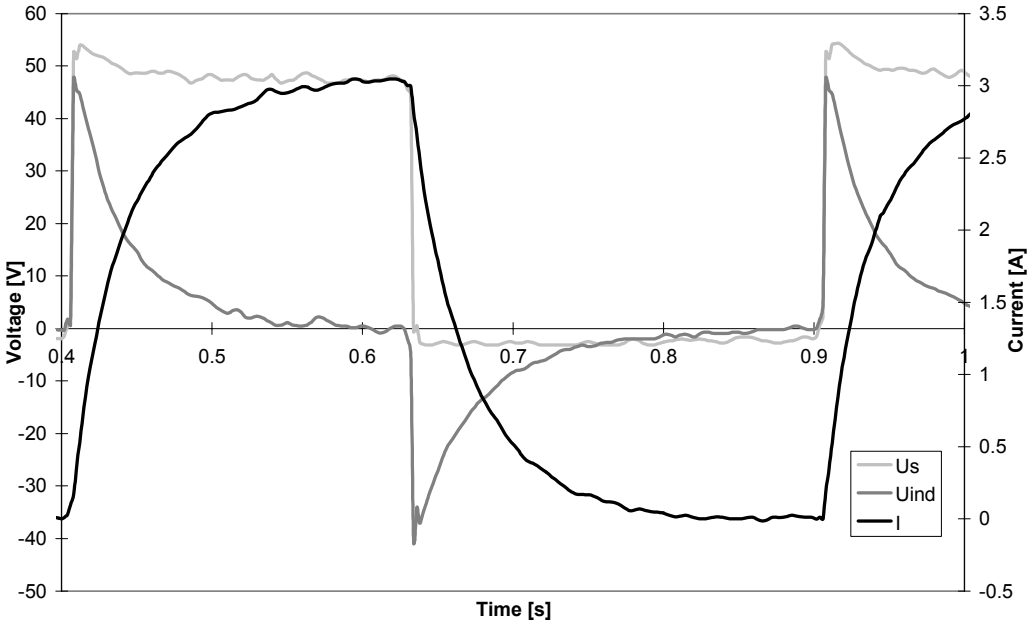

Figure 5.46. The supply voltage, the induced voltage and the current when the frequency is 2 Hz. The mover is in the edge position. The labels next to the picture indicate the supply voltage as Us, the induced voltage as Uind and the current as I. Each curve has 1024 points and the lenght of record is 0.6 s. There may appear fast transients that are not visible, but the period of the measured curves is 100000 times the period of the possible unvisible transient.

The measured and the FEM-calculated traction forces as a function of current are illustrated in figure 5.47. when the mover is in the edge position. The measured transient traction force increases a little bit slower than the measured static upward traction force. The measured traction force stays almost in its peak value after the peak value of the current is reached and the current decreases rapidly. After that, the measured traction force decreases slower than the measured static downward traction force. The behaviour of the measured transient traction force in contrast to the measured upward and downward static traction force indicates some mechanical

friction problems and mostly the eddy current power losses of the solid iron magnetic circuit. The magnetic hysteresis is included in the measurements. When the current changes rapidly it takes time to wait all the eddy current effects to vanish and let the main flux to build up and down. The strongest effect of the eddy currents can be seen in inversion points of the current: the zero point of current and the peak current. In these points the current changes the most fastest and at the same time the traction force changes nearly at all.

The transient 3D-FEM-calculation is used to predict the traction force in a dynamical situation. The magnetic material modelling does not take into account the hysteresis and the presence of magnetic domains. The classical eddy current governed by Ampere's law is computed by the means of the transient-FEM-calculation. It can be seen in figure 5.47. that the transient-3D-FEM-calculation can predict in some ways the traction force in a dynamical situation. The largest error source in the transient-3D-FEM-calculations is the material modelling. However, figure 5.47. shows that the 3D-FEM-calculation can be used to some extent to predict the dynamical traction force production.

The current measured in the transient measurement is the current supplied to the coil as it can be seen in figure 5.45. All that power carried with the supply voltage and the current is not converted to mechanical power (see figure 4.6.). The transient-3D-FEM-calculations are done in two way. The first transient-3D-FEM-calculation is done by using the measured current pulse of figure 5.46. In figure 5.47. the first transient-3D-FEM-calculation is indicated as (1) and the second transient-3D-FEM-calculation is indicated as (2).

The second transient-3D-FEM-calculation is done by using the current pulse composed of the measured traction force as a function of the current pulse in figure 5.46. and of the static traction forces in figure 5.35. Current composition is achieved in the following way: the currents are chosen from figure 5.35. as a function of the traction forces measured in the transient measurement. The currents are chosen from the upward curve in the figure 5.35. when the measured transient traction forces are increasing, and the currents are chosen from the downward curve in figure 5.35. when the measured transient traction forces are decreasing. The currents in figure 5.35. are the currents required in order to produce in an ideal way the corresponding static traction force which includes the hysteresis effect. When the current pulse used in the second tran-

sient-3D-FEM-calculation is composed in that way, the hysteresis effect is included into transient-3D-FEM-calculation.

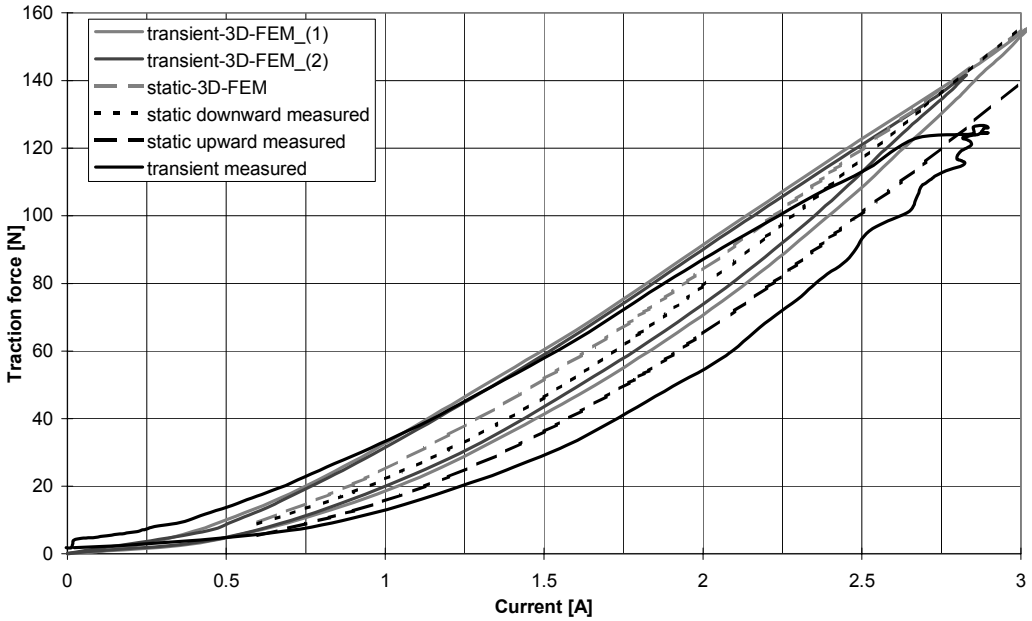

Figure 5.47. Traction force as a function of current and frequency. The mover is in the edge position. Static measurements are also shown as an ideal traction force production. Transient 3D-FEM-calculations are done with two methods. Measured transient current is used as a source current in the first method marked as (1) in figure. In second method, marked as (2) in figure, the source current is composed by combining mesured transient traction forces and static currents. The measured transient force loop is wider than the measured static loop. The static loop fits inside the transient loop like it should be. Transient 3D-FEM-calculation results are little bit too high compared to measured static traction forces.

The difference of the areas of the loops of the first and the second transient-3D-FEM-calculations indicates the energy of the hysteresis loss. The area of the loop of the second transient-3D-FEM-calculation indicates the energy of the eddy currents. The area of the measured transient flux linkage in figure 5.48. counts all the dynamical loss components. The measured flux linkage is obtained by integrating the measured induced voltage in the measuration coil. The area is a little bit larger than the area of the loops of transient-FEM-calculations. The position of the measured transient flux linkage loop is different than that of the FEM-calculated transient flux linkage loops. The measured current includes all the loss components, since the FEM-calculations are done with in a way ideal current pulses. The most important error of the tran-

sient flux linkage measurement is caused by the measuration coil. The measuration coil is wound on the main coil. When the current changes rapidly, the voltage induced into the measuration coil is caused by the change of the main flux and the stray flux of the main coil. That part of the induced voltage due to the change of the stray flux of the main coil is impossible to extract by the help of the measurement assembly shown in figure 5.45. The error is quite evident because the measured and the FEM-calculated traction forces are much closer to each other (figure 5.47.) than the measured and the FEM-calculated flux linkages (the figure 5.48.).

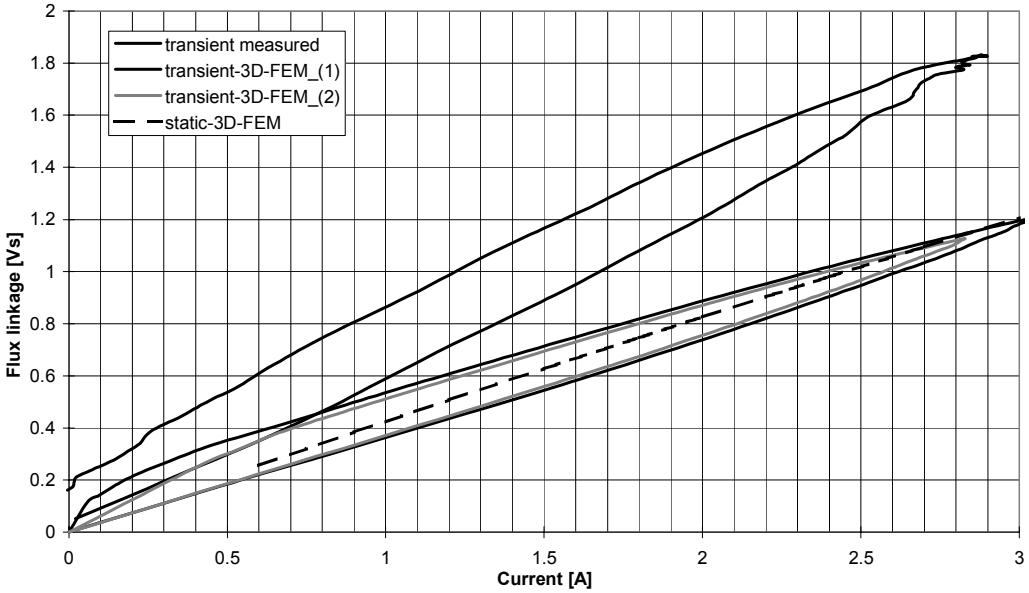

Figure 5.48. Flux linkage as a function of current and frequency. The mover is in the edge position. Flux linkages of static- and transient-3D-FEM-calculation show quite good agreement. The loop of transient-FEM-calculation are caused by computed eddy currents. The position of the measured flux linkage loop indicate unsuccessful transient measurements. The computed and measured loops should be closer to each other as are loops in figure 5.47.

5.7.3 Cooling of the prototype

The required amount of force or torque and the cooling system used determines the size of the motor. There is a lot of experimental knowledge about cooling of rotating electrical motors. Such a knowledge does not exist for LSR-motors. The coil of the LSR-motor is a pole winding. It can be compared to the field windings of the rotating electrical motors. The coil of the labo-

ratory prototype is an unhomogeneous mixture of copper wire, insulating varnish, slot insulator and insulator tape. The coil has a tight contact to the stator pole iron in the corners of the coil. In the middle of the coil along the stator iron length the contact between the coil and the iron is loose. The shape of the coil is unsymmetric. The thickness of the layer of insulations between the air and copper varies. The coil and the heat transfer from the coil to the air is a real three dimensional case. The heat resistances over different insulation layers and contact heat resistances are unknown. Because of these reasons it is quite hard to find an analytical expression for the heat transfer from the copper to the air in the case of the coil of the laboratory prototype.

Some simple measurements were done to find out the current density which can be used with natural air cooling and with forced air cooling. Because there was no thermocouple left inside the coil when the coil was wound, the measurement are carried out as resistance tests. The most difficult task of the driving of the LSR-motor is to keep the mover in standstill with the maximum current when cooling is considered. That case can be simulated by using DC-current in the coil when the mover is fixed. The maximum average temperature of the coil T_c is chosen to be about 140°C which fits in with the IEC 34-1 standard class of 155°C given for the used insulating varnish. The average temperature of the coil is found from the equation

$$T_c = T_1 + \frac{R - R_1}{\alpha \cdot R_1}, \tag{5.33}$$

where T_1 is 20°C, R_1 is the resistance of the coil when the temperature of the coil is T_1. R_1 is 13.4 Ω. α is the temperature coefficient of the resistance. α is 0.00381 1/°C for copper in 20°C. R is the resistance of the coil when the average temperature of the coil is T_c. R is found by measuring the voltage and current of the coil when the stabile working point is reached and the temperature of the coil is not changing any more.

The first test was done by using natural air cooling. The precalculated current density is adjusted to be in the coil. Then measurements were done after the voltage of the coil was constant. After that, the first axial fan was installed directly below the coil. The current density was kept constant and after the voltage was constant the measurement was carried out. Then the current density was increased so that the resistance was the same as in the first test.

The second axial fan was installed parallel to the first axial fan and the current density is adjusted to be the same as in the first test. Again the measurements were done after the voltage of the coil was constant. Then the current density was increased so that the resistance was the same as in the first test. The fan type is an axial fan Semikron SKF 3-230-01 with the maximum air flow of 190 m3/h (fan supply 230 V(a.c.), 50 Hz). The results of the tests are shown in table 5.14. The ambient temperature in all tests was 20°C.

Table 5.14. The measurements of the cooling of the coil. P_c is the power dissipated in the coil.

	Natural cooling	Forced cooling 1 fan		Forced cooling 2 fans	
J [A/mm^2]	5.1	5.1	6.2	5.1	6.4
T_c [°C]	137.3	93.1	137.3	87.2	137.3
P_c [W]	78.7	69.6	118.6	68.3	124.5

The current density of natural cooling fits into the range of the current density as given for natural cooling in table 3.1. The axial fan used was a small one and that is why the current density was quite low for the through cooled structure. The adding of the second fan increased the current density only 0.2 A/mm^2. This result indicates that the air speed along the coil side is increased only a little when the second fan was added parallel to the first one.

6 CONCLUSIONS

The rapid development in microelectronics and information technology makes it now possible to use simpler mechanical structures in electric motors. New types of electrical drives are created. The linear movement SR-motor may be such a new type of electrical drive. Only few scientific papers describe linear movement SR-motors, despite the fact that there is a wide scope of applications listed in chapter 1.

The thesis introduces new design methods for TF-LSR-motors. Designing should be started from the performance values set by the intended application. There are unlimited possibilities to choose the magnetical structure of the LSR-motor. In this work the very basic structure is chosen in order to get the fundamental design methods which are introduced in chapter 3.

The air gap has an effect on the traction force production, but it raises to the remarkable design parameter only when iron is used in a linear region. In this work iron is very heavily saturated to give the maximum available traction force due to which copper losses increase. The designer should also study the possibility to use a multi-tooth per stator pole structure, when iron is not heavily saturated and the air gap is chosen optimally.

The transversal flux design of the magnetic circuit for the linear movement SR-motor is more attractive than the longitudinal flux design in terms of the mover mass. This conclusion is based on the comparison described at the end of chapter 3. A one-sided two-mover poles one-stator pole transversal flux linear movement switched reluctance motor is selected for the basic construction part (basic pole pair) of all linear SR-motors.

The modelling of the static properties is done with FEM-calculations by using the BTFPP-model (basic transversal flux pole pair) introduced in chapter 5. The BTFPP-model is a two dimensional FEM-model of the one-sided two-mover poles one-stator pole transversal flux linear movement SR-motor. The BTFBB-model is accurate enough to model the static key features for the basic dimensioning of the LSR-motor. The strength of the BTFPP-model is its simplicity. It is fast to solve by means of 2D-FEM and it is quite easy to utilise. 3D-FEM-models have to be

used in order to get the most accurate calculation results of the static traction force production as a function of the mover position and current.

The most serious problem in FEM-calculations is the modelling of magnetic material. The magnetical properties of the solid materials used in the solid magnetic cores are rarely known accurately enough. The long calculation times of 3D-FEM-calculations seem to be another problem. The developed scaling law can reduce the number of the FEM-calculations needed. Now an FEM-calculation of only one size is needed, when the geometry of the poles is determined. The final 3D-FEM-model is achieved, when the size of the LSR-motor to produce the required traction force is found.

The solid iron core laboratory prototype of the basic pole pair of the TF-LSR-motors is constructed for the measurements of the static traction force production, dynamic effects and heat transfer. The measurements show that the one-sided structure is not a suitable construction even for a prototype. The normal force combined to friction causes a lot of difficulties. The protoype should be at least two-sided to have balanced normal forces.

The most important measurement is that of the static traction force as a function of the mover position and current. Despite of some errors, the measurement proved the developed static dimensioning and the modelling methods to be good enough.

The hysteresis of the iron circuit together with the friction of the bearing system makes the measurement of the static traction force quite complicated. The DC-voltage source should be current controlled in oder to keep the current steady when the temperature rise of the winding increases the resistance of the winding. Also the drift of the force transducer should be well compensated.

The static traction force gives the ideal performance of the LSR-motor. All kinds of dynamic effects reduce the ideal performance. Some transient measurements were done to find out how much the dynamic effects reduce force production. It seems also to be problematic to apply transient measurements to the laboratory prototype. The measuration coil of the induced voltage was wound on the main coil. The location of the measuration coil causes measurement errors when

all the voltages induced by the stray fluxes of the main coil are measured by the measuration coil too, when only the voltage induced by the main flux was to be measured. This problem can not be avoided by arranging the current windings.

The poles of the laboratory prototype are made of solid steel, which causes lots of eddy current effects. If the poles of the LSR-motor are made of laminated magnetic material, the eddy current effects should be less and the simulation model of figure 4.5. can be applied.

The manufactured one-sided solid iron core laboratory prototype had poorly designed magetical properties and windings. The one-sided structure was a bad selection also from a mechanical point of view. The laboratory prototype was designed at the beginning of the study. The original idea was to design a prototype as simple as possible which can be properly modelled using 3D-FEM. A comparison of the measured and calculated static traction force results shows that the project could be performed succesfully.

The methods for the basic dimensioning of the machine, for the scaling the machine size and for the modelling of the static traction force production are the main contributions of this thesis.

7 REFERENCES

(Abrahamsen, 1994) Abrahamsen, J. G., Ennemark, P., Jensen, F. A novel electromagnetic model of a linear reluctance actuator. Proceedings of the ICEM 94 Paris. 1994. 6 p.

(Adamiak, 1987) Adamiak, K., Barlow, D., Choudhury, C. P., Cusack, P. M., Dawson, G. E., Eastham, A. R., Grady, B., Ho, E., Hongping, Y., Pattison, L., Welsh, J. The switched reluctance motor as a low-speed linear drive. Proceedings of IEEE international conference on maglev & linear drives. 1987. 4 p.

(Akmese, 1989) Akmese, R., Eastham, J. F. Dynamic performance of a brushless DC tubular drive system. IEEE Transactions on Magnetics. 1989. Vol. 25, No. 5, 3 p.

(Barrass, 1996) Barrass, P. G., Mecrow, B. C. Torque control of switched reluctance drives. Proceedings of the ICEM 96 Vigo. 1996. 6 p.

(Basak, 1997) Basak, A., Flores Filho, A. F., Nakata, T., Takahashi, N. Three dimensional computation of force in a novel brushless DC linear motor. IEEE Transactions on Magnetics. 1997. Vol. 33, No. 2, 3 p.

(Bausch, 1997) Bausch, H., Kanelis, K. Feedforward torque control of a switched reluctance motor based on static measurements. ETEP. 1997. Vol. 7, No. 6, 8 p.

(Benhama, 1997) Benhama, A., Williamson, A. C., Reece, A. B. J. SRM-torque computation from 3D finite element field solutions. IEE Conference publications of the EMD97. 1997. No. 444, 4 p.

(Benhama, 1999) Benhama, A., Williamson, A. C., Reece, A. B. J. Force and torque computation from 2D and 3D finite element field solutions. IEE proceedings of the electrical power applications. 1997. Vol. 146. No. 1, 7 p.

(Ben Yahia, 1998) Ben Yahia, K., Henneberger, G. Design and control of a magnetically levitated system for a high speed machine tool with linear direct drive. Proceedings of the SPEEDAM 98 Sorrento. 1998. 6 p.

(Bertotti, 1985) Bertotti, G. Physical interpretation of eddy current losses in ferromagnetic materials. 1. Theoretical considerations. Journal of applied Physics. 1985. Vol. 57, No. 15, 16 p.

(Bertotti, 1988) Bertotti, G. General properties of power losses in soft ferromagnetic materials. IEEE Transactions on Magnetics. 1988. Vol. 24, No. 1, 9 p.

(Byrne, 1972) Byrne, J. V. Tangential forces in overlapped pole geometries incorporating ideally saturable material. IEEE Transactions on Magnetics. 1972. Vol. 8, No. 1, 8 p.

(Carpenter, 1959) Carpenter, C. Surface-integral methods of calculating forces on magnetized iron parts. IEE Monograph. 1959. No. 342, 9 p.

(Cincotti, 1997) Cincotti, S., Marchesi, M., Serri, A. Microcontroller optimal implementation of a neural network position estimator for a variable reluctance linear actuator. Proceedings of the EPE 97 Trondheim. 1997. 6 p.

(Corda, 1993) Corda, J., Masic, S., Stephenson, J., M. Computation and experimental determination of running torque waveforms in switched-reluctance motors. IEE Proceedings-B. 1993. Vol. 140, No. 6, 6 p.

(Corda, 1994) Corda, J., Wilkinson, M. Prediction and measurement of magnetic parameters of cylindrical linear switched reluctance actuator. Proceedings of the ICEM 94 Paris. 1994. 6 p.

(Corda, 1995) Corda, J., Wilkinson, M. Modelling of static thrust characteristics of cylindrical linear switched reluctance actuator. IEE Conference publications of the EMD95. 1995. No. 412, 5 p.

(Corda, 1996) Corda, J., Wilkinson, M. Effects of eddy-currents on pull-out characteristics of cylindrical linear variable-reluctance stepper motor. Proceedings of the ICEM 96 Vigo. 1996. 3 p.

(Corda, Skopljak, 1993) Corda, J., Skopljak, E. Linear switched reluctance actuator. IEE Conference publications of the EMD93. 1993. No. 376, 5 p.

(Coulomb, 1984) Coulomb, J. L., Meunier, G. Finite element implementation of virtual work principle for magnetic or electric force and torque computation. IEEE Transactions on Magnetics. 1984. Vol. 20, No. 5, 3 p.

(Deshpande, 1993) Deshpande, U. S., Cathey, J. J., Richter, E., A high force density linear switched reluctance motor. Proceedings of the 28th IEEE Industry Applications Conference. Part 1 (of 3). 1993. 7 p.

(Edwards, 1987) Edwards, J. D., Preston, M. A., Williams, G. Forces in short-secondary linear reluctance motor. IEEE Transactions on Magnetics. 1987. Vol. 23, No. 5, 3 p.

(Edwards, 1995) Edwards, J., Freeman, E. MagNet 5.1 User Guide - Using the MagNet Version 5.1 Package from Infolytica. Published by Infolytica. 1995. London and Montreal.

(Evans, 1997) Evans, S., Smith, I., Ketteleborough, J. Optimization of a short-stroke permanent magnet linear reluctance motor by finite element field modelling. IEE Conference publications of the EMD97. 1997. No. 444, 5 p.

(Fiorillo, 1990) Fiorillo, F., Novikov, A. An improved approach to power losses in magnetic laminations under nonsinusoidal induction waveform. IEEE Transactions on Magnetics. 1988. Vol. 26, No. 5, 6 p.

(Gieras, 1997) Gieras, J. F., Wang, R. Calculation of forces in a hybrid linear stepping motor for machine tools. Proceedings of the EPE'97 Trondheim. 1997. 5 p.

(Qu, 1997) Qu, Q. S., Stiebler, M. Scaling and dimensioning of switched reluctance machines. ETEP. 1997. Vol. 7, No. 5. 10 p.

(Harris, 1991) Harris, M., Miller, T. Comparison of design and performance parameters in switched reluctance and induction motors. Proceedings of ICEM 1991. 1991. 5 p.

(Hayashiya, 1997) Hayashiya, H., Katayama, T., Ohsaki H., Masada E. Feasibility of non-contacting conveyance system for a steel plate using normal and thrust force of a linear induction motor. Proceedings of the EPE'97. 1997. 6 p.

(Hendershot, 1994) Hendershot, J. R. Design of brushless permanent magnet motors. Hillsboro, USA. Magna Physics Publishing. 1994. 0-19-859389-9. 580 p.

(Imal, 1994) Imal, E., Williams, G. Suspension and propulsion forces on can secondaries of linear reluctance motors. Proceedings of the Mediterranean Electrotechnical Conference (IEEE) - MELECON. Part 2 (of 3). 1994. 4 p.

(Khan, 1994) Khan, S. H., Ivanov, A. A. Modelling and computation of nonlinear magnetic fields in linear step motors by finite element method. IEEE Transactions on Magnetics. 1994. Vol. 30, No. 6, 3 p.

(Kuisma, 1997) Kuisma, M. Häiriösuojaus elektroniikan laitesuunnittelussa. Lappeenranta. Diplomityö. Lappeenrannan teknillinen korkeakoulu, 1997. 91p. (In finnish).

(Lawrenson, 1980) Lawrenson, P., Stephenson, J., Blenkinsop, P., Corda, J., Fulton, N. Variable speed switched reluctance motors. IEE Proceedings-B. 1980. Vol. 127, No. 4, 15 p.

(Leu, 1988) Leu, M. C., Scorza, E. V., Bartel, D. L. Characteristics and optimal desing of variable airgap linear force motor. IEE Proceedings-B. 1988. Vol. 135, No. 6, 5 p.

(Li, 1994) Li, J., Jufer, M. Modelling and dynamical simulations of switched reluctance motors including iron losses. Proceedings of the ICEM 94 Paris. 1994. 5 p.

(Liu, 1994) Liu, C., Kuo, J. Experimental investigation and 3-D modelling of linear variable reluctance machine with magnetic-flux decoupled windings. IEEE Transactions on Magnetics. 1994. Vol. 30, No. 6, 3 p.

(Lovatt, 1997) Lovatt, H., McClelland, M., Stephenson, J. Comparative performance of singly salient reluctance, switched reluctance and induction motors. IEE Conference publications of the EMD97. 1997. No. 444, 5 p.

(McFee, 1987) McFee, S., Lowther, D. A. Towards accurate and consistent force calculations in finite element based computational magnetostatics. IEEE Transactions on Magnetics. 1987. Vol. 23, No. 5, 3 p.

(McLean, 1988) McLean, G. W. Review of recent progress in linear motors. IEE Proceedings-B. 1988. Vol. 135, No. 6, 36 p.

(Michaelides, 1994) Michaelides, A. M., Pollock, C. Effect of end core flux on the performance of the switched reluctance motor. IEE Proceedings-B. 1994. Vol. 141, No. 6, 8 p.

(Miller, 1993) Miller, T. Switched Reluctance Motors and their Control. Chelsea, USA. Magna Physics Publishing. 1993. ISBN 0-19-859387-2. 200 p.

(Moghani, 1994) Mogani, J. S., Eastham, J. F., Akmese, R., Hill-Cottingham, R. J. Three dimensional force prediction in a model linear brushless DC motor. IEEE Transactions on Magnetics. 1994. Vol. 30, No. 6, 3 p.

(O'Connor, 1980) O'Connor, W. J. Magnetic forces in idealised saturable-pole configurations. IEE Proceedings-B. 1980. Vol. 127, No. 1, 5 p.

(Osada, 1998) Osada, T., Watada, M., Ebihara, D. The design of linear oscillatory actuator for artificial heart with the blood pump. Proceedings of the SPEEDAM 98 Sorrento. 1998. 6 p.

(Pulle, 1991) Pulle, D.,W., J. New data base for switched reluctance drive simulation. IEE Proceedings-B. 1991. Vol. 138, No. 6, 7 p.

(Pyrhönen, 1991) Pyrhönen, J. The high-speed induction motor: Calculating the effects of solid-rotor material on machine characteristics. Acta polytechnica scandinavia. The Finnish Academy of Technology. Helsinki. 1991. El 68. 84 p.

(Redlich, 1996) Redlich, R., Unger, R., Van der Walt, N. Linear compressors: motor configuration, mudulation and systems. Proceedings of the 1996 International Compressor Engineering Conference West Lafayette USA. 1996. http://www.sunpower.com/pub68/purdue.html, 7 p.

(Rizzo, 1995) Rizzo, M., Savini, A. The optimal scaling of a linear reluctance motor by field computation. The international journal for computation and mathematics in electrical and electronic engineering. 1995. Vol. 14, No. 4, 5 p.

(Rizzo, 1997) Rizzo, M., Savini, A., Turowski, J. Comparative field analysis of linear variable-reluctance small motors. Electromotion. 1997. Vol. 4, July-Septemper, 4 p.

(Roubicek, 1988) Roubicek, O., Pejsek, Z., Podzimek, O. Progress in the development of electric linear drives intended for technological applications. Electric Machines and Power Systems. 1988. Vol. 14, 8 p.

(Salo, 1996a) Salo, J., Silventoinen, P., Tolsa, K., Pyrhönen, J. Calculations and measurements of the magnetic properties of a 6/4-SR-motor. Proceedings of the SPEEDAM 96 Capri, 1996. 6 p.

(Salo, 1996b) Salo, J. Molemmin puolin avonapainen reluktanssimoottori. Lappeenranta. Lisensiaatintutkimus. Lappeenranan teknillinen korkeakoulu energiatekniikan osasto sähkötekniikan laitos. 1996. 75 p. (In finnish).

(Silventoinen, 1999) Silventoinen, P., Salo, J., Tolsa, K., Pyrhönen, J. Dynamic tests with a switched reluctance motor drive. IEEE Aerospace and Electronic Systems Magazine. 1999. Vol. 14, No. 1, 4 p.

(Silvester, 1983) Silvester, P. P., Ferrari, R. L. Finite elements for electrical engineers. Cambridge University Press, Cambridge. 1983. 209 p.

(Sjöberg, 1996) Sjöberg, L., Alaküla, M. Table based torque control of a new switched reluctance machine drive system. Proceeding of the nordic research symposium, energy efficient electric motors and drives, 1996. 6 p.

(Stephenson, 1979) Stephenson, J. M., Corda, J. Computation of torque and current in doubly-salient reluctance motors from nonlinear magnetization data. IEE Proceedings. 1979. Vol. 126, No. 5, 6 p.

(Stephenson, 1989) Stephenson, J. M., El-Khazendar, M. A. Saturation in doubly salient reluctance motors. IEE Proceedings-B. 1989. Vol. 136, No. 1, 9 p.

(Tolsa, 1996) Tolsa, K., Silventoinen, P., Salo, J., Pyrhönen, J. Torque control of the switched reluctance motor minimizing copper losses. Proceedings of the ICEM 96 Vigo. 1996. 6 p.

(Vogt, 1996) Vogt, K. Berechnung elektrischer maschinen. Weinheim, Germany. VCH. 1996. ISBN 3-527-28391-9. 524 p.

(Wakiwaka, 1996) Wakiwaka, H.,Yajima, H., Senoh, S., Yamada, H. Simplified thrust limit equation of linear DC motor. IEEE Transactions on Magnetics. 1996. Vol. 32, No. 5, 3 p.

(York, 1997) York, M., Stephenson, J. M., Hughes, A. A novel electronically-operated linear variable-reluctance actuator. Proceedings of the EPE'97. 1997. 6 p.